Communications Research Centre

THE DISTORTION OF AM BROADCAST ANTENNA PATTERNS AS CAUSED BY NEARBY TOWERS AND HIGHRISE BUILDINGS

by

G.M. Royer

Government of Canada
Department of Communications

Gouvernement du Canada
Ministère des Communications

CRC REPORT NO. 1379

OTTAWA, MARCH 1985

Canada

COMMUNICATIONS RESEARCH CENTRE

DEPARTMENT OF COMMUNICATIONS
CANADA

THE DISTORTION OF AM BROADCAST ANTENNA PATTERNS AS CAUSED BY NEARBY TOWERS AND HIGHRISE BUILDINGS

by

G.M. Royer

(Radar and Communications Technology Branch)

CRC REPORT NO. 1379

March 1985

OTTAWA

TABLE OF CONTENTS

THE DISTORTION OF AM BROADCAST ANTENNA PATTERNS AS CAUSED BY NEARBY TOWERS AND HIGHRISE BUILDINGS

by

G.M. ROYER

ABSTRACT

AM broadcast antennas are designed to have patterns which provide an adequate broadcasting service, while at the same time satisfying domestic and international regulations with respect to permissible levels of interference with signals from other stations operating in the same frequency band. The erection of a tower or highrise building near a broadcast antenna could possibly distort the antenna's pattern such that the above objectives are not met. It is the purpose of this report to: 1) provide the engineer with sufficient information to enable him to compute whether or not a given structure will cause serious pattern distortion, and 2) investigate methods for reducing the strength of a tower's scattered field; thereby reducing the tower's pattern distorting effects.

1. INTRODUCTION

Functions are derived in Section 2 which give upper and lower bounds for the directive gain pattern of an AM broadcast antenna in the presence of a scatterer. Note that functions which give bounds for the directive gain (as distinguished from a function which gives the antenna's actual gain) are provided because the former: 1) are less complex, 2) require a simpler characterization of the scatterer's properties (because, as will be shown, we need not concern ourselves with relative phases of the scattered and antenna signals), and 3) should provide sufficient information to enable the engineer to decide whether or not a scatterer will significantly distort an antenna's directive gain pattern. In the above functions the scattering structure's scattering properties are contained in a parameter called scattering cross-section. Scattering cross-section values are not readily available and therefore figures showing this parameter are provided in Section 3. Use of the information contained in Section 3 should make it possible to estimate the scattering cross-section for most towers and buildings which are likely to cause a pattern distortion problem. Section 4 investigates methods for reducing a tower's scattering cross-section (hence reducing the towers effect on the antennas directive gain pattern). Section 2's functions for computing the upper and lower bounds for the directive gain of an array-scatterer combination, become inaccurate if the array-to-scatterer range is too small. This problem is investigated in Section 5 through the application of the above functions to specific situations.

Unless otherwise indicated, all calculations were done using a computer program called Numerical Electromagnetic Code (NEC). NEC employs the Method of Moments[1] and was written by G.J. Burke[2] and A.J. Poggio at the Lawrence Livermore National Laboratory. Appendix B contains an experimental test of the ability of NEC to solve the types of problems on which it was employed in the research reported here.

This document forms the final report for the author's contribution to a project (see references 4 to 11), whose purpose was to determine the magnitude of, and find remedial measures for, the pattern distorting effects of towers, buildings (the structures considered here) and power transmission lines near AM broadcast antennas.

2. UPPER AND LOWER BOUNDS ON THE DIRECTIVE GAIN FOR AN AM BROADCAST ANTENNA IN THE PRESENCE OF A SCATTERER

In this section, two pairs of functions (called near-field limit functions and far-field limit functions) are derived. Either pair can be used to compute upper and lower bounds on the directive gain for an AM broadcast array in the presence of a scatterer. The near-field limit functions are more complex than the far-field limit functions, they are however accurate down to smaller array-to-scatterer ranges.

The near-field functions are derived first. Figure 1 shows the geometry which will be used. Throughout this document, the ground plane and all structures are considered to be perfectly conducting. The array elements are numbered 1,2,...n where k is used to represent a general array element number. Let (r,θ,ϕ) locate a far-field point and

$S_{a\theta}(r,\theta,\phi)$ = the power density (e.g. watts/m^2) at (r,θ,ϕ) of the θ polarized component for the signal from the antennas when there is no scatterer present

$S_{\theta}(r,\theta,\phi)$ = the power density at (r,θ,ϕ) of the θ polarized component for the signal from the antenna-scatterer combination.

$S_{s\theta}(r,\theta,\phi)$ = the power density at (r,θ,ϕ) of the θ polarized component for the signal scattered by the scatterer.

At (r,θ,ϕ) the θ polarized electric field intensity of the signal from the array-scatterer combination ($E_{\theta}(r,\theta,\phi)$) is equal to the sum of the θ polarized electric field intensity when there is no scatterer present ($E_{a\theta}(r,\theta,\phi)$) and the θ polarized scattered field ($E_{s\theta}(r,\theta.\phi)$), i.e.

$$E_{\theta}(r,\theta,\phi)=E_{a\theta}(r,\theta,\phi)+E_{s\theta}(r,\theta,\phi) \qquad ...(1)$$

The above is true by definition of the scattered field. Note that in this document complex quantities (where $\exp(j\omega t)$ is understood) are used to represent electric field intensities, voltages and currents. For example the time varying, θ polarized, total electric field intensity at (r,θ,ϕ) is given by the real part of $E_{\theta}(r,\theta,\phi)\exp(j\omega t)$. Equation (1) shows that, for the purpose of computing the magnitude of E_{θ} (i.e. $|E_{\theta}|$) we need to know both the magnitude and relative phase for $E_{a\theta}$ and $E_{s\theta}$. In the derivation which follows the scattering properties of the scatterer will be charactized by its scattering cross-section. This parameter will enable us to compute $S_{s\theta}$ or $|E_{s\theta}|$ (using $S_{s\theta}=|E_{s\theta}|^2/\eta$ where $\eta=376.73\Omega$, the wave impedance for free space (air)). In other words the scatterer's scattering cross-section lacks sufficient information to enable us to compute the relative phase between $E_{a\theta}$ and $E_{s\theta}$ (see eqn. 1). However, as is shown in (2) below, it is possible to compute upper and lower bounds on S_{θ} where the above bounds correspond to the cases where $E_{a\theta}$ and

$E_{s\theta}$ are respectively in phase and 180° out of phase.

$$[S_{a\theta}(r,\theta,\phi)^{\frac{1}{2}} - S_{s\theta}(r,\theta,\phi)^{\frac{1}{2}}]^2 \leq S_{\theta}(r,\theta,\phi) \leq [S_{a\theta}(r,\theta,\phi)^{\frac{1}{2}} + S_{s\theta}(r,\theta,\phi)^{\frac{1}{2}}]^2 \quad ...(2)$$

By definition of directive gain, $S_{a\theta}$ and S_{θ} are given by

$$S_{a\theta}(r,\Theta,\phi) = \frac{P_t}{4\pi r^2} D_{a\theta}(\Theta,\phi) \quad ...(3)$$

$$S_{\theta}(r,\theta,\phi) = \frac{P_t}{4\pi r^2} D_{\theta}(\theta,\phi) \quad ...(4)$$

P_t= the power transmitted by the array.

$D_{a\theta}(\theta,\phi)$ = the θ polarized directive gain, in the direction (θ,ϕ), for the array when there is no scatterer present.

$D_{\theta}(\theta,\phi)$ = the θ polarized directive gain, in the direction (θ,ϕ), for the array-scatterer combination.

Consider next the case shown in Fig. 2 where only array element k is present (i.e. the scatterer and other array elements are absent). By definition of directive gain the θ polarized power density of the signal radiated is given by

$$S_{\theta k}(r_k,\theta_k) = \frac{P_{tk} D_{\theta k}(\theta_k)}{4\pi r_k^2} \quad ...(5)$$

where (r_k,θ_k,ϕ_k) locates a far-field point in array element k's coordinate system and

P_{tk} = the power transmitted by array element k

$D_{\theta k}(\theta_k)$ = the θ_k polarized directive gain for array element k when the scatterer and other array elements are absent.

Note that broadcast array elements are usually monopoles which radiate omni-directionally as a function of ϕ (neglecting the effect of the guy wires, which should be small if they are broken by a sufficient number of insulators). Therefore no ϕ_k dependence has been shown above for $S_{\theta k}$ and $D_{\theta k}$. The ground plane and array element are perfectly conducting (hence the system is lossless) and therefore

$$P_{tk} = |I_k|^2 R_k/2 \quad ...(6)$$

$$I_k = |I_k| \exp(j\alpha_k) \quad ...(7)$$

I_k = the complex peak current at the input of array element k

R_k = the radiation resistance of array element k when the scatterer and other array elements are absent.

Equation (5) can now be written as follows

$$S_{\theta k}(r_k,\theta_k) = \frac{|I_k|^2 R_k D_{\theta k}(\theta_k)}{2(4\pi r_k^2)} \qquad ...(8)$$

For the case shown in Fig. 1 where the scatterer and all array elements are present and excited, we will (in accordance with eqn.(8)) let the power density of the signal which is from array element k and incident on the scatterer be given by

$$S_{\theta k}(r_{sK},90°) = \frac{|I_k|^2 R_k D_{\theta k}(90°)}{2(4\pi r_{sk}^2)} \qquad ...(9)$$

r_{sk} = the range between array element k and the scatterer.

Equation (9) gives $S_{\theta k}(r_{sk},90°)$ accurately if r_{sk} is sufficiently large (i.e. large enough such that the scatterer is in array element k's far-field) and the current distribution on array element k is not significantly changed by the presence of the scatterer and other array elements. The above constant current distribution assumption would result in significant error if the length of the array elements were too large. AM broadcast band monopoles are only about one quarter wavelength (or less) long. This length is small enough such the error, introduced by the above constant current distribution assumption, will be small. Note that two spatially distributed currents are considered here to have the same current distribution if a constant can be found such that the constant times one of the current distributions can be made equal to the other current distribution. The following equation is true by definition of scattering cross-section.

$$S_{s\theta k}(r,\theta,\phi) = \frac{S_{\theta k}(r_{sk},90°)\sigma_\theta(\theta,\phi)}{4\pi r^2} \qquad ...(10)$$

$S_{s\theta k}(r,\theta,\phi)$ = the power density at (r,θ,ϕ) of the θ polarized component for the signal scattered by the scatterer when the incident signal is from array element k.

$\sigma_\theta(\theta,\phi)$ = the θ polarized scattering cross-section for the scatterer in the direction (θ,ϕ).

Scattering cross-section has the dimensions of area (e.g. m^2) where, for example, $\sigma_\theta(\theta,\phi)$ can be thought of as the area which when multiplied by the power density for an incident plane wave ($S_{\theta k}(r_{sk},90°)$ in eqn. (10)) would give a signal power (e.g. watts) which, if scattered omni-directionally, would result in a θ polarized scattered signal with a power density ($S_{s\theta k}(r,\theta,\phi)$ in eqn. (10)) equal to that which actually exists at (r,θ,ϕ). In the above definition for scattering cross-section we specified the polarization (θ) and direction

(θ,ϕ) for the scattered far-electric-field intensity. A complete definition for scattering cross-section would include the polarization and direction of incidence for the field incident on the scatterer. The incident field can be considered to be composed of components; one for each element of the array. It is assumed that: 1) over the dimensions of the scatterer, the incident fields are vertically polarized plane waves, and 2) in a given far-field direction, the scatterer's scattering cross-section is nearly constant over the range of angles of incidence for the component incident signals. The last assumption will result in negligible error when the scatterer is a tower because at AM broadcast frequencies a tower's horizontal dimensions, in wavelengths, are very small. This assumption will not be as good when the scatter is a building. However, note that the range of angles of incidence should be small, and at 1MHz the horizontal dimensions in wavelengths for a 60mx60m building are only about $.2\lambda x.2\lambda$.

When eqns (9) and (10) are combined we get

$$S_{s\theta k}(r,\theta,\phi) = \frac{|I_k|^2 R_k D_{\theta k}(90°)\sigma_\theta(\theta,\phi)}{2(4\pi r_{sk} r)^2} \qquad ...(11)$$

The total θ polarized scattered field intensity is obtained by adding together its components, where eqn. (11) gives the power density for the component of the scattered field due to array element k. When this is done it is found that the power density for the total θ polarized scattered field is given by

$$S_{s\theta}(r,\theta,\phi) = \left| \sum_{k=1}^{n} \left\{ \left[\frac{|I_k|^2 R_k D_{\theta k}(90°)\sigma_\theta(\theta,\phi)}{2(4\pi r_{sk} r)^2} \right]^{\frac{1}{2}} \right.\right.$$

$$\left.\left. x\exp\left[j\left(\alpha_k - \frac{2\pi}{\lambda} r_{sk} \right) \right] \right\} \right|^2 \qquad ...(12)$$

λ = the wavelength of the transmitted signal.

We get the following upper and lower bounds (near-field limit functions) on the directive gain for an AM broadcast array in the presence of a scatterer when (2) and eqns. (3), (4) and (12) are combined.

$$[D_{a\theta}(\theta,\phi)^{\frac{1}{2}} - N_\theta(\theta,\phi)]^2 \leqq D_\theta(\theta,\phi) \leqq [D_{a\theta}(\theta,\phi)^{\frac{1}{2}} + N_\theta(\theta,\phi)]^2 \qquad ...(13)$$

$$N_\theta(\theta,\phi) = \left[\frac{\sigma_\theta(\theta,\phi)}{8\pi P_t} \right]^{\frac{1}{2}} \left| \sum_{k=1}^{n} \left\{ \frac{|I_k|[R_k D_{\theta k}(90°)]^{\frac{1}{2}}}{r_{sk}} \right.\right.$$

$$\left.\left. x\exp\left[j\left(\alpha_k - \frac{2\pi}{\lambda} r_{sk} \right) \right] \right\} \right|$$

If all of the array elements are identical then $N_\theta(\theta,\phi)$ can be expressed as follows.

$$N_\theta(\theta,\phi) = \left[\frac{R_k D_{\theta k}(90°)\sigma_\theta(\theta,\phi)}{8\pi P_t}\right]^{\frac{1}{2}}$$

$$x\left|\sum_{k=1}^{n}\left\{\frac{|I_k|}{r_{sk}}\exp\left[j\left(\alpha_k - \frac{2\pi}{\lambda}r_{sk}\right)\right]\right\}\right|$$

Note that $|I_k|$ in the $N_\theta(\theta,\phi)$ functions is a peak (as distinguished from an rms) current.

When the array-to-scatterer range is large enough such that the scatterer is in the array's far-field then (as shown below and refer to Fig. 3) the directive gain for the array can be used to accurately compute the power density for the signal incident on the scatterer.

$$S_{a\theta}(r_s,90°,180°) = \frac{P_t D_{a\theta}(90°,180°)}{4\pi r_s^2} \qquad ...(14)$$

r_s = the range between the array and scatterer.

Note that the geometry shown in Fig. 3 is such that the direction of the scatterer with respect to the array is $(\theta,\phi)=(90°,180°)$ and therefore $D_{a\theta}(90°,180°)$ is $D_{a\theta}(\theta,\phi)$ in the direction of the scatterer. By definition of scattering cross-section, it follows from eqn. (14) that the power density for the θ polarized scattered field is given by

$$S_{s\theta}(r,\theta,\phi) = \frac{P_t D_{a\theta}(90°,180°)\sigma_\theta(\theta,\phi)}{(4\pi r_s r)^2} \qquad ...(15)$$

When (2) and eqn (3), (4) and (15) are combined the following upper and lower bounds on $D_\theta(\theta,\phi)$ (called far-field limit functions) are obtained

$$[D_{a\theta}(\theta,\phi)^{\frac{1}{2}} - F_\theta(\theta,\phi)]^2 \leqq D_\theta(\theta,\phi) \leqq [D_{a\theta}(\theta,\phi)^{\frac{1}{2}} + F_\theta(\theta,\phi)]^2 \qquad ...(16)$$

$$F_\theta(\theta,\phi) = \left[\frac{D_{a\theta}(90°,180°)\sigma_\theta(\theta,\phi)}{4\pi r_s^2}\right]^{\frac{1}{2}}$$

Far-field limit functions for the ϕ polarized directive gain of an AM broadcast array in the presence of a scatterer can similarly be derived. The result is

$$[D_{a\phi}(\theta,\phi)^{\frac{1}{2}} - F_{\phi}(\theta,\phi)]^2 \leqq D_{\phi}(\theta,\phi) \leqq [D_{a\phi}(\theta,\phi)^{\frac{1}{2}} + F_{\phi}(\theta,\phi)]^2 \qquad \ldots(17)$$

$$F_{\phi}(\theta,\phi) = \left[\frac{D_{a\theta}(90°,180°)\sigma_{\phi}(\theta,\phi)}{4\pi r_s^2} \right]^{\frac{1}{2}}$$

$D_{a\phi}(\theta,\phi)$ = the ϕ polarized directive gain, in the direction (θ,ϕ), for the array when there is no scatterer present

$D_{\phi}(\theta,\phi)$ = the ϕ polarized directive gain, in the direction (θ,ϕ), for the array-scatterer combination

$\sigma_{\phi}(\theta,\phi)$ = the ϕ polarized scattering cross-section for the scatterer, in the direction (θ,ϕ).

When deriving the near-field and far-field limit functions a simplifying assumption was made which was not mentioned. In particular, second and higher order scattering were ignored. For example, we ignored the signal which was scattered from the scatterer, to the array, and then rescattered by the array. The error introduced by the above assumption will be small if: 1) the interaction between the scatterer and array does not significantly change the current distributions on the array elements (see discussions following eqn. (9)), and 2) the excitations for the array elements when the scatterer is present are changed to make the feed currents the same as they were when the scatterer was absent.

When the near-field (see (13)) and far-field (see (16) and (17) limit functions are compared it is seen that the former are more complex. However the minimum usable array-to-scatterer range when the near-field functions are used is less than that for the far-field functions. In particular r_s should be such that the scatterer is in the far-field of, 1) each individual array element, or 2) the whole array, when respectively the near-field and far-field limit functions are employed.

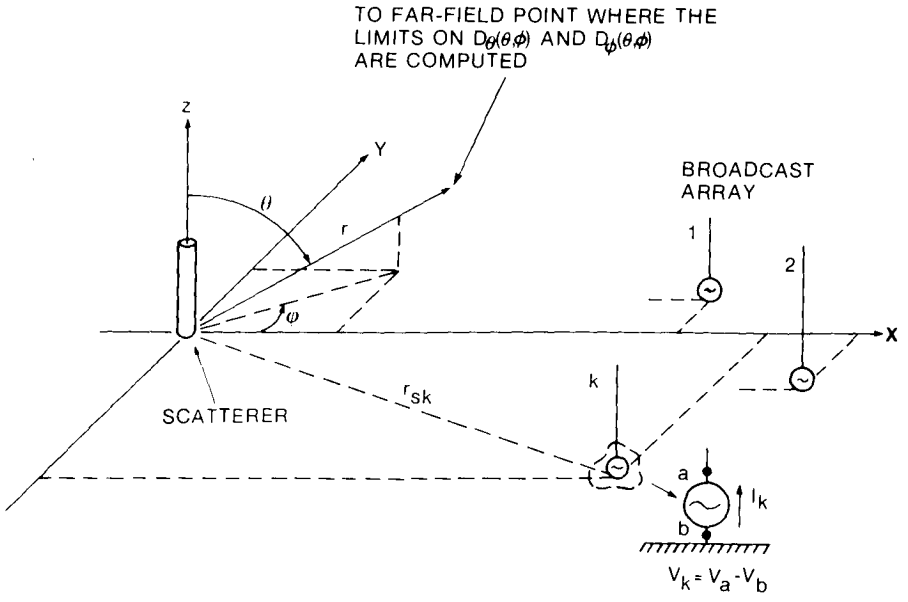

Fig. 1, Geometry used when deriving the near-field limit function on the directive gain for an AM braodcast array in the presence of a scatterer.

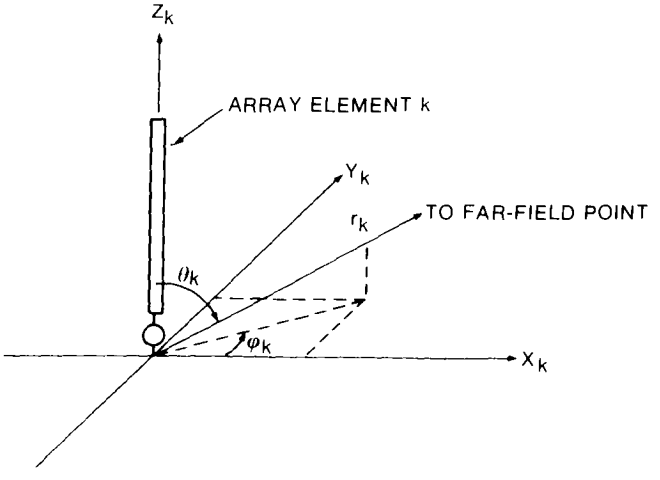

Fig. 2, Geometry used when considering array element k in the absence of the scatterer and other array elements.

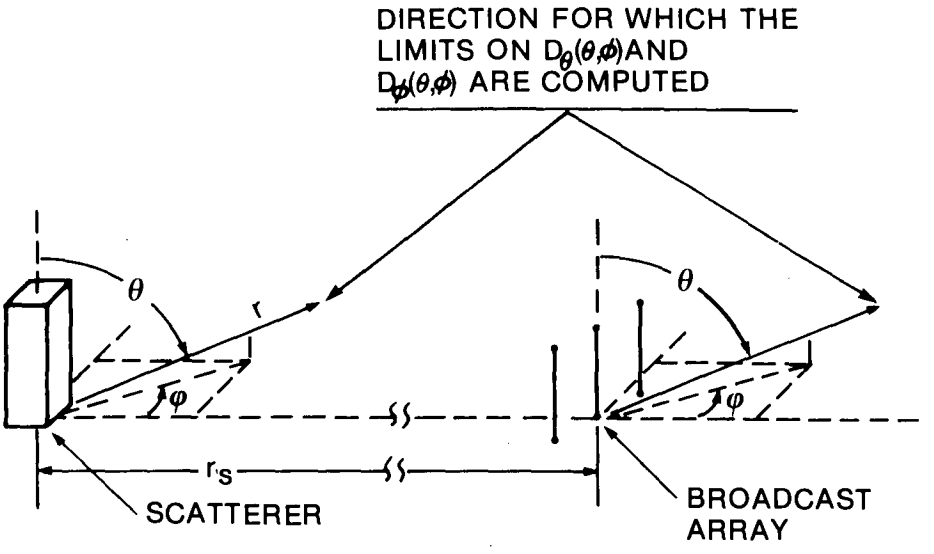

Fig. 3, Geometry used when deriving the far-field limit functions on the directive gain for an AM broadcast array in the presence of a scatterer.

3. THE SCATTERING CROSS-SECTION FOR TOWERS AND BUILDINGS

Before section 2's limit functions can be used, the scattering structure's scattering cross-section characteristics must be known. This section contains figures showing scattering cross-section for a sufficiently wide range of structures such that this parameter can at least be estimated for most towers and buildings which are likely to cause a pattern distortion problem. In particular we consider scattering cross-section characteristics for structures ranging from towers with radii equal to $.0005\lambda$ up to buildings whose dimensions in horizontal cross-section are $.2\lambda x.2\lambda$. In the figures, structure dimensions and scattering cross-section values are normalized and made to be dimensionless by dividing the dimensins by λ and the scattering cross-section values by λ^2. This makes the information in the figures easily usable at any frequency.

The computer program NEC was used to compute all scattering cross-section values. Towers whose normalized radii (a/λ) were less than or equal to .008 were modelled using a single (circular in cross-section) wire. A wire grid was employed to model structures whose dimensions in cross-section were larger than that above. The ground plane and wires were considered to be perfectly conducting.

Figures 4 and 5 plot the normalized θ polarized scattering cross-section along the ground plane ($\sigma_\theta(90°,\phi)/\lambda^2$), as a function of normalized tower height (h/λ). Each curve in the above figures is for a particular value of a/λ and a/λ ranges between .0005 and .008. Figures 6 through 9 contain vertical $\sigma_\theta(\theta,\phi)/\lambda^2$ patterns for the case where a/λ is .004 and each pattern is for the value h/λ indicated. Sufficient vertical patterns are shown such that (when $a/\lambda=.004$) an accurate estimate can be made of $\sigma_\theta(\theta,\phi)/\lambda^2$ for any tower where $.1 \leqq h/\lambda \leqq 1$. Note, it has been found that towers where a/λ is less than about .008, scatter almost omni-directionally as a function of ϕ and therefore the values of $\sigma_\theta(\theta,\phi)/\lambda^2$ given in Figs. 4 through 9 are applicable for any value of ϕ. The vertical patterns in Figs. 6 to 9 (for which $a/\lambda = .004$) and the information contained in Figs. 4 and 5, can be used to estimate $\sigma_\theta(\theta,\phi)/\lambda^2$ values for $.0005 \leqq a/\lambda \leqq .008$ provided h/λ is less than about .5. This is so because it has been found that when a/λ and h/λ satisfy the above conditions, the shape of a tower's vertical $\sigma_\theta(\theta,\phi)/\lambda^2$ pattern, on log-linear graph paper, is nearly independent of a/λ. For example let us compute $\sigma_\theta(\theta,\phi)/\lambda^2$ for the case where $h/\lambda=.5$, $a/\lambda=.0005$ and $\theta=40°$. When $h/\lambda=.5$ and $a/\lambda=.004$, Fig. 7 gives $\sigma_\theta(\theta,\phi)/\lambda^2$ as $1.77\text{x}10^{-1}$ and $3.42\text{x}10^{-2}$ when θ is respectively 90° and 40°. Figure 4 shows $\sigma_\theta(90°,\phi)/\lambda^2$ to be $8.20\text{x}10^{-2}$ for the case where $h/\lambda=.5$ and $a/\lambda=.0005$. It follows that $\sigma_\theta(40°,\phi)/\lambda^2$, when $h/\lambda=.5$ and $a/\lambda=.0005$, is given by

$$\sigma_\theta(40°,\phi)/\lambda^2 = 8.20\text{x}10^{-2}\ \frac{3.42\text{x}10^{-2}}{1.77\text{x}10^{-1}} = 1.53\text{x}10^{-2}$$

A direct calculation, using NEC, gives $1.56\text{x}10^{-2}$ for the above.

Figures 10 to 33 present scattering cross-section characteristics for structures with horizontal dimensions which are larger than those considered above. The structures were modelled using a wire grid (as distinguished from a single wire). This was done because NEC places computed wire currents along the center of the wire and hence single wire vertical towers are computed to have ϕ omni-directional $\sigma_\theta(\theta,\phi)/\lambda^2$ patterns. It has been found however that vertical towers where a/λ is greater than about .008, have $\sigma_\theta(\theta,\phi)/\lambda^2$ patterns which depart significantly from being ϕ omni-directional. Those figures, in Figures 10 to 33, which plot $\sigma_\theta(90°,\phi)/\lambda^2$ as a function of h/λ show two curves for a structure with a given size in horizontal cross-section. They correspond to the maximum and minimum values for $\sigma_\theta(90°,\phi)/\lambda^2$ as a function of ϕ. We concentrate on presenting θ polarized scattering cross-section characteristics along the ground plane ($\sigma_\theta(90°,\phi)/\lambda^2$). The exceptions to this occurs for .1x.1λ buildings where, in additon to $\sigma_\theta(90°,\phi)/\lambda^2$ characteristics, we consider horizontal patterns (where $\theta < 90°$), and vertical patterns for both σ_θ/λ^2 and σ_ϕ/λ^2.

Figures 10 and 11 plot $\sigma_\theta(90°,\phi)/\lambda^2$ versus h/λ for wire grid structures whose dimensions in horizontal cross-section are .016λx.016λ, .032λx.032λ and .064λx.064λ. Note that, as a function of ϕ, $\sigma_\theta(90°,\phi)/\lambda^2$: 1) is nearly ϕ omni-directional for the .016λx.016λ wire grid structures, and 2) departs significantly from being ϕ omni-directional for the .032λx.032λ, and larger, wire grid structures. The single wire towers considered in Figs. 4 and 5,where "a" is .008λ, are about the same size in horizontal cross-section as the .016λx.016λ wire grid structures. The above therefore supports the previously made statement that, when using NEC, a/λ, for single wire towers, should not be larger than about .008.

Figures 12 to 33 show scattering cross-section characteristics for wire grid buildings whose horizontal dimensions are .1λx.1λ, .2λx.2λ and .1λx.2λ. It is shown that rotation (where the direction of propagation for the incident signal remains unchanged) of the above square in horizontal cross-section buildings (i.e. the .1λx.1λ and .2λx.2λ buildings) has little effect on the structures' scattering properties. This statement is no doubt true for all simple (i.e. no stubs) structures whose horizontal dimensions are square and less than .2λx.2λ. Inspection of Figs. 25 to 33 shows that the above statement is not true for the building whose horizontal dimensions are .1λx.2λ.

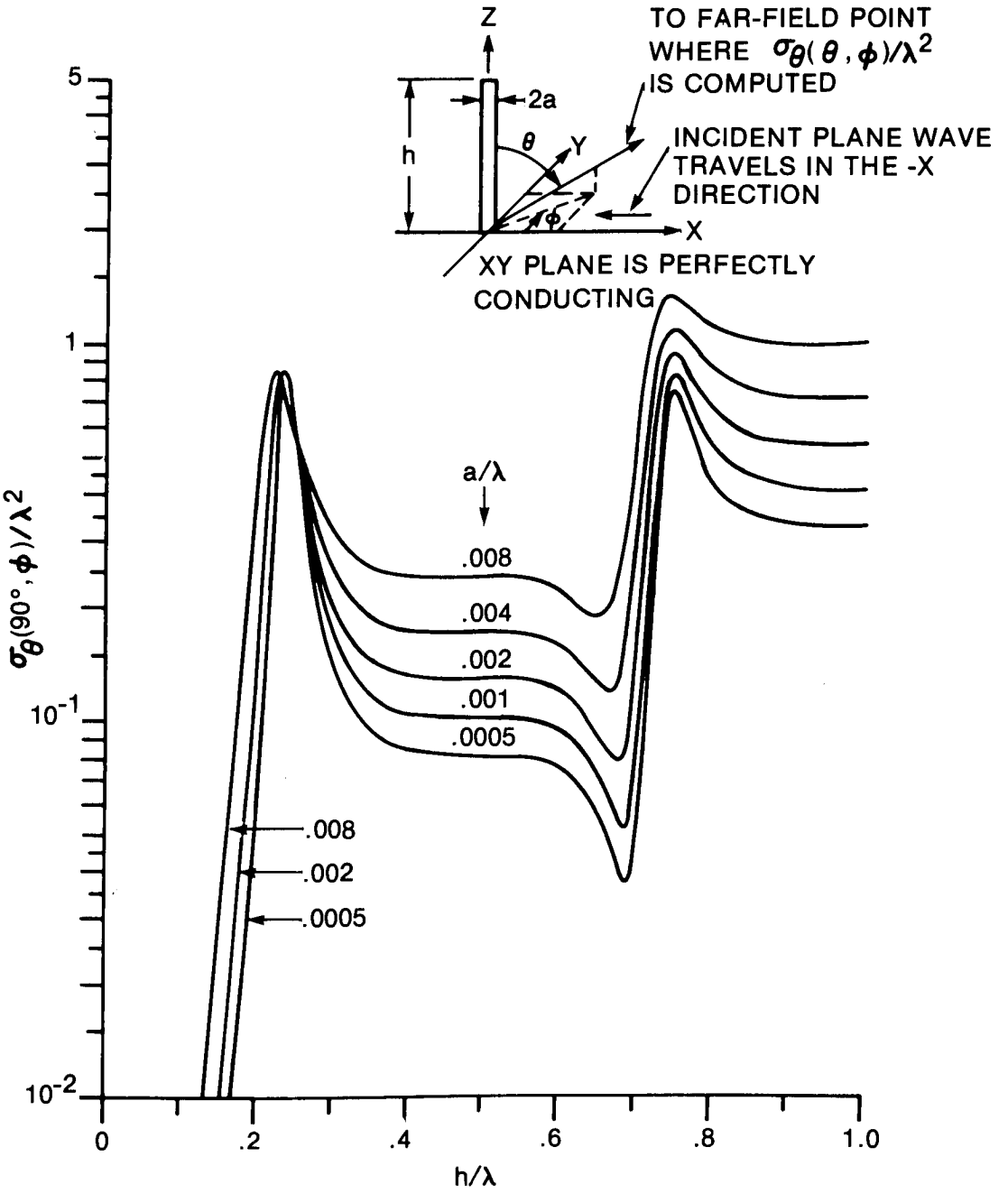

Fig. 4, $\sigma_\theta(90°,\phi)/\lambda^2$ as a function of h/λ, for single-wire towers with normalized radii (a/λ) ranging between .0005 and .008.

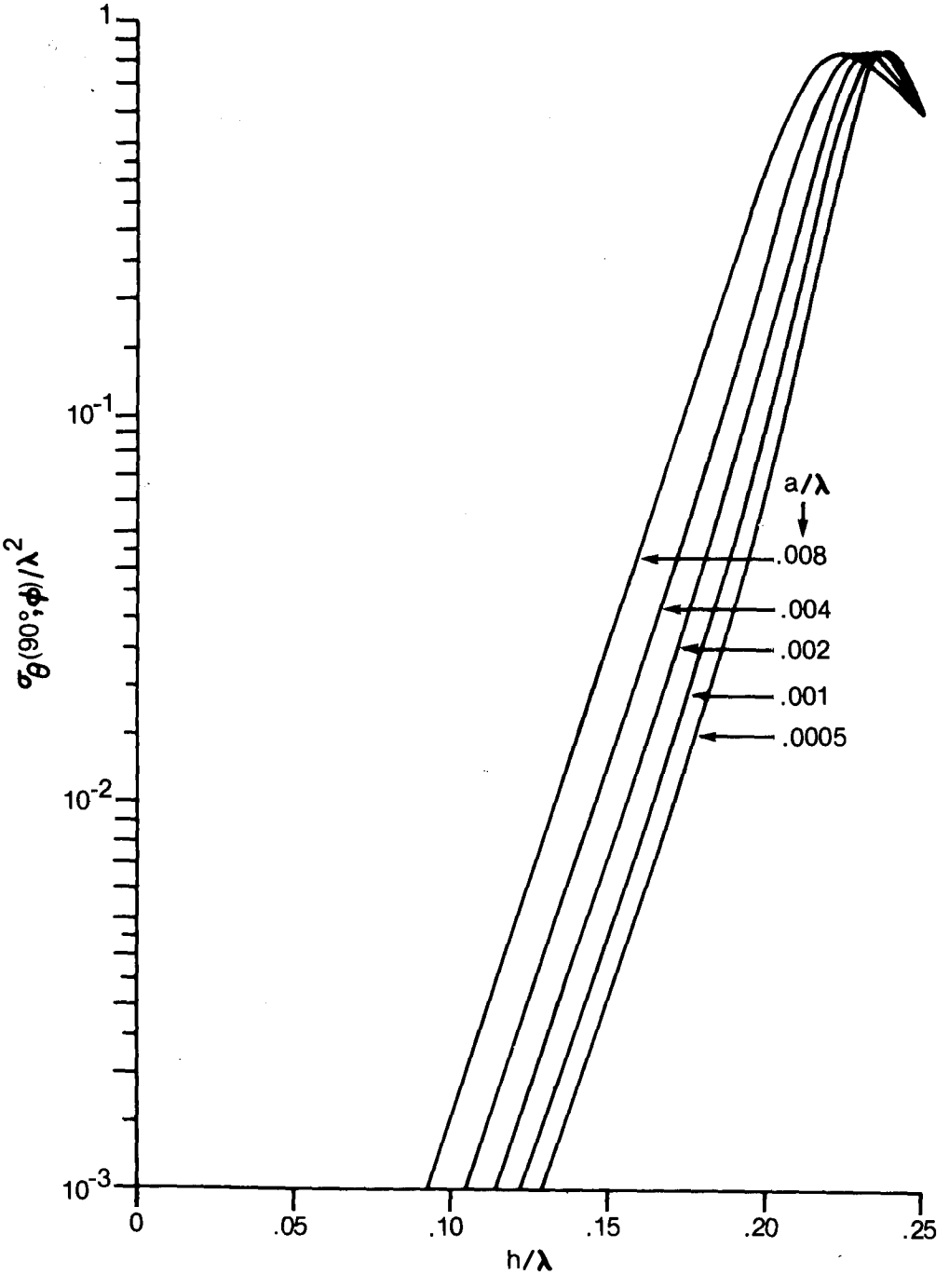

Fig. 5, $\sigma_\theta(90°,\phi)/\lambda^2$ as a function of h/λ, in the region $0 \leqq h/\lambda \leqq .25$, for the structures considered in Fig. 4.

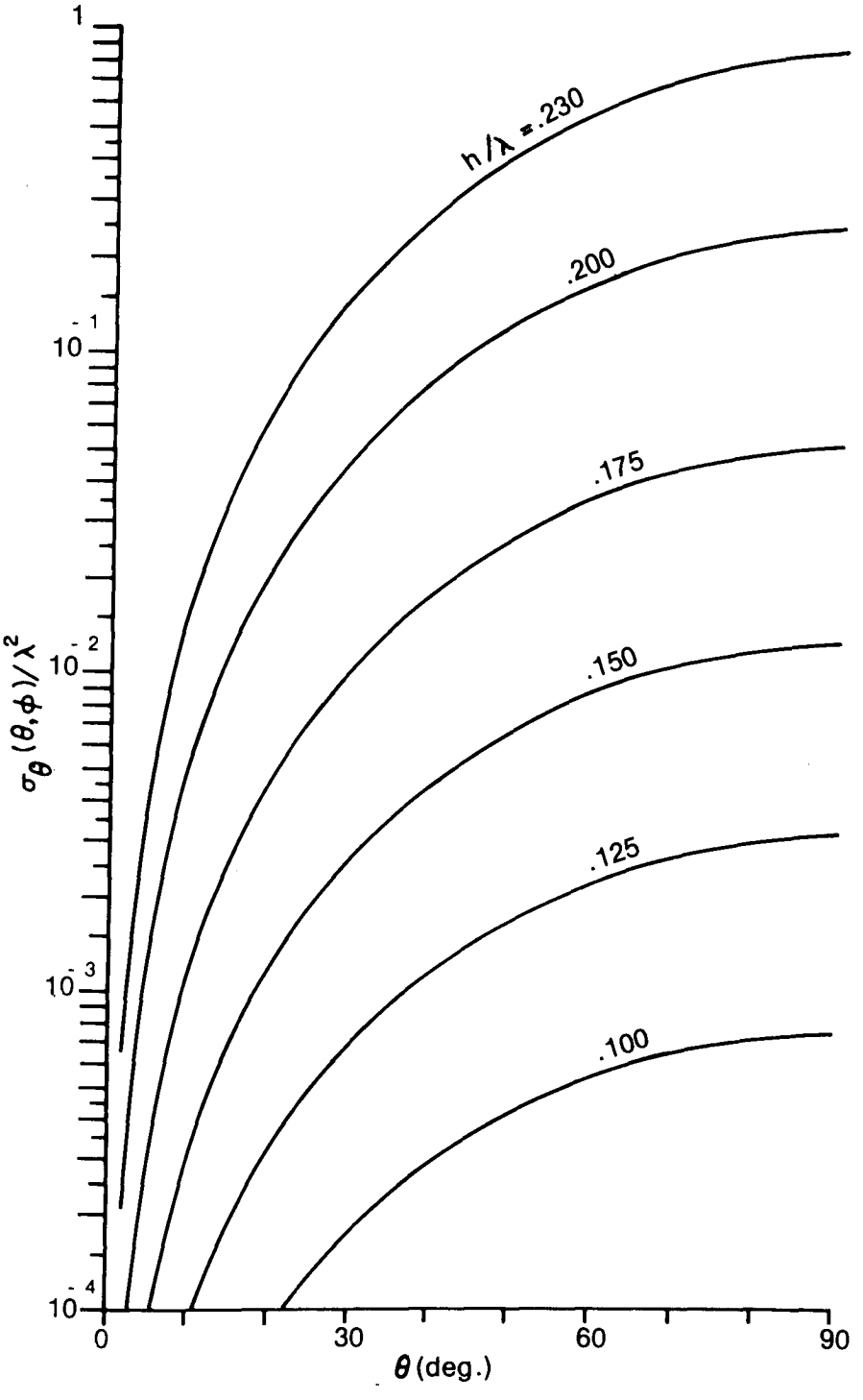

Fig. 6, Vertical $\sigma_\theta(\theta,\phi)/\lambda^2$ patterns for the structure shown in Fig. 4 where $a/\lambda = .004$ and $.100 \leqq h/\lambda \leqq .230$.

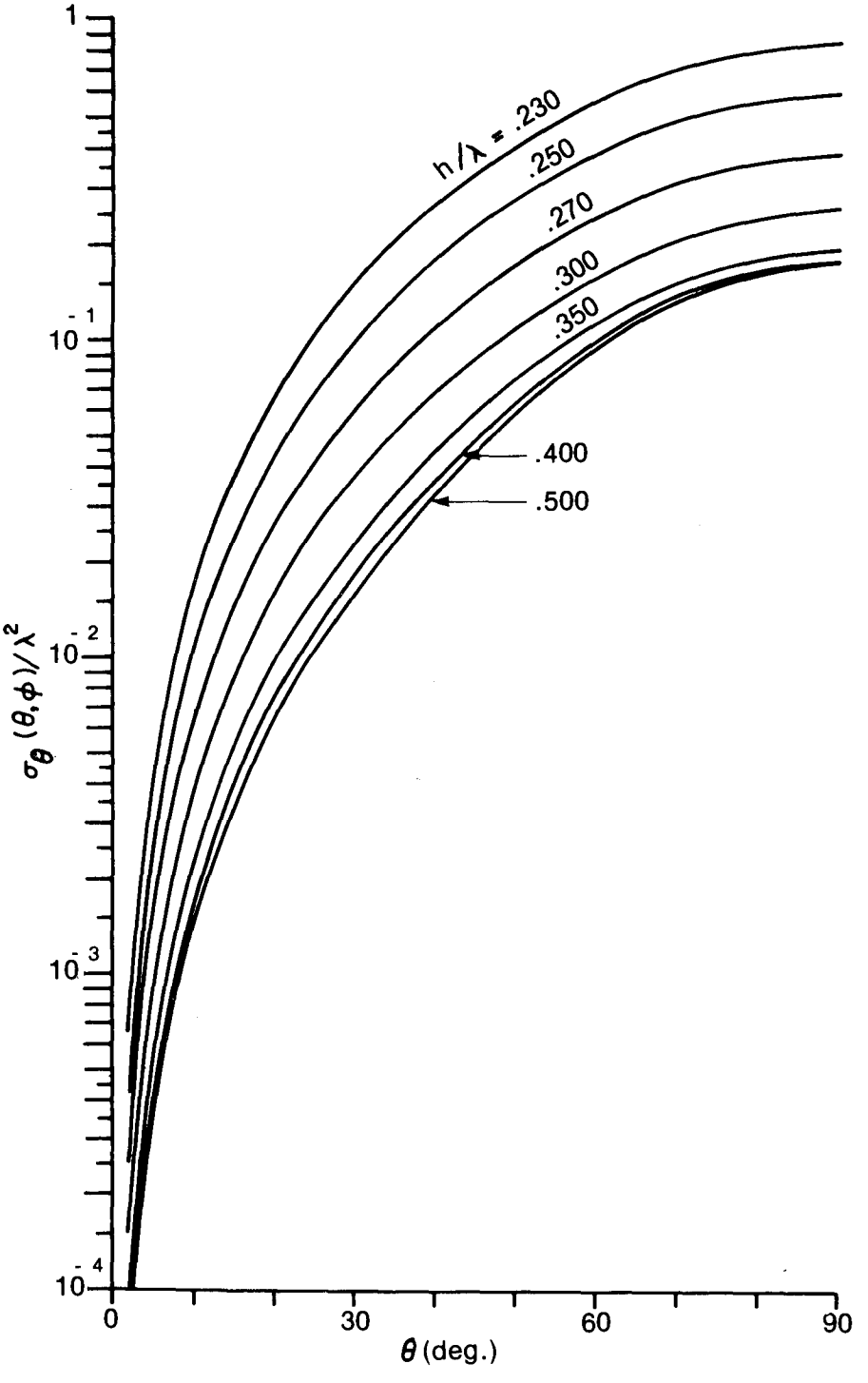

Fig. 7, Vertical $\sigma_\theta(\theta,\phi)/\lambda^2$ patterns for the same structure as used to compute the patterns shown in Fig. 6 except that $.230 \leqq h/\lambda \leqq .500$.

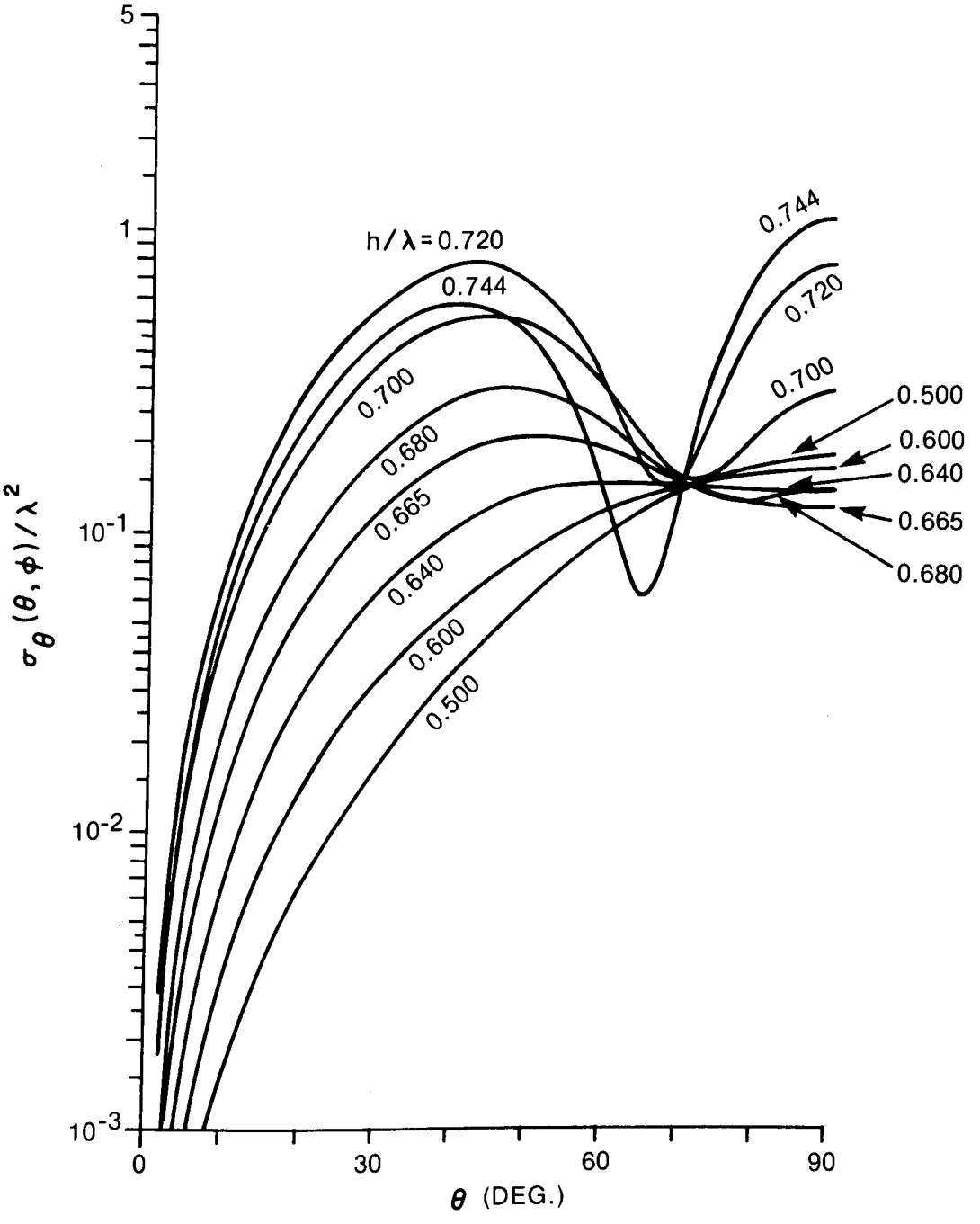

Fig. 8, Vertical $\sigma_\theta(\theta,\phi)/\lambda^2$ patterns for the same structure as was used to compute the patterns shown in Fig. 6 except that $.500 \leq h/\lambda \leq .744$.

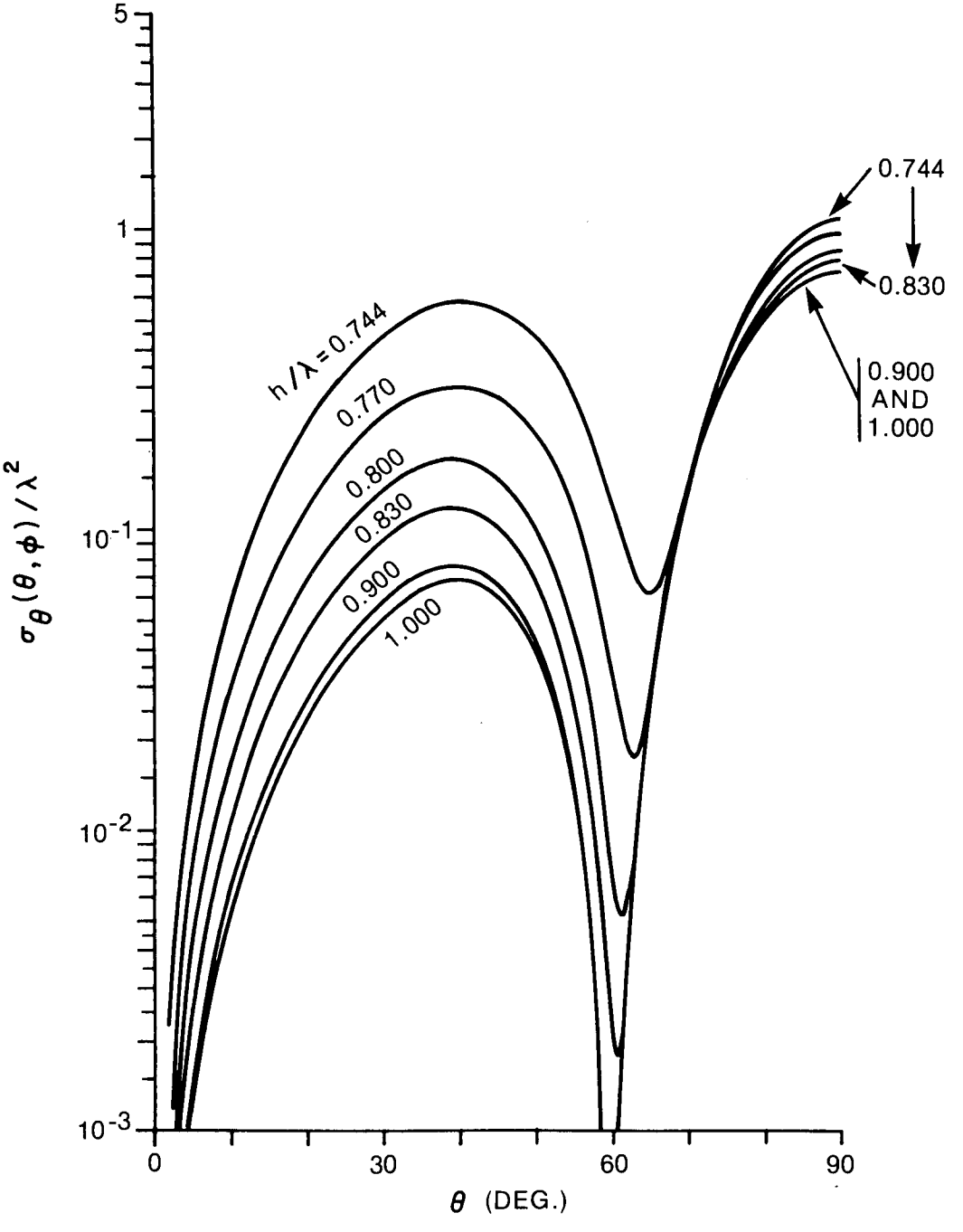

Fig. 9, Vertical $\sigma_\theta(\theta,\phi)/\lambda^2$ patterns for the same structure as was used to compute the patterns shown in Fig. 6 except that $.744 \leqq h/\lambda \leqq 1.000$.

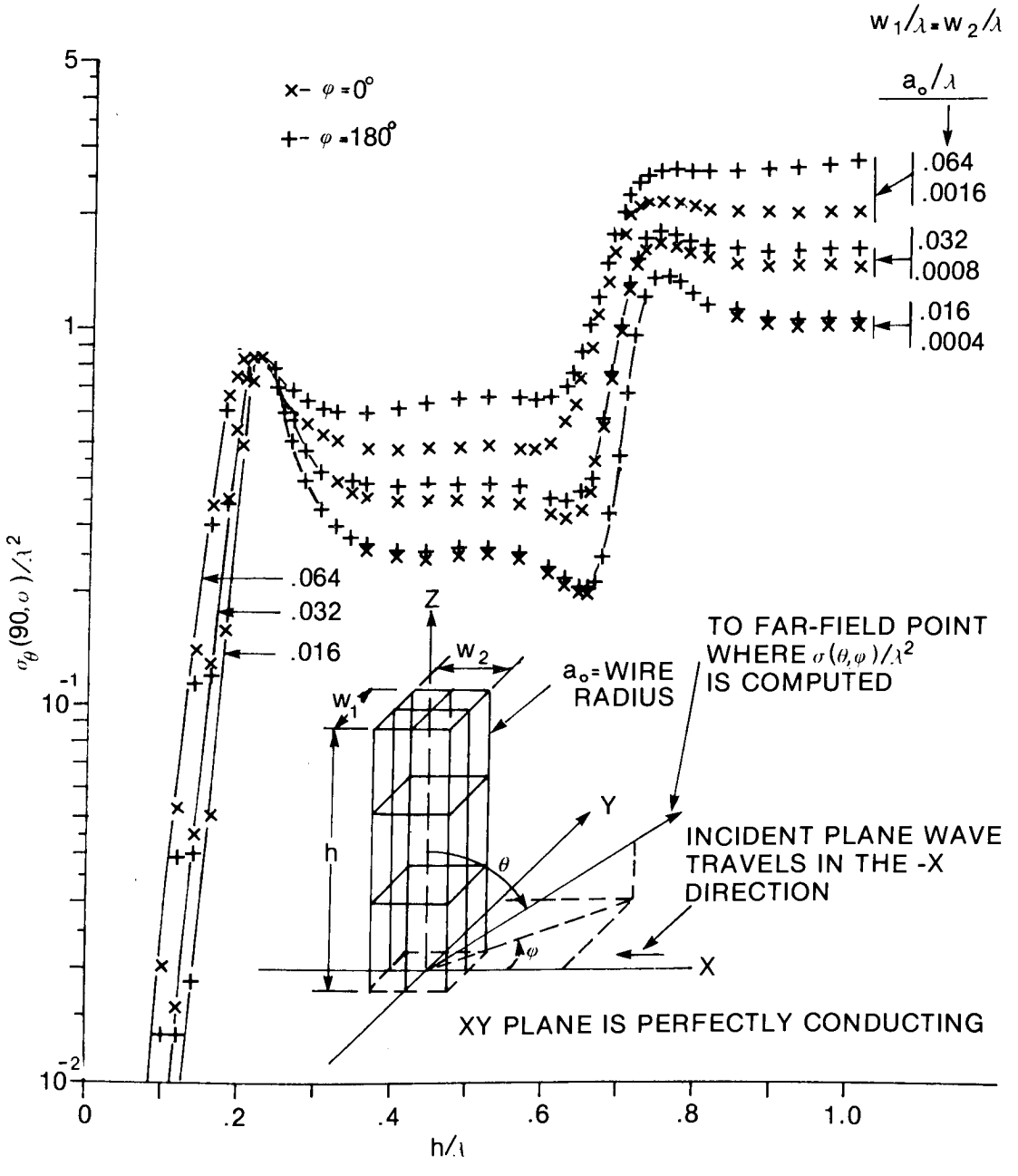

Fig. 10, $\sigma_\theta(90°,\phi)/\lambda^2$ as a function of h/λ for wire grid structures where $w_1/\lambda = w_2/\lambda$ range between .016 and .064.

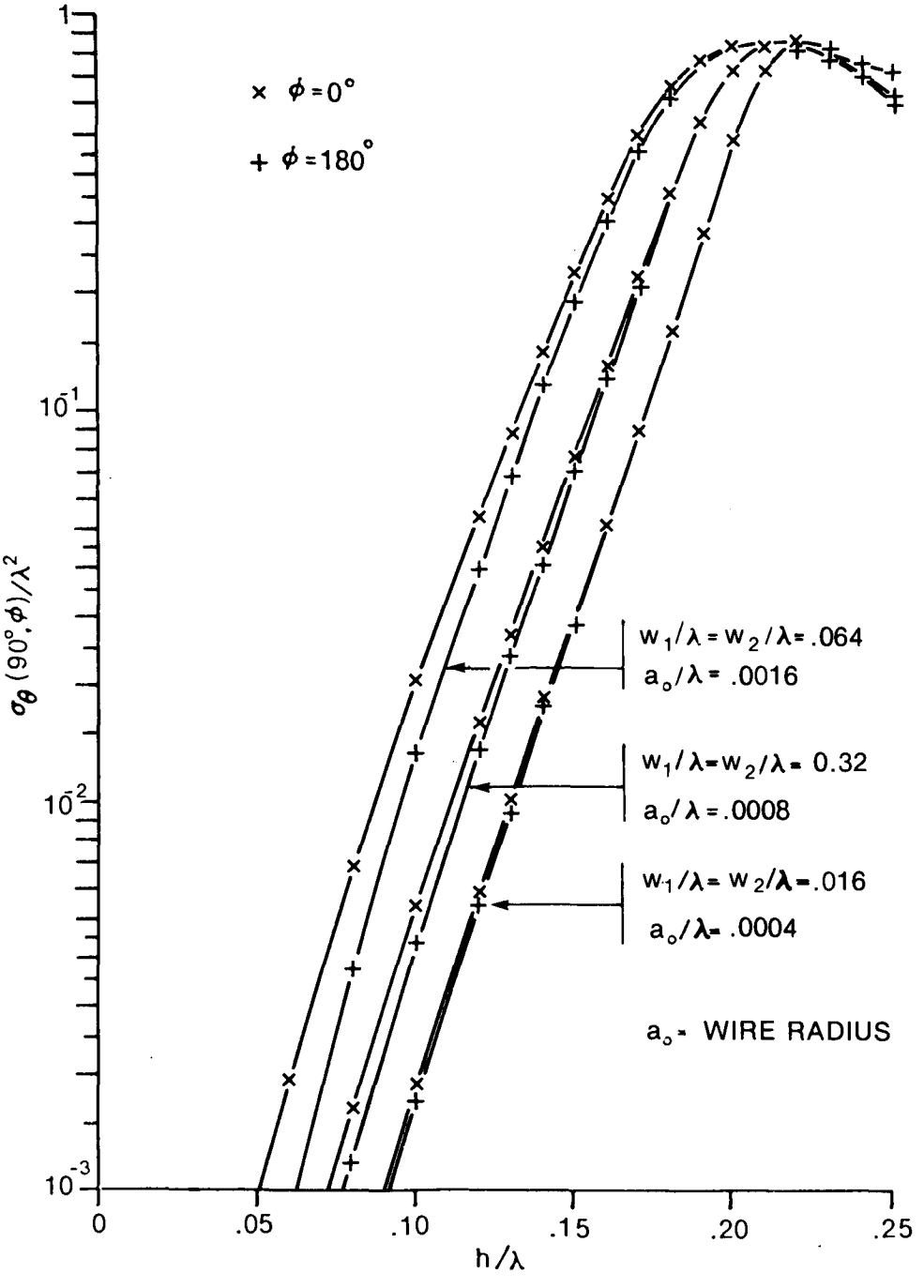

Fig. 11, $\sigma_\theta(90°,\phi)/\lambda^2$ as a function of h/λ, in the region $0 \leqq h/\lambda \leqq .25$, for the structures considered in Fig. 10.

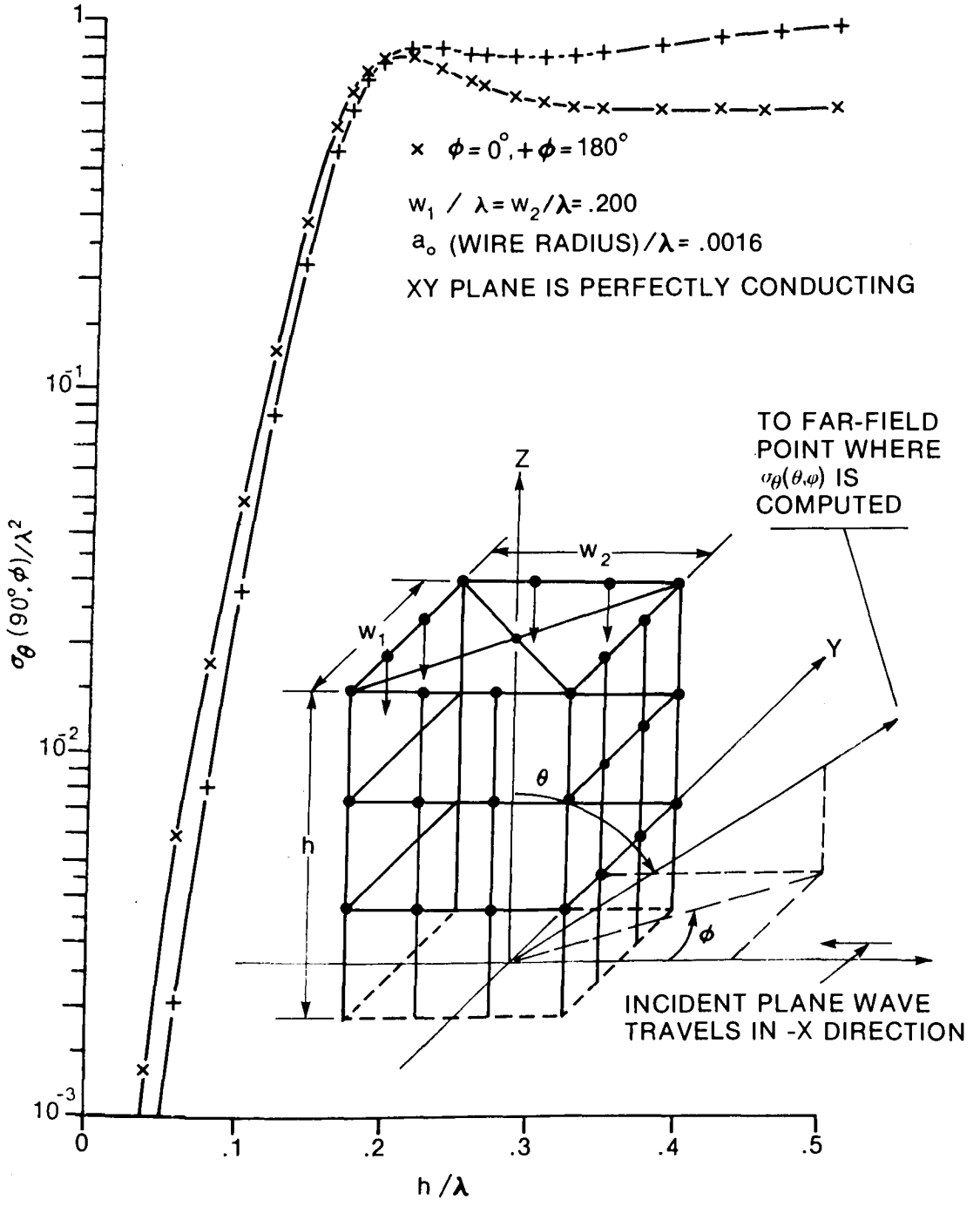

Fig. 12, $\sigma_\theta(90°,\phi)/\lambda^2$ as a function of h/λ for a wire-grid building whose dimensions in horizontal cross-section are .1λx.1λ.

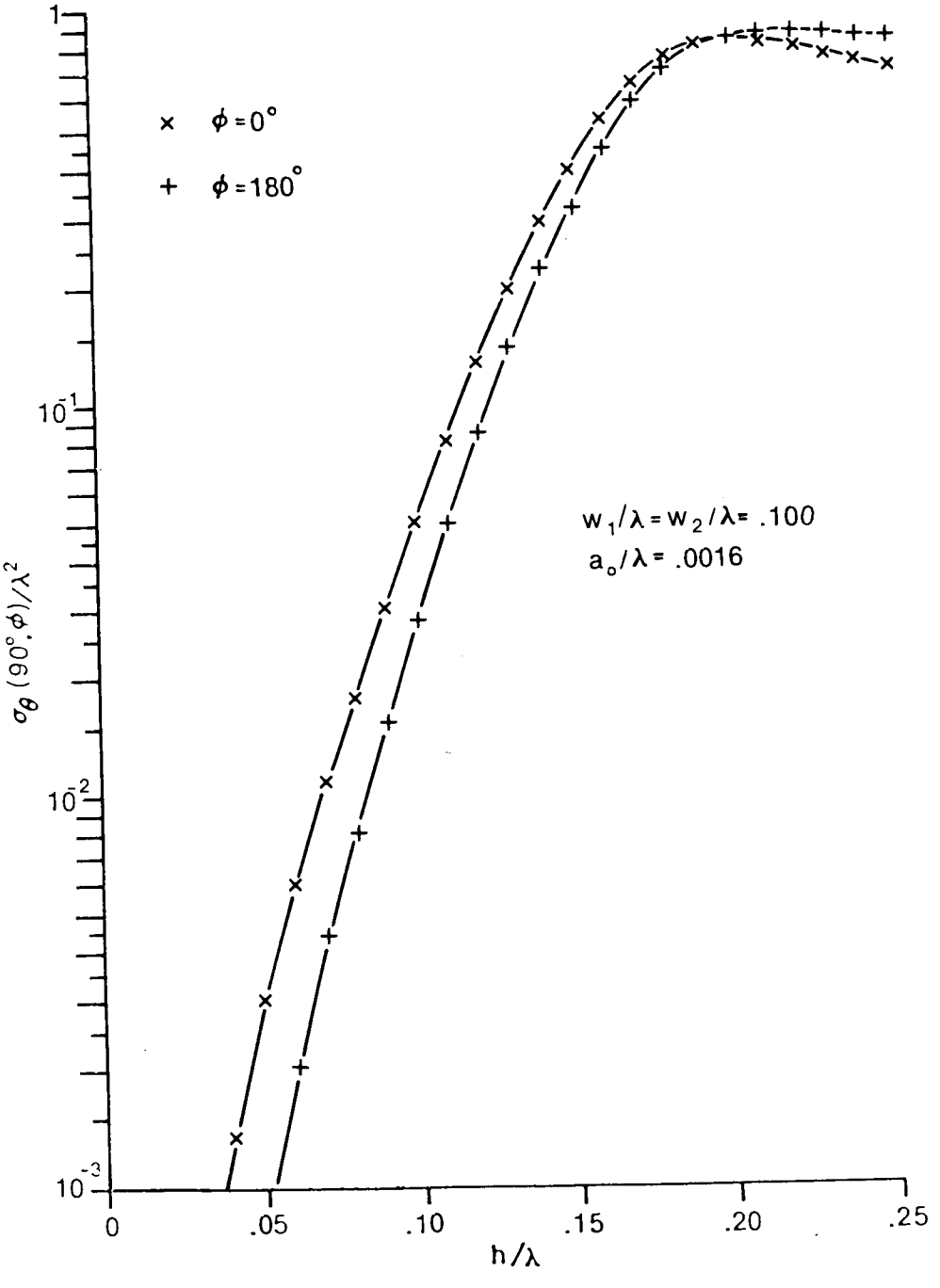

Fig. 13, $\sigma_\theta(90°,\phi)/\lambda^2$ as a function of h/λ, in the region $0 \leqq h/\lambda \leqq .25$, for the structure shown in Fig. 12.

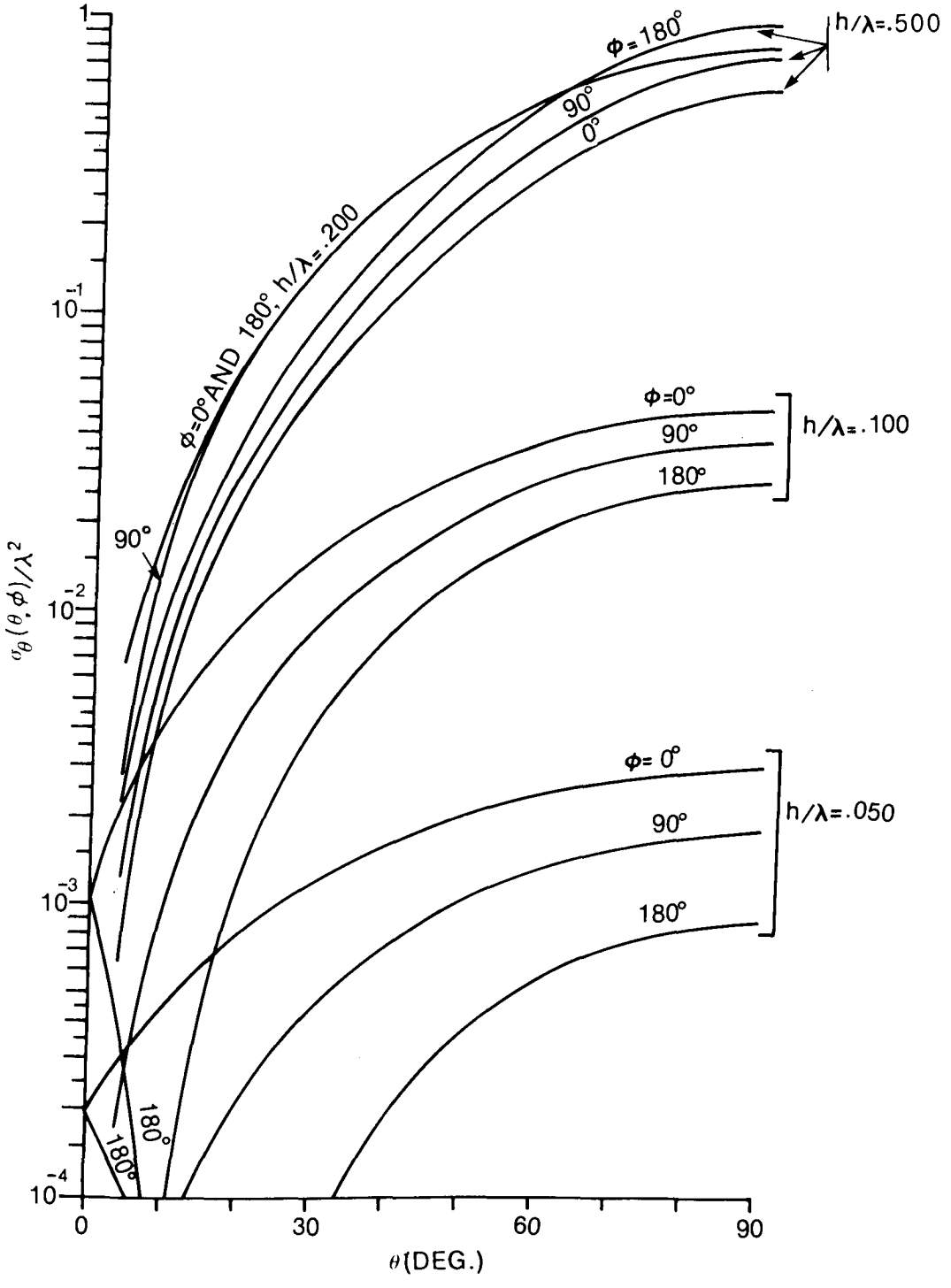

Fig. 14, Vertical $\sigma_\theta(\theta,\phi)/\lambda^2$ patterns for the structure shown in Fig. 12.

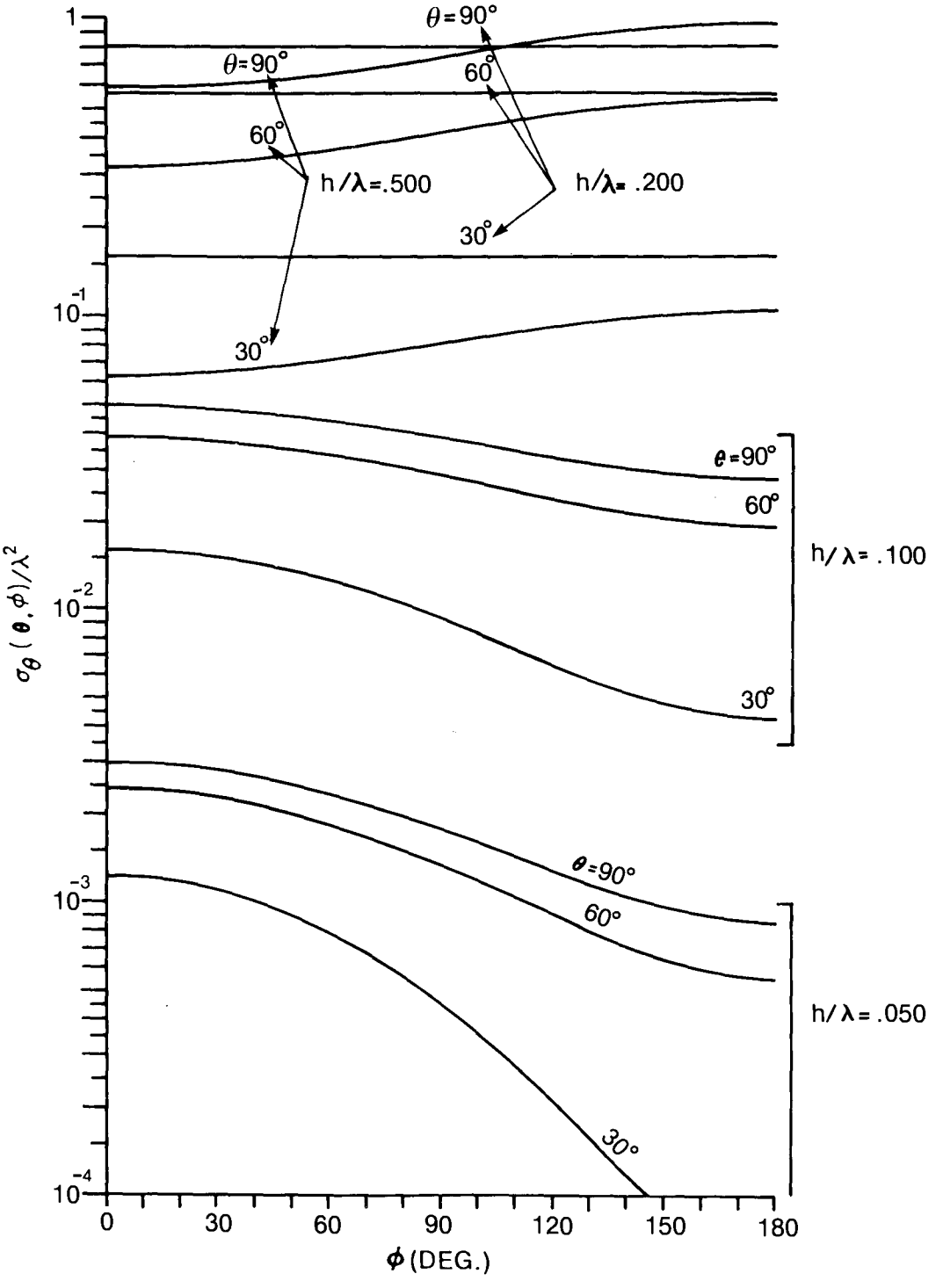

Fig. 15, Horizontal $\sigma_\theta(\theta,\phi)/\lambda^2$ patterns for the structure shown in Fig. 12.

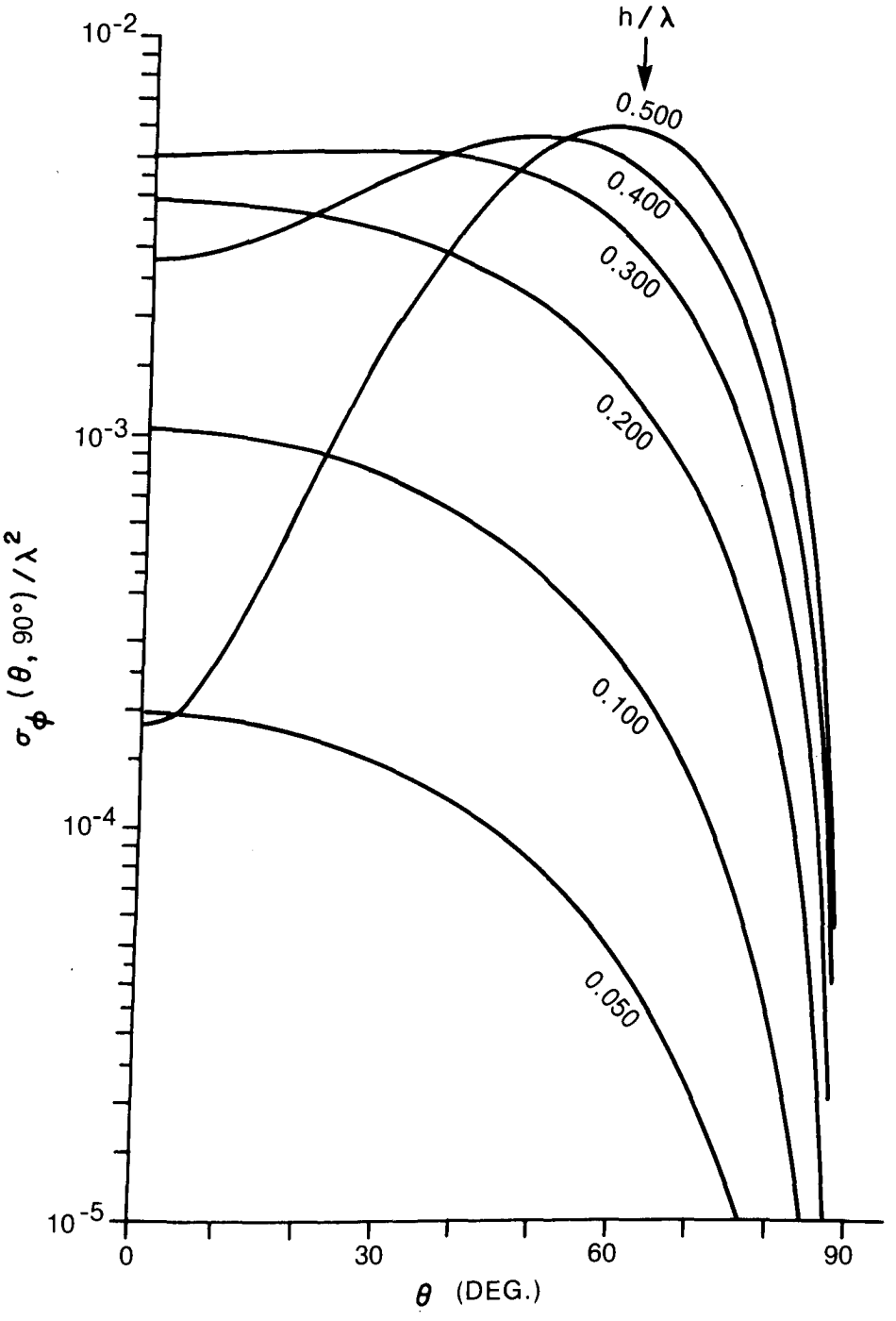

Fig. 16, Vertical $\sigma_\phi(\theta,\phi)/\lambda^2$ patterns, at ϕ=90°, for the structure shown in Fig. 12. Note that the subscript ϕ for σ indicates the above are ϕ (or horizontally) polarized patterns.

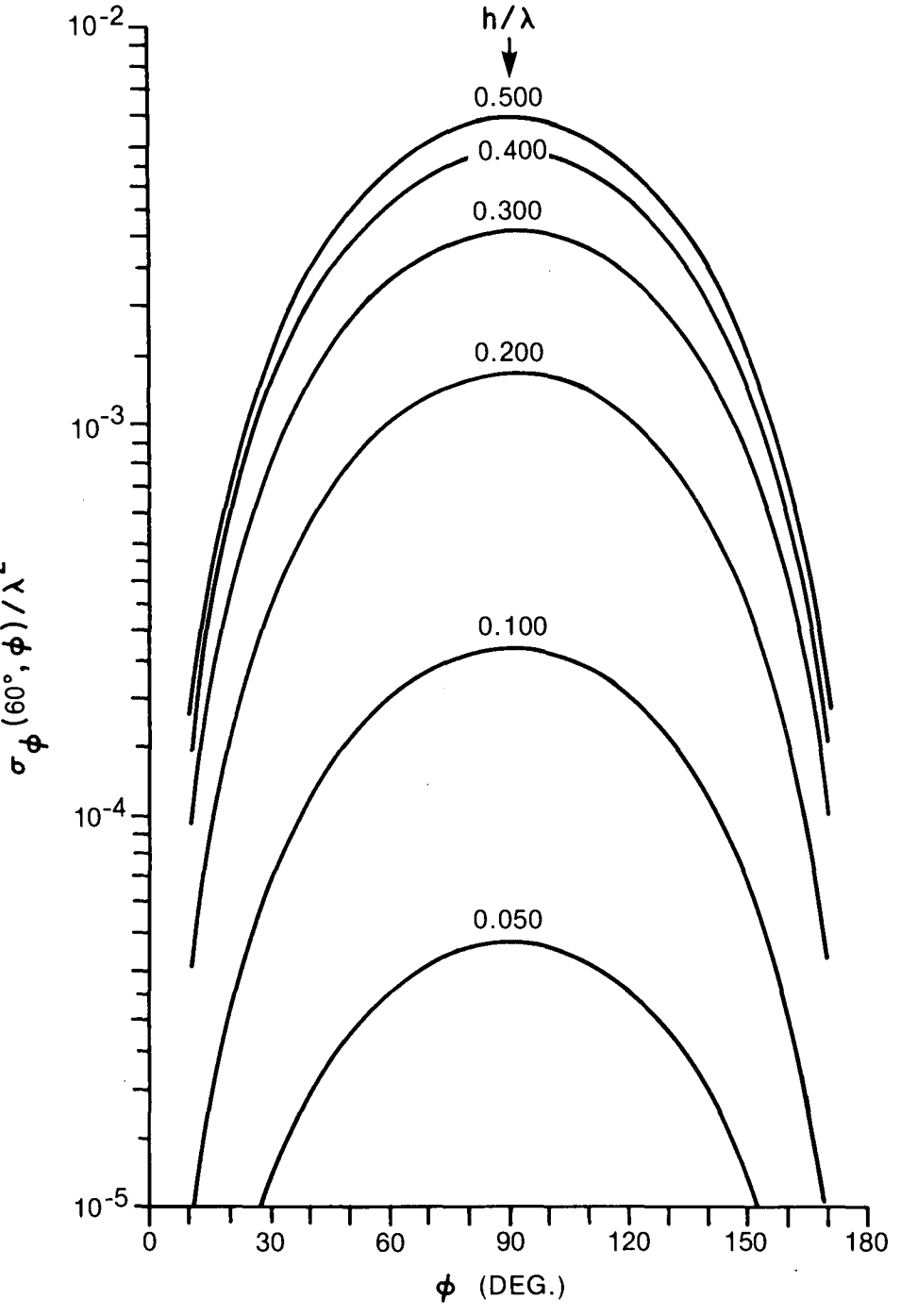

Fig. 17, Horizontal $\sigma_\phi(60°,\phi)/\lambda^2$ patterns, at θ=60°, for the structure shown in Fig. 12.

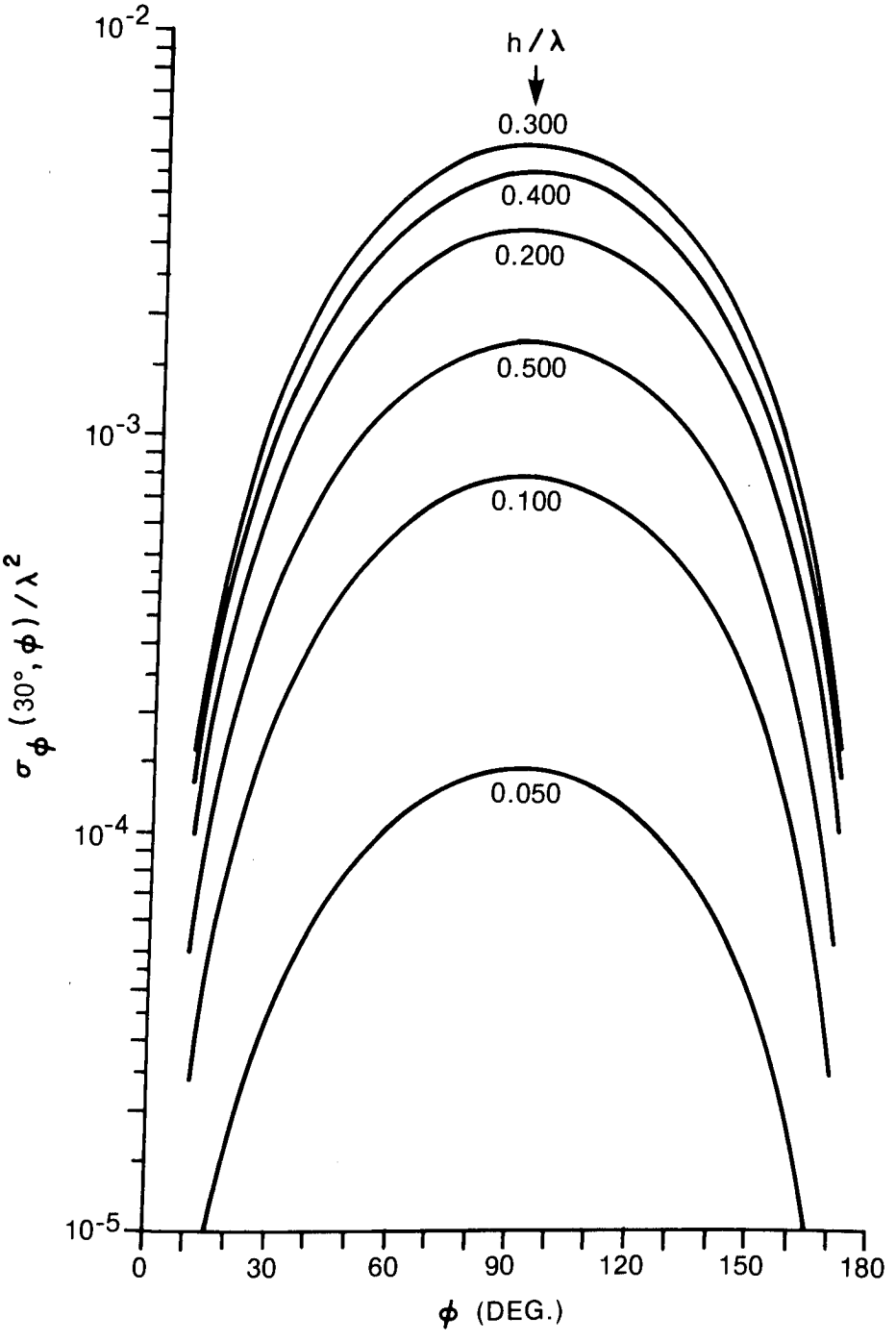

Fig. 18, Horizontal $\sigma_\phi(30°,\phi)/\lambda^2$ patterns, at θ=30°, for the structure shown in Fig. 12.

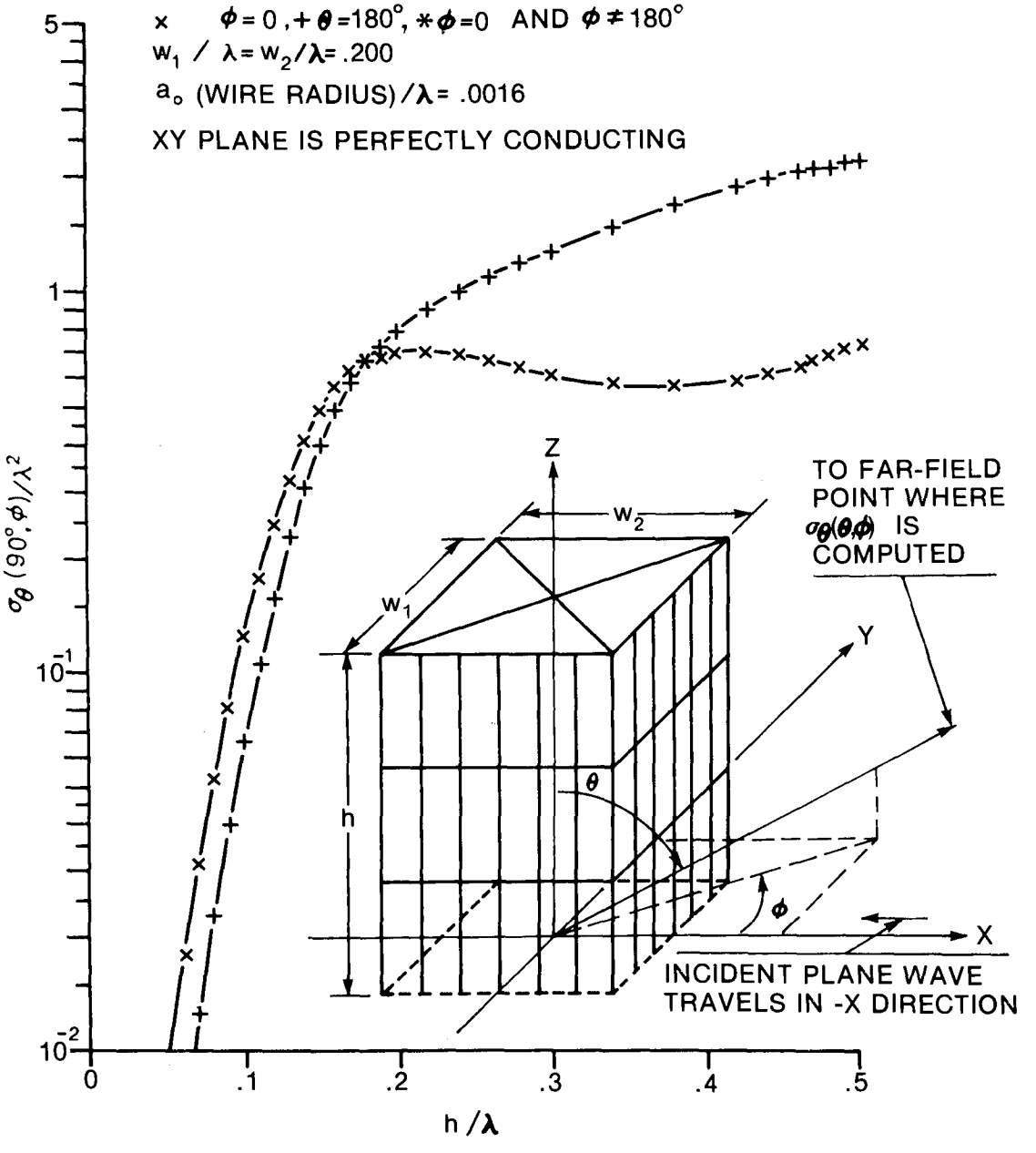

Fig. 19, $\sigma_\theta(90°,\phi)/\lambda^2$ as a function of h/λ for the wire-grid building shown. Note, although not indicated, the wire grids for the $x/\lambda=-.1$ and $y/\lambda=.1$ sides are the same as shown for the $x/\lambda=.1$ and $y/\lambda=-.1$ sides.

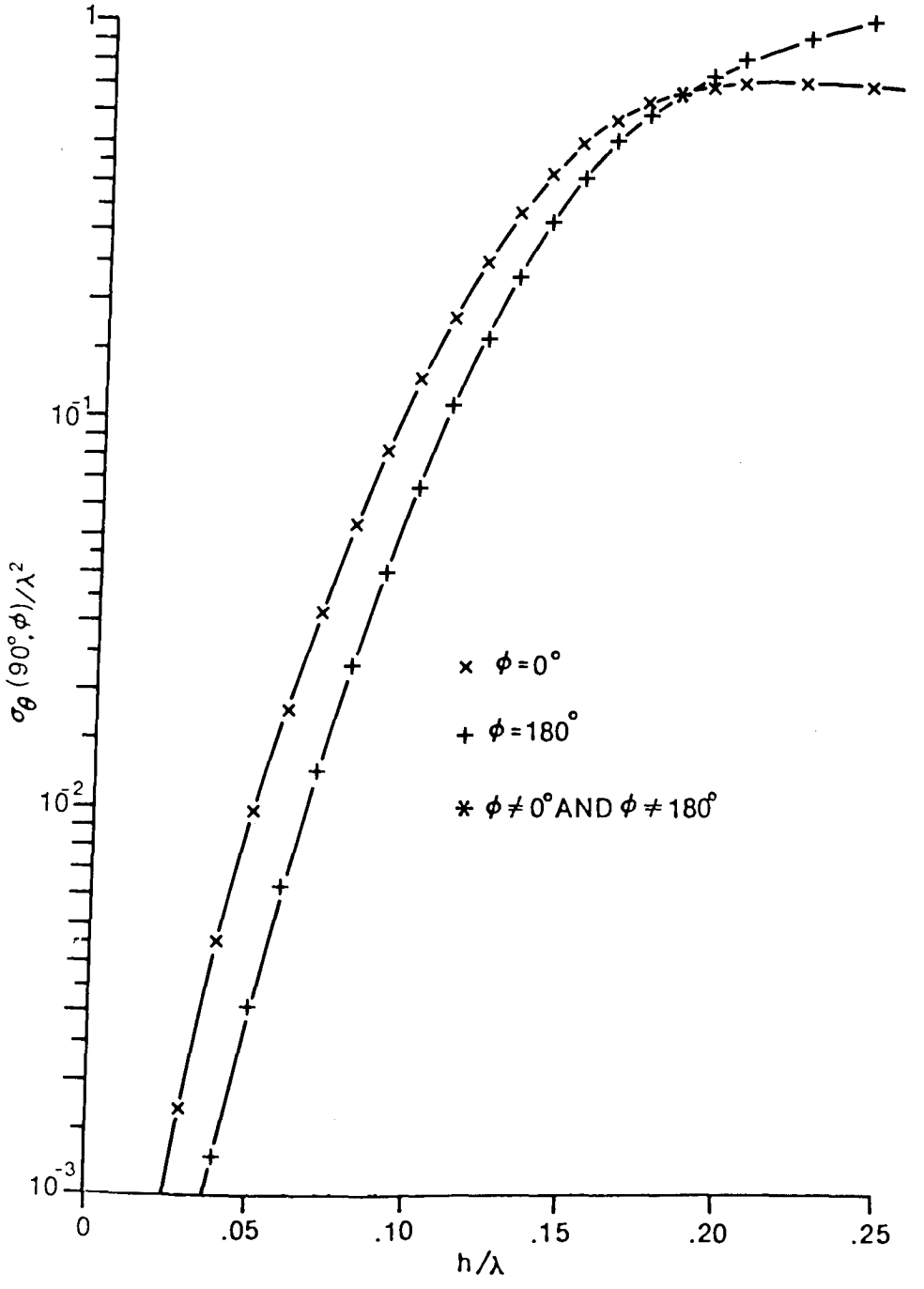

Fig. 20, $\sigma_\theta(90°,\phi)/\lambda^2$ as a function of h/λ, in the region $0 \leqq h/\lambda \leqq .25$, for the wire-grid building shown in Fig. 19.

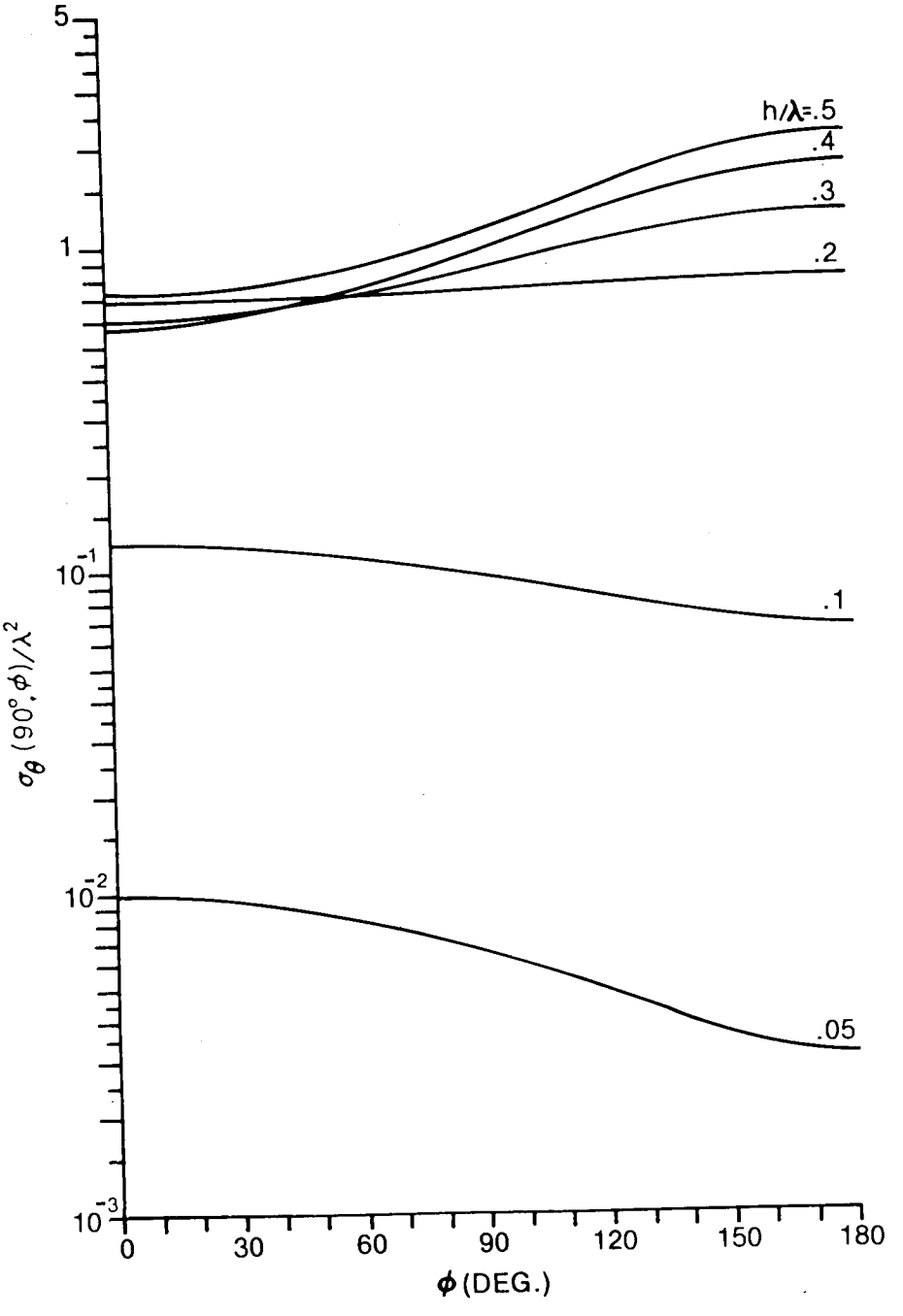

Fig. 21, $\sigma_\theta(90°,\phi)/\lambda^2$ as a function of ϕ for the wire-grid building shown in Fig. 19.

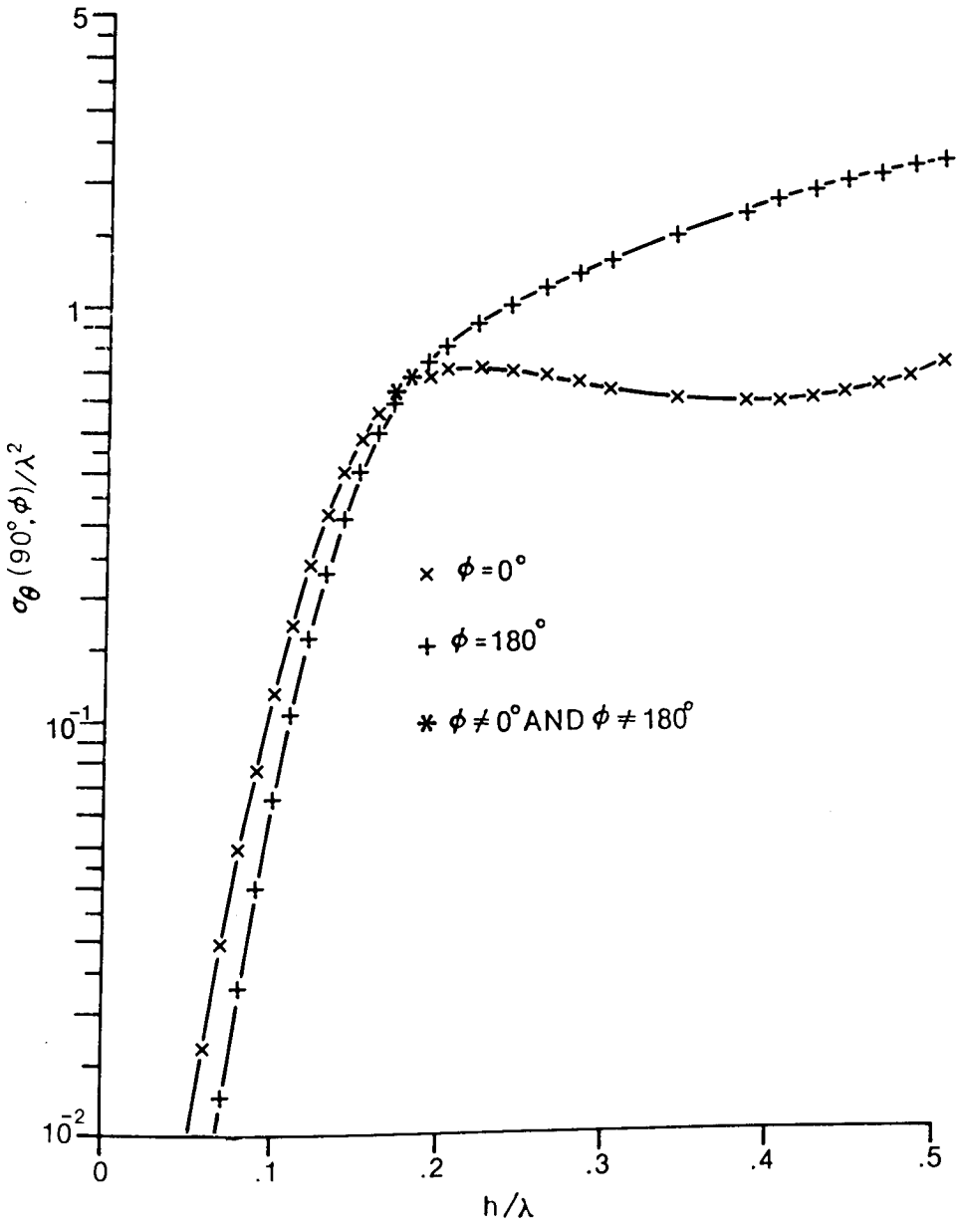

Fig. 22, $\sigma_\theta(90°,\phi)/\lambda^2$ as a funtion of h/λ for the wire-grid building shown in Fig. 19 except that the building has been rotated about the Z axis through 45°.

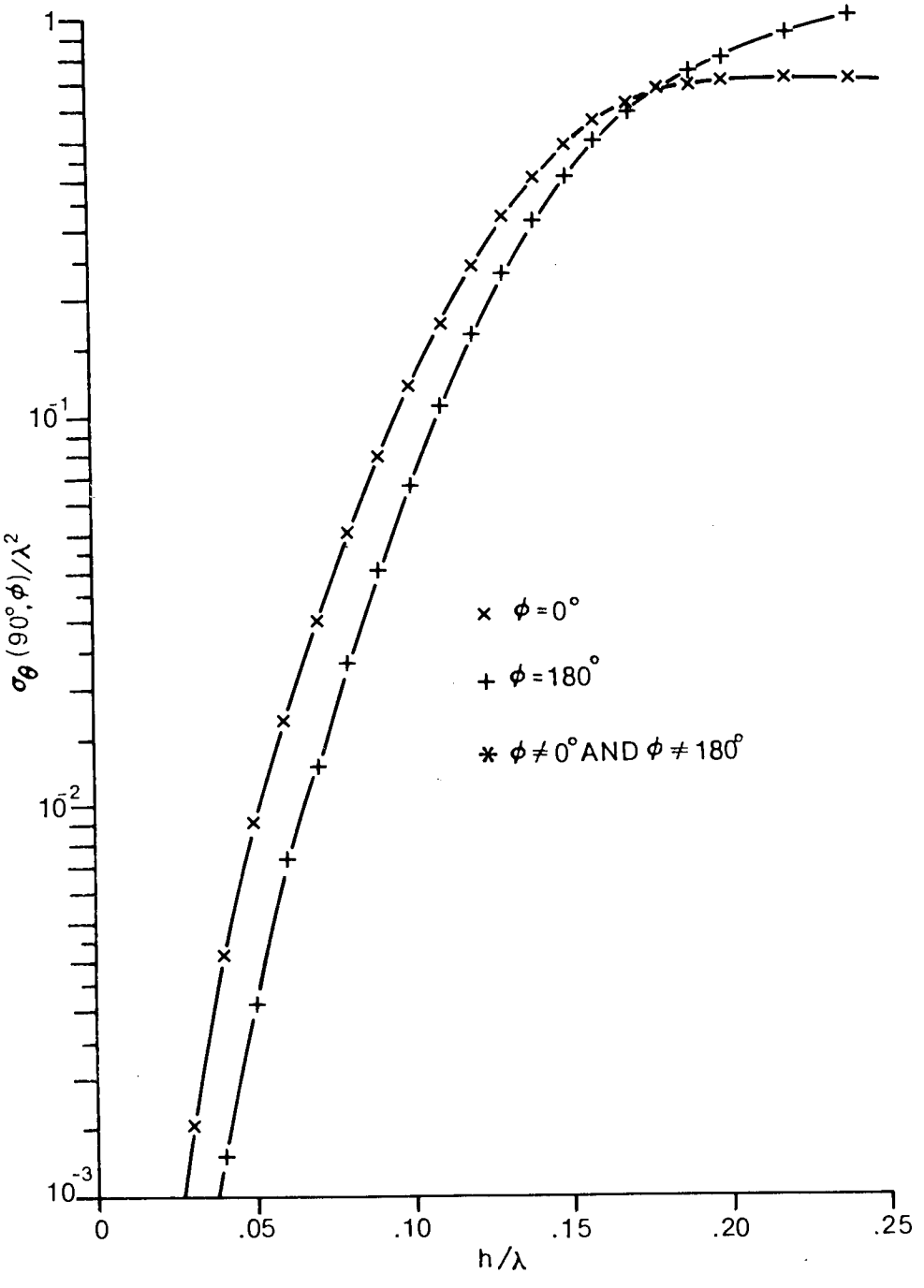

Fig. 23, $\sigma_\theta(90°,\phi)/\lambda^2$ as a function of h/λ. in the region $0 \leqq h/\lambda \leqq .25$, for the structure considered in Fig. 22.

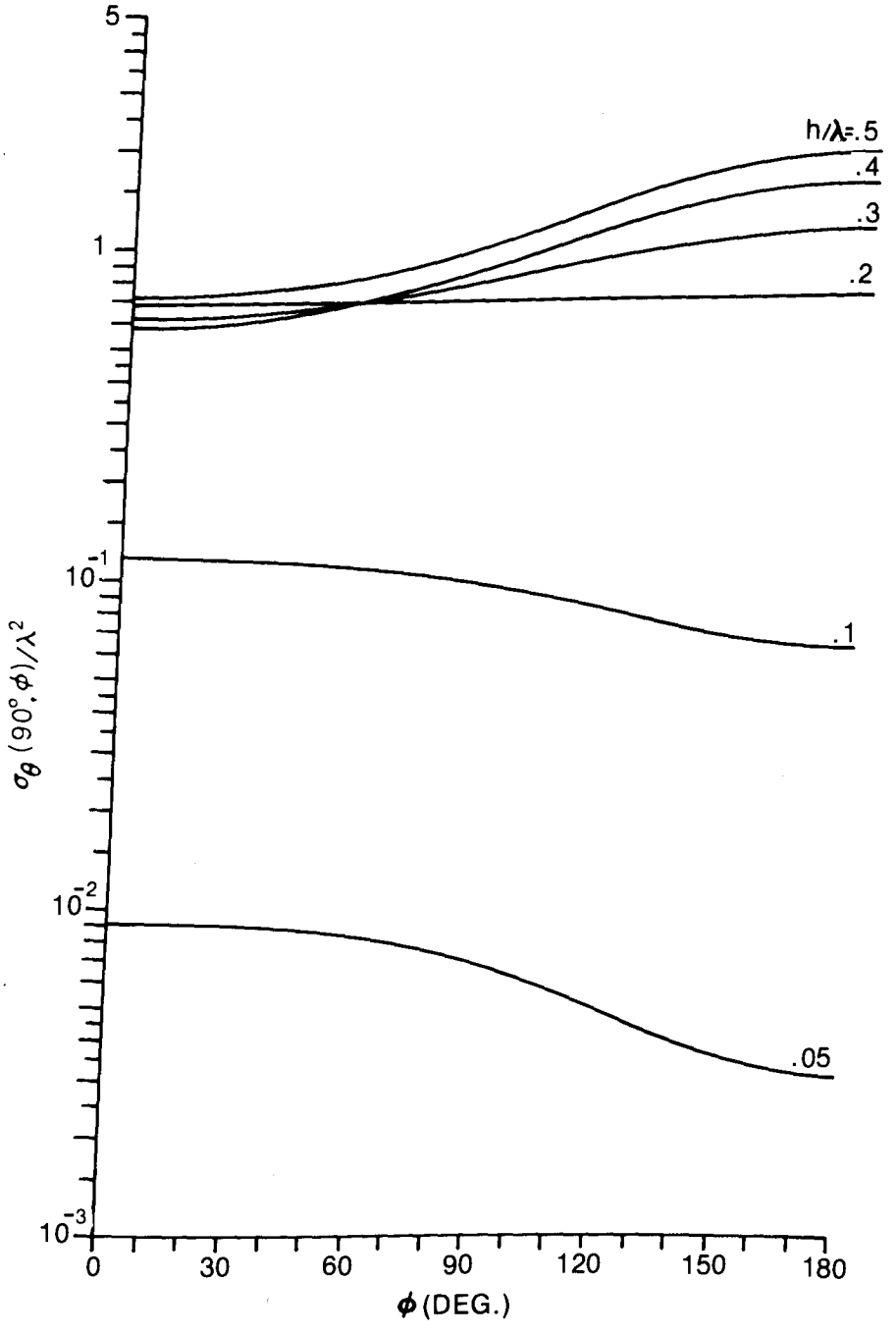

Fig. 24, $\sigma_\theta(90°,\phi)/\lambda^2$ as a function of ϕ for Fig. 22's structure.

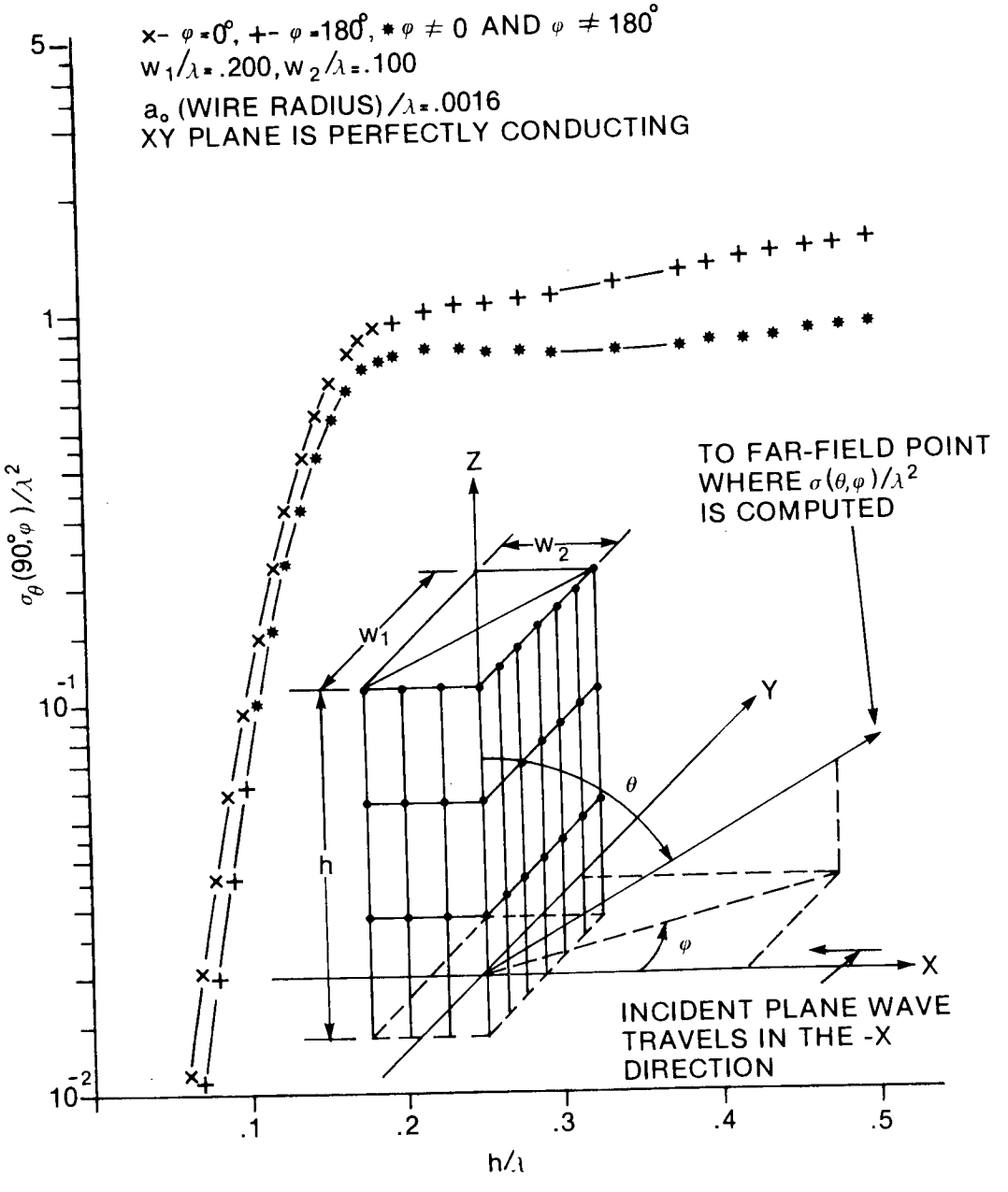

Fig. 25, $\sigma_\theta(90°,\phi)/\lambda^2$ as a function of h/λ for the wire-grid building shown. Note, although not indicated, the wire grids for the $x/\lambda=-.05$ and $y/\lambda=.1$ sides are the same as shown for respectively the $x/\lambda=.05$ and $y/\lambda=-.1$ sides.

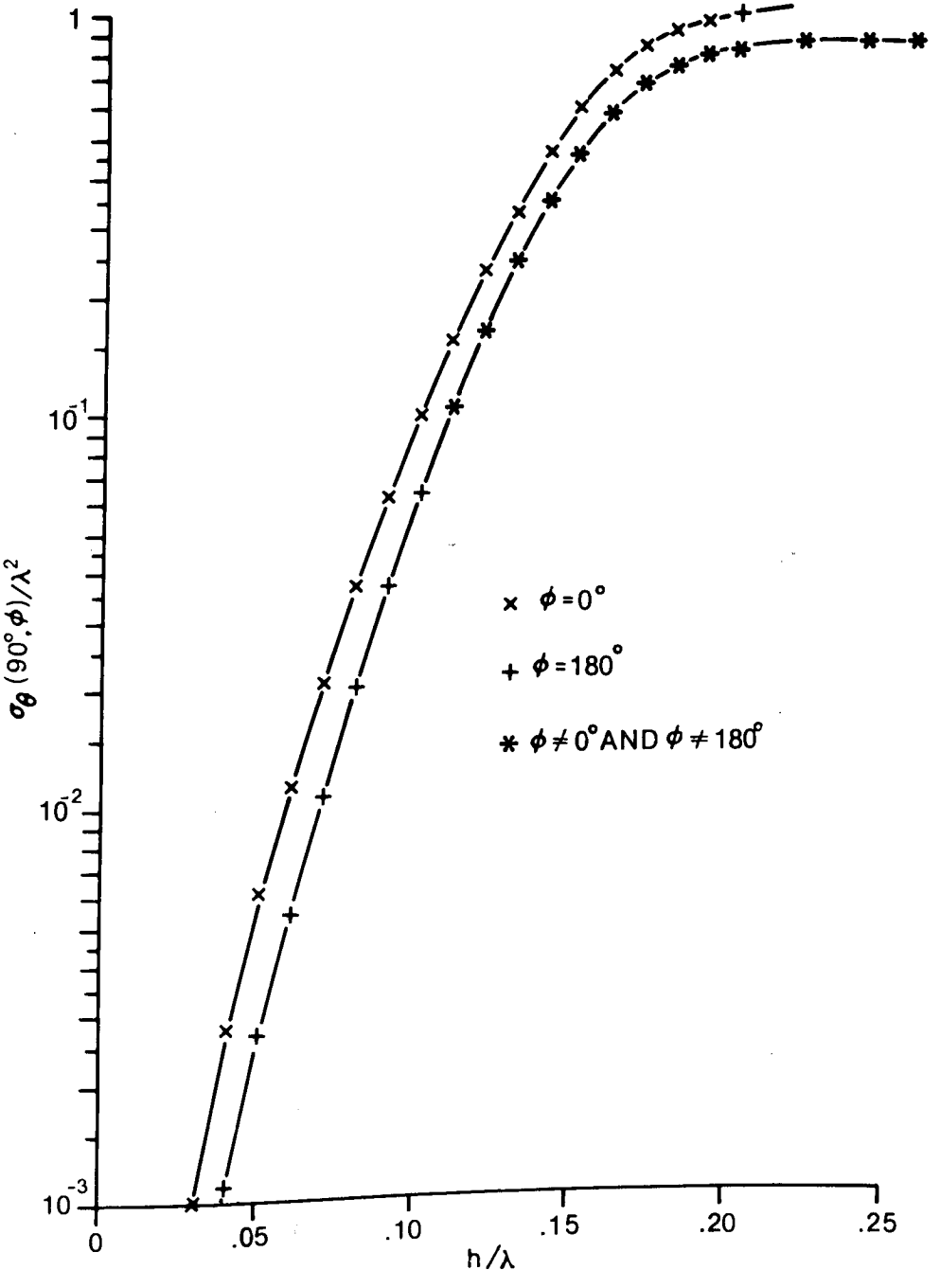

Fig. 26, $\sigma_\theta(90°,\phi)/\lambda^2$ as a function of h/λ, in the region $0 \leqq h/\lambda \leqq .25$, for the wire-grid building shown in Fig. 25.

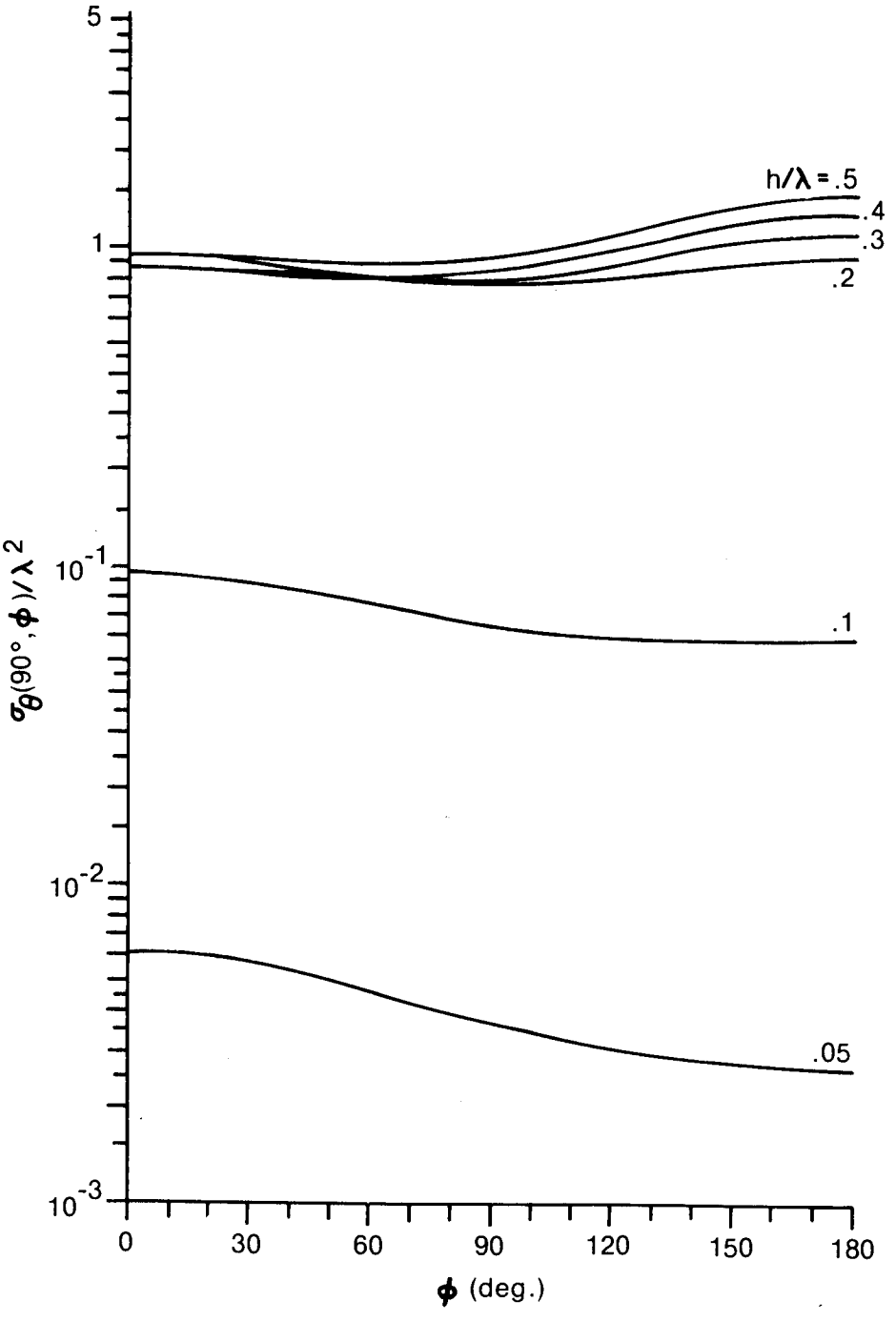

Fig. 27, $\sigma_\theta(90°,\phi)/\lambda^2$ as a function of ϕ for Fig. 25's structure.

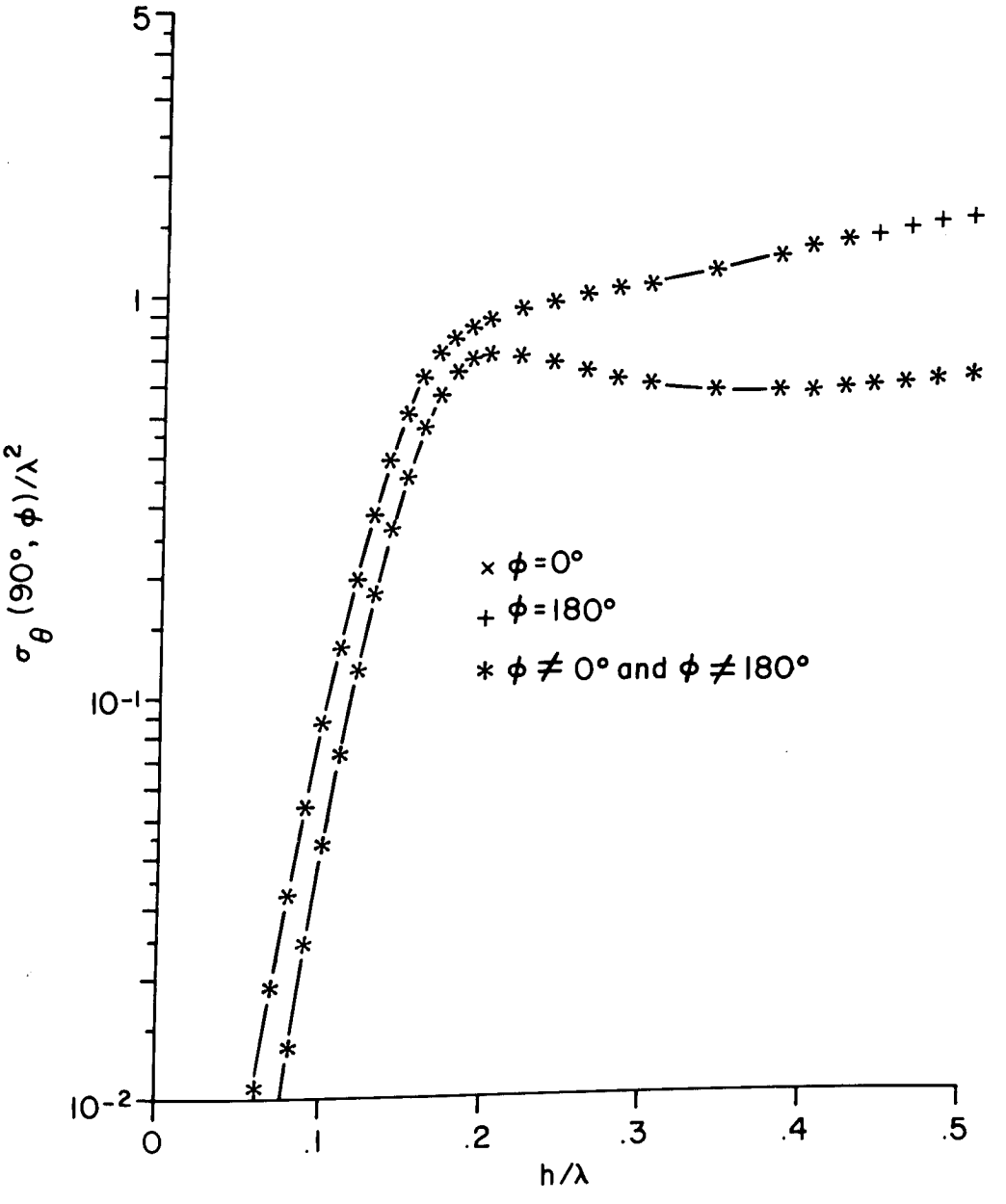

Fig. 28, $\sigma_\theta(90°,\phi)/\lambda^2$ as a function of h/λ for the wire-grid building shown in Fig. 25 except that the building has been rotated about the Z axis through 45° in the positive ϕ direction.

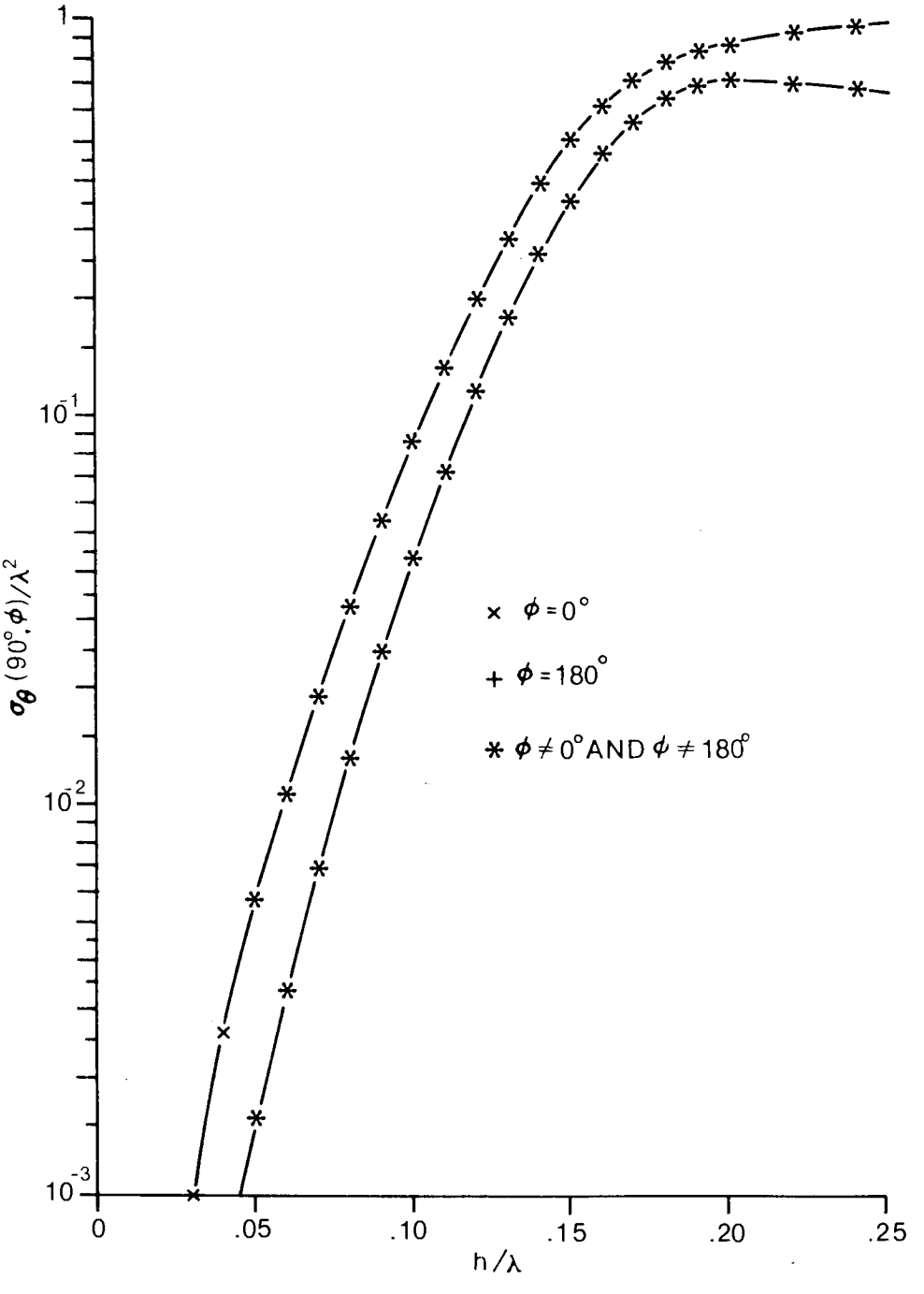

Fig. 29, $\sigma_\theta(90°,\phi)/\lambda^2$ as a function of h/λ, in the region $0 \leq h/\lambda \leq .25$, for the structure considered in Fig. 28.

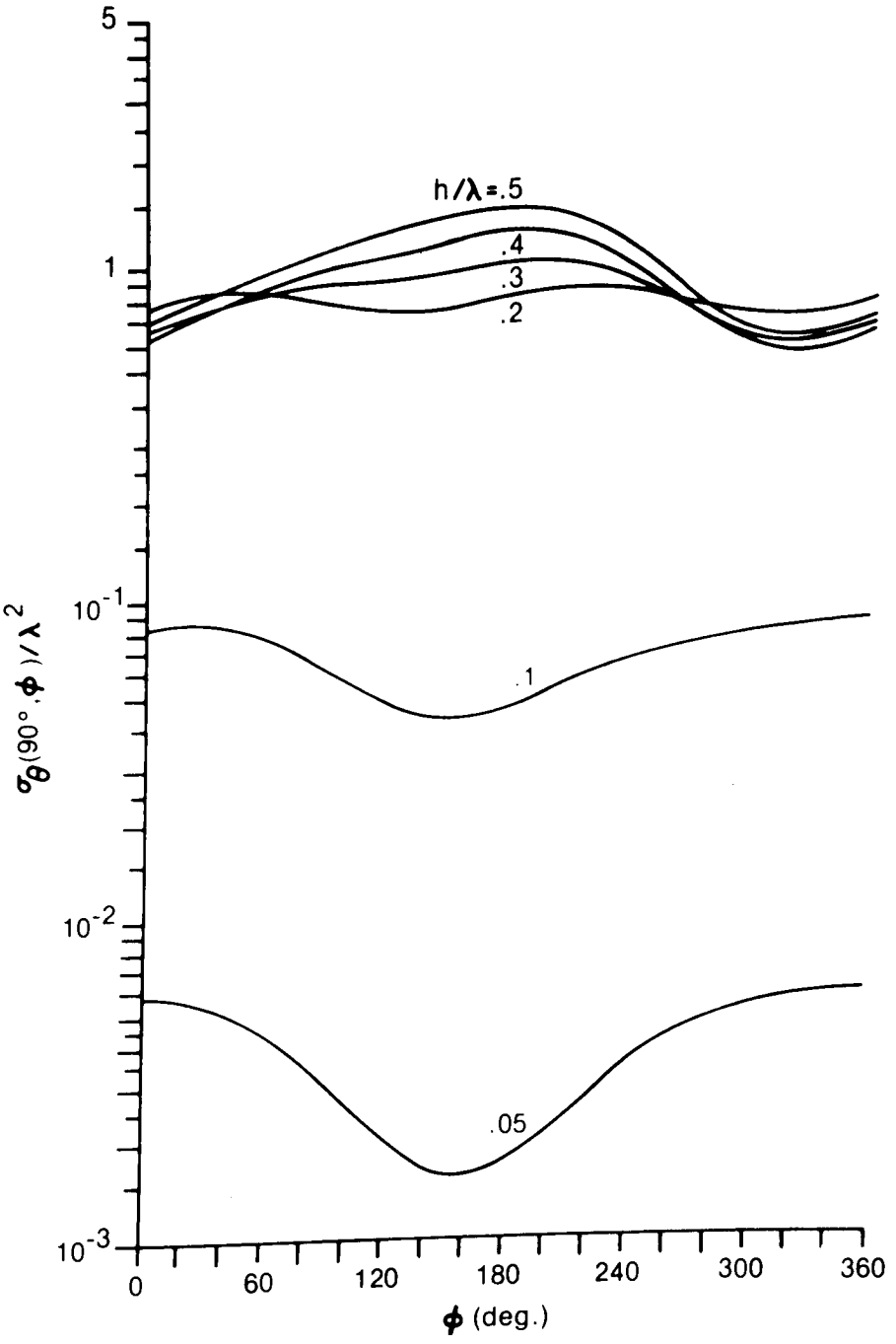

Fig. 30, $\sigma_\theta(90°,\phi)/\lambda^2$ as a function of ϕ for Fig. 28's structure.

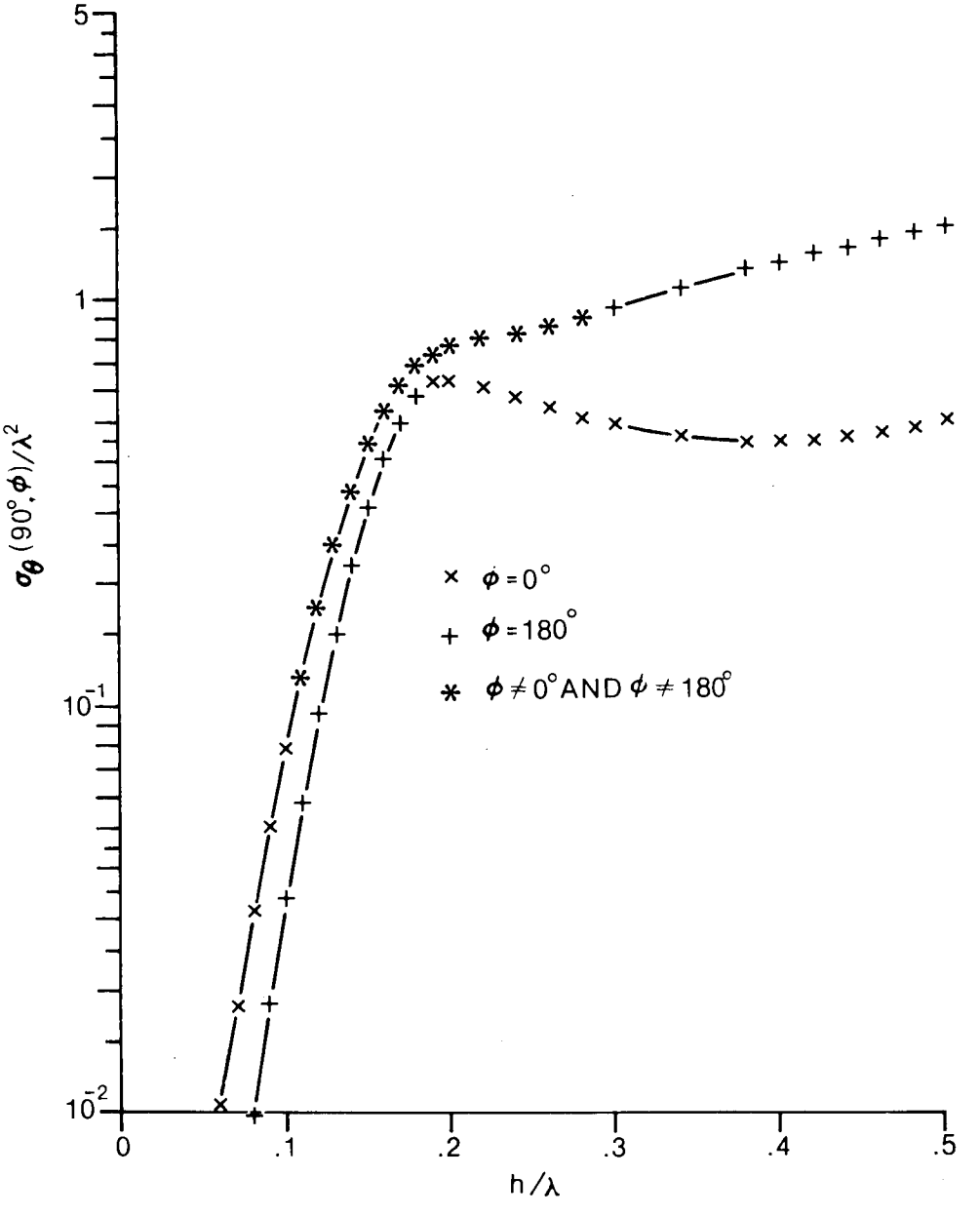

Fig. 31, $\sigma_\theta(90°,\phi)/\lambda^2$ as a function of h/λ, for the wire-grid building shown in Fig. 25 except that the building has been rotated about the Z axis through 90°.

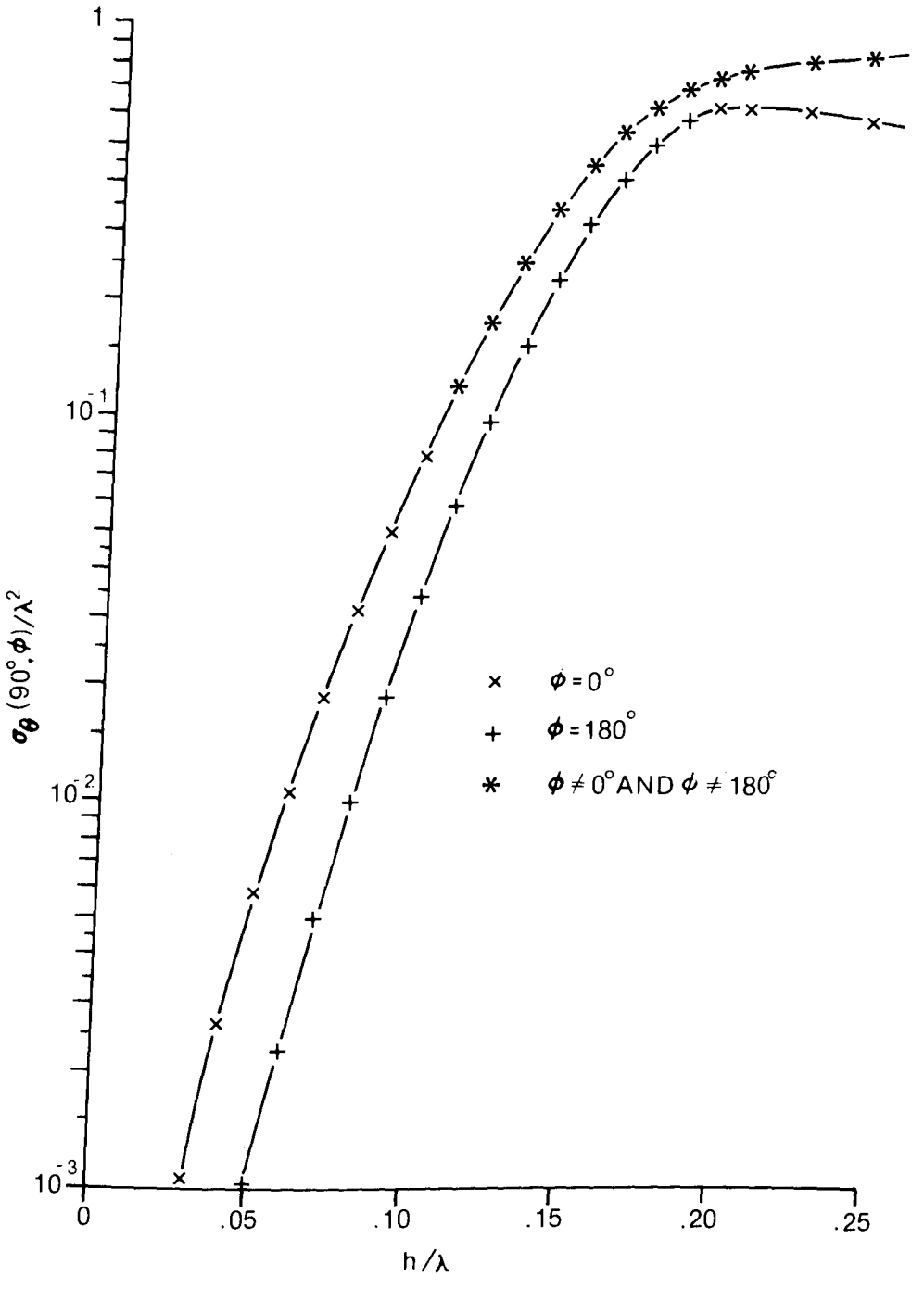

Fig. 32, $\sigma_\theta(90°,\phi)/\lambda^2$ as a function of h/λ, in the region $0 \leqq h/\lambda \leqq .25$,

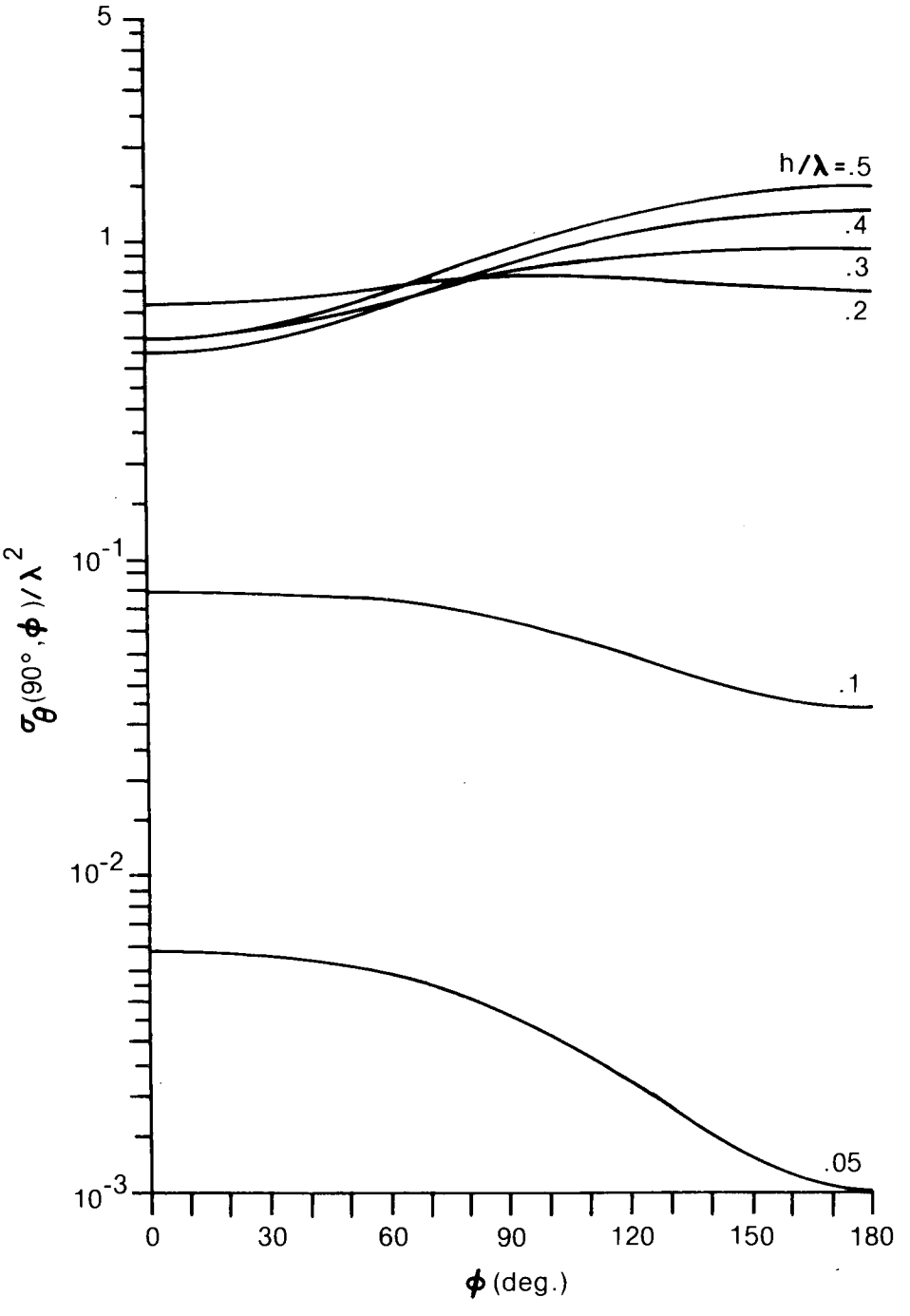

Fig. 33, $\sigma_\theta(90°,\phi)/\lambda^2$ as a function of ϕ for Fig. 31's structure.

4. METHODS FOR REDUCING A TOWER'S SCATTERING CROSS-SECTION

Inspection of the limit functions contained in (13), (16), and (17) shows that reducing a structure's scattering cross-section reduces in turn the structure's distortion of a nearby antenna's directive gain pattern. In this section methods for reducing the scattering cross-section of towers are investigated. It is shown in subsection 4.1 that, provided the height of the tower is not too large, a tower's scattering cross-section can be significantly reduced by electrically isolating the base of the tower from the ground plane. The use of stubs as a means for reducing the scattering cross-section for towers is investigated in Subsections 4.2 and 4.3 where the normalized height for the towers satisfy respectively $h/\lambda \leqq .25$ and $.25 \leqq h/\lambda \leqq .50$.

4.1 Electrical Isolation of the Base of Towers from the Ground Plane

It may be possible in some cases to electrically isolate the base of a tower from the ground plane. Figure 34 shows $\sigma_\theta(90°,\phi)/\lambda^2$ as a function of h/λ for idential $a/\lambda=.001$ towers except that one of the towers is electrically connected, whereas the other is not electrically connected, to the ground plane. It is shown that disconnecting the base of the tower from the ground plane, shifts the peak for the lowest h/λ resonance from $h/\lambda=.235$ to $h/\lambda=.460$. The two curves cross over at about $h/\lambda=.350$. It has been found that, for towers where a/λ ranges between .0005 and .008, the above h/λ cross-over points range between .360 and .305. It can be said in general that electrically disconnecting the base of a tower from the ground plane will serve as an effective means for reducing the tower's scattering cross-section provided it's normalized height is near to or less than .25.

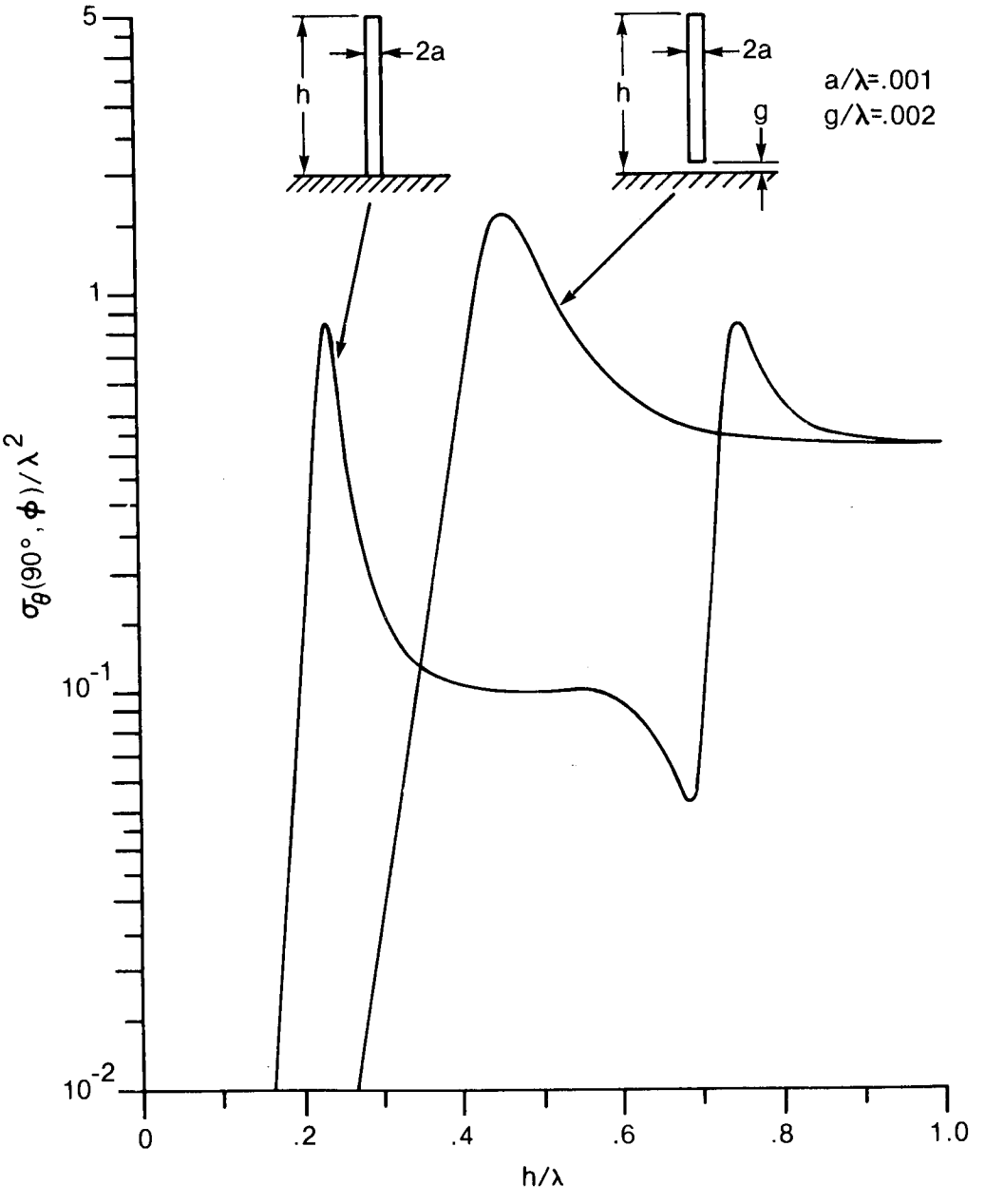

Fig. 34, A comparison of $\sigma_\theta(90°,\phi)/\lambda^2$ as a function of h/λ for two towers which are identical except that one is grounded and the other ungrounded.

4.2 Stubs on Towers where h/λ is Equal To or Less Than .25

Figure 35 shows the type of stubs which will be employed on towers where normalized heights satisfy $h/\lambda \leqq .25$. They will be referred to as full-length loaded stubs because they: 1) extend from the top of the tower (where they are electrically connected to the tower) downward to a point near the tower's base, and 2) are loaded (connected to the tower) at the bottom end by a reactance (X_L).

We first investigate the characteristics of the following full-length loaded stub systems on Fig. 35's tower where $h/\lambda=.15$.

a) A one stub system where only the stub numbered 1 in Fig. 35 is present and the normalized distance between the stub wire and adjacent tower wire (d/λ) is .001 .
b) The four stub system shown in Fig. 35 where $d/\lambda=.0015$.
c) The four stub system defined in b) above except that $d/\lambda=.0030$.

Figures 36, 37 and the appropriate columns in Table 1 provide a comparison for the characteristics of the one and four-stub systems defined above in a) and b). The figures plot normalized scattering cross-section along the ground plane ($\sigma_\theta(90°,\phi)/\lambda^2$) for the above tower-stub systems, as a function of load reactance (X_L). Both the one stub and four stub systems show the same general $\sigma_\theta(90°,\phi)/\lambda^2$ versus X_L characteristics in that, as X_L is decreased from zero, a deep null followed by a peak in $\sigma_\theta(90°,\phi)/\lambda^2$ are encountered. In the figures and Table 1, the values of X_L which produce the null and peak values for $\sigma_\theta(90°,\phi)/\lambda^2$ are symbolized by respectively X_L-(optimum) and X_L-(worst) because, for our purposes, they are the optimum and worst load reactances. The tables and figures also contain the following characteristic parameters.

$\sigma_\theta(90°,\phi)/\lambda^2$- (tower alone) = $\sigma_\theta(90°,\phi)/\lambda^2$ for the tower without stubs

$\sigma_\theta(90°,\phi)/\lambda^2$- ($X_L=\infty$) = $\sigma_\theta(90°,\phi)/\lambda^2$ for the case where $X_L=\infty$ (i.e. the stubs are not loaded)

$\sigma_\theta(90°,\phi)/\lambda^2$- (worst) = the peak value for $\sigma_\theta(90°,\phi)/\lambda^2$ as a function of X_L

$Z_i = R_i+jX_i$ = the impedance seen at the load end of a stub when all stub loads are absent.

Note that the characteristic parameter "A" in Table 1 will be defined when we consider the frequency bandwidth properties of the four stub systems. The values for $\sigma_\theta(90°,\phi)/\lambda^2$-(tower alone) is important because a stub system has a benificial effect only if it reduces the tower-stub system's $\sigma_\theta(90°,\phi)/\lambda^2$ below this value. A comparison of Figs. 36 and 37 show the width of the four stub system's null to be significantly broader than that for the one stub system. Two stub systems were found to have a null width which is intermediate to those above. It appears therefore that the bandwidth for stub systems increases as the number of stubs is increased

from one to four. It will be shown further on that the frequency bandwidth for four stub systems is marginal, hence we will consider only four stub systems in the remainder of this section.

It can be seen (refer to Fig. 37) that when X_L is made to be X_L-(optimum) then the tower-stub system's normalized scattering cross-section along the ground plane $\sigma_\theta(90°,\phi)/\lambda^2$) is much reduced below that for the tower alone. Figure 37 however, gives no information about the tower-stub systems scattering characteristics at angles above the ground plane (i.e. $\theta < 90°$) and therefore in this region the system could have unsatisfactorily high values for $\sigma_\theta(\theta,\phi)/\lambda^2$. Figure 38 contains vertical $\sigma_\theta(\theta,\phi)/\lambda^2$ patterns for the tower with no stubs and the tower stub system where X_L is X_L-(worst) and X_L-(optimum). The X_L-(optimum) vertical $\sigma_\theta(\theta,\phi)/\lambda^2$) pattern increases as θ is decreased from 90° and peaks at about θ=35°; however despite this the pattern is always much less than that for the tower with no stubs.

The incident field induces the currents on the scattering structure which in turn induce the scattered field. Therefore an investigation of the tower-stub system's induced currents would probably be instructive. For Fig. 37's structure, this is done in Figs. 39 and 40 where X_L is respectively X_L-(optimum) and X_L-(worst). The figures plot current amplitude and phase along (as a function of z, see Fig. 35) stub wire #1 and the adjacent tower wire. Also shown, for purposes of comparison is current amplitude along the above tower wire when there are no stubs on the tower. It might be thought that the optimum stub load would be that which produces an open circuit as seen at the stub's load end. This would supposedly reduce the tower-stub system's scattering cross-section by reducing the induced currents at the tower's base, and hence along its length. The information contained in Fig. 39 shows the above mode of operation to be incorrect. With the exception of the portion of the tower wire below the bottom end of the stub, the optimumly loaded stubs do not decrease, but instead increase the current amplitude on the tower wire. The system's true mode of operation becomes apparent when it is observed that when X_L=X_L-(optimum): 1) the amplitudes of the currents on the stub and adjacent tower wire are almost equal, and 2) the phases for these currents differ by about 180°. Therefore, since the separation between the stub and adjacent tower wire is small with respect to the wavelength, the currents on the two wires induce far-field intensities which nearly cancel each other. Note that the current amplitude and phase values shown in Fig. 39 (and the other current plots in this section) correspond to the following incident electric field intensity.

$E_i = \underline{u}_z(-1)\exp(jkx), v/\lambda$

$\underline{u}_z$ = the z directed unit vector

$k = 2\pi/\lambda$

When X_L is made to be X_L-(worst) the above current distributions become as shown in Fig. 40. A comparison of Figs. 39 and 40 shows that the

tower-stub system where $X_L=X_L$-(worst) has a comparatively high scattering cross-section because changing X_L to X_L-(worst): 1) increases the currents on the structure's wires, and 2) produces stub and adjacent tower wire current amplitudes which are not as close to being equal.

It is not sufficient that the tower-stub system have a significantly lower scattering cross-section than the tower alone; it is necessary in addition that the system have the above characteristic across the frequency band occupied by the transmitted signal. The scattering cross-section as a function of X_L behavior does not completely specify a tower-stub systems frequency characteristics because changing frequency, in addition to changing X_L, also changes the system's dimensions in wavelengths. In this section plots like that contained in Fig. 41 are used to show how tower-stub systems perform as a function of frequency. These figures plot $\sigma_\theta(90°,\phi)/\lambda^2$ as a function of f/f_o where f is the frequency variable and at $f=f_o$:
1) The dimensions of the system in wavelengths are those specified. For Fig. 41 these are the dimensions previously specified in b).
2) The stub load reactances (or in the following subsection, the normalized stub lengths) are made to be optimum. For Fig. 41's structure, $X_L=X_L$-(optimum)= -522 Ω.

On some of the plots showing $\sigma_\theta(90°,\phi))/\lambda^2$ as a function of f/f_o and in Tables 1 to 5, values for the parameter $A(\Delta f/f_o)$ are listed where Δf is a bandwidth (hence $\Delta f/f_o$ is a normalized bandwidth) for the transmitted signal and

$A(\Delta f/f_o)$= the minimum amount, in the normalized bandwidth $\Delta f/f_o$, that the optimumly loaded tower-stub system attenuates $\sigma_\theta(90°,\phi)/\lambda^2$ below that for the tower alone when $f=f_o$.

Values for $A(\Delta f/f_o)$ are considered for $\Delta f/f_o$ equal to .0374, .0200 and .0125. When Δf is 20 kHz, the above $\Delta f/f_o$ values correspond respectively to the f_o frequencies 535 kHz, 1000 kHz and 1605 kHz (the bottom, approximate middle and top frequencies for the AM broadcast band). For the tower-stub system specified previously in b), Fig. 41 and Table 1 show $A(\Delta f/f_o)$ to be 13.9 db, 19.2 db and 23.2 db when $\Delta f/f_o$ is respectively .0374, .0200 and .0125.

The tower stub system, for which Figs. 42 and 43 plot $\sigma_\theta(90°,\phi)/\lambda^2$ as functions of respectively X_L and f/f_o, is that specified previously in c). This system is the same as was investigated above except that the normalized distance between the centers of a stub wire and adjacent tower wire (d/λ) has been increased from .0015 to .0030. When the appropriate columns in Table 1 and Figs. 37, 41, 42 and 43 are compared, it is seen that doubling d/λ from .0015 to .0030:
1) Increased the reactances X_L-(optimum), X_L-(worst) and X_i. This is to be expected because increasing d/λ increases the characteristic impedance of the transmission line formed by the stub and tower.
2) Increased R_i because (in addition to the reason mentioned in 1) increasing d/λ makes the structure a better radiator when the feed point is at the load end for a stub.

3) Had little effect on $\sigma_\theta(90°,\phi)/\lambda^2$-(worst).
4) Slightly increased $A(\Delta f/f_o)$.

From an electrical performance point of view the $d/\lambda=.0030$ system's larger values for $A(\Delta f/f_o)$ make it superior to the $d/\lambda=.0015$ system. This increase in $A(\Delta f/f_o)$ was however small (about 1.5db) and therefore (because they would be easier to contruct) we will in the remainder of this section consider only stub systems where $d/\lambda=.0015$.

To this point in the subsection we have considerd tower-stub systems where $h/\lambda=.15$. Table 2 lists values for Z_i, X_L-(optimum) and A(.02) for Fig. 36's tower-stub system where $d/\lambda=.0015$ and h/λ ranges between .050 and .250. The A(.02) values of Table 2 show that, for $h \leqq .250$ towers, the full length loaded stub systems perform best when h/λ is in the vicinity of .250. When Table 2's values for Z_i and X_L-(optimum) are compared it is seen that (except when $h/\lambda \simeq .250$) $-X_i$ is approximately equal to X_L-(optimum). However, note that as indicated in Figs. 36, 37 and 42, X_L should not in general be set equal to $-X_i$. The above, and the narrowness of the nulls in the $\sigma_\theta(90°,\phi)/\lambda^2$ as a function of X_L curves, indicate the following procedure for setting up full length loaded stub systems.

1) Install at least four stubs
2) Measure the input reactances (X_i) for a stub.
3) Load the stubs with variable reactances for which the center reactance is approximately $-X_i$.
4) Place a field strength meter in the far-field of the array-scatterer combination and adjust the stub load reactances to reduce to a minimum the tower-stub system's perturbation of the measured field.

Although it has not been tried, it would probably suffice in step 3) to connect the load ends of all stubs together and place a variable reactance, whose center reactance was about $-X_i/n_s$ (where n_s is the number of stubs), between the connected stubs and ground. If the antenna's directive gain pattern has a null in some directon along the ground plane, it would be best to place step 4)'s field strength meter in the direction of the null.

Table 1, Characteristic values for three different full-length loaded stub systems on the tower shown in Fig. 35 where $h/\lambda=.150$.

	One stub $d/\lambda=.0015$	Four stubs $d/\lambda=.0015$	Four stubs $d/\lambda=.0030$
$\sigma_\theta(90°,\phi)/\lambda^2$ - (tower alone)	.00912	.00912	.00912
$\sigma_\theta(90°,\phi)/\lambda^2$ - ($X_L=\infty$)	.0119	.0228	.0387
$\sigma_\theta(90°,\phi)/\lambda^2$ - (worst)	.760	.774	.769
X_L -(optimum) in ohms	-437	-522	-684
X_L -(worst) in ohms	-488	-760	-1220
R_i - in ohms	6.2	10.1	28.9
X_i - in ohms	487.1	498.4	655.6
R_i - in ohms	6.2	10.1	28.9
X_i - in ohms	487.1	498.4	655.6
$A(\Delta f/f_o)=A(.0374)$ in db	-	13.9	15.5
A(.0200) in db	-	19.2	20.7
A(.0125) in db	-	23.2	24.5

Table 2, Z_i, X_L-(optimum) and $A(\Delta f/f_o=.02)$ for Fig. 35's tower with full-length loaded stubs, as a function of $h/\lambda(.050 \leqq h/\lambda \leqq .250)$, where $d/\lambda=.0015$.

h/λ	Z_i (Ω)	X_L-(optimum) (Ω)	A(.02) (db)
.050	.013+j(102.5)	-114.7	12.4
.100	.33+j(238.8)	-267.2	17.3
.150	10.1+j(498.4)	-522.0	19.2
.200	438.8+j(1328)	-1135.5	30.0
.250	1940+j(1634)	∞ *	26.0

* When searching for B_L-(optimum), where B_L-(optimum)= $-1/[X_L$-(optimum)], it was found that, for the case where $h/\lambda=.250$, B_L-(optimum) was very close to zero. Therefore, for the purpose of computing A, X_L (at $f/f_o=1$) was set equal to ∞. That ∞ was not quite the proper value for X_L-(optimum) was shown in a plot of $\sigma_\theta(90°,\phi)\lambda^2$ versus f/f_o where the minimum in $\sigma_\theta(90°,\phi)/\lambda^2$ occured at $f/f_o=1.003$. If X_L-optimum was ∞ then the above minimum would have occured at $f/f_o=1$.

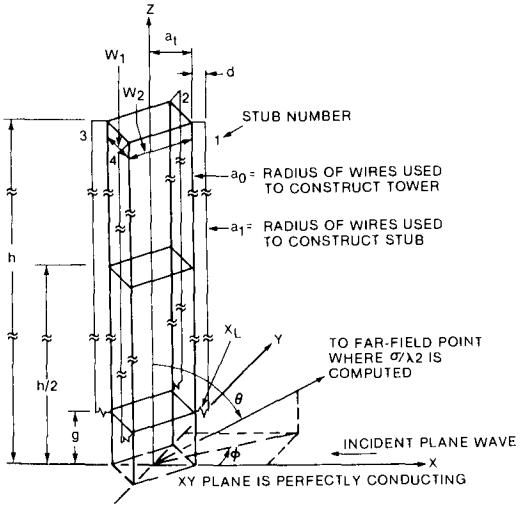

Fig. 35, Geometry of a tower with 4 full-length loaded stubs where $w_1/\lambda=\omega_2/\lambda=.005657$, $(a_t/\lambda=.004)$, $a_o/\lambda=.00015$, $a_1/\lambda=.000015$ and $g/\lambda=.005$.

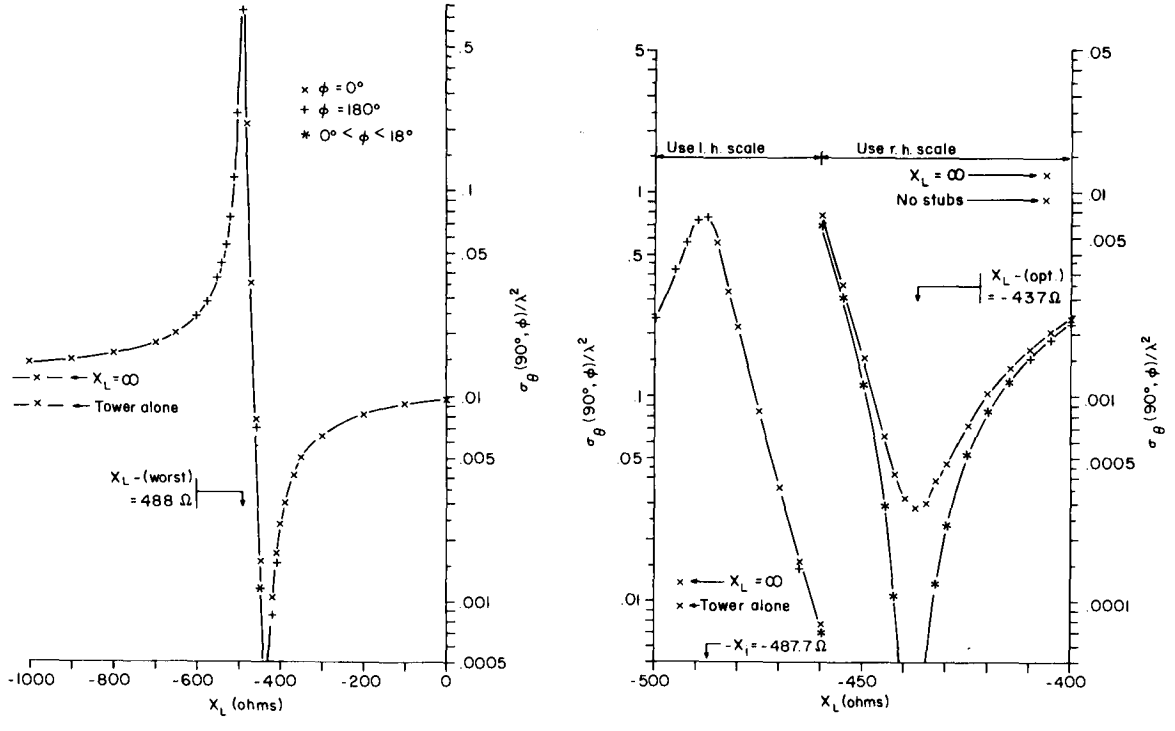

Fig. 36, $\sigma_\theta(90°,\phi)/\lambda^2$ as a function of X_L for the tower shown in Fig. 35 where $h/\lambda=.15$, $d/\lambda=.0015$ and 1 full-length stub (stub 1) is used.

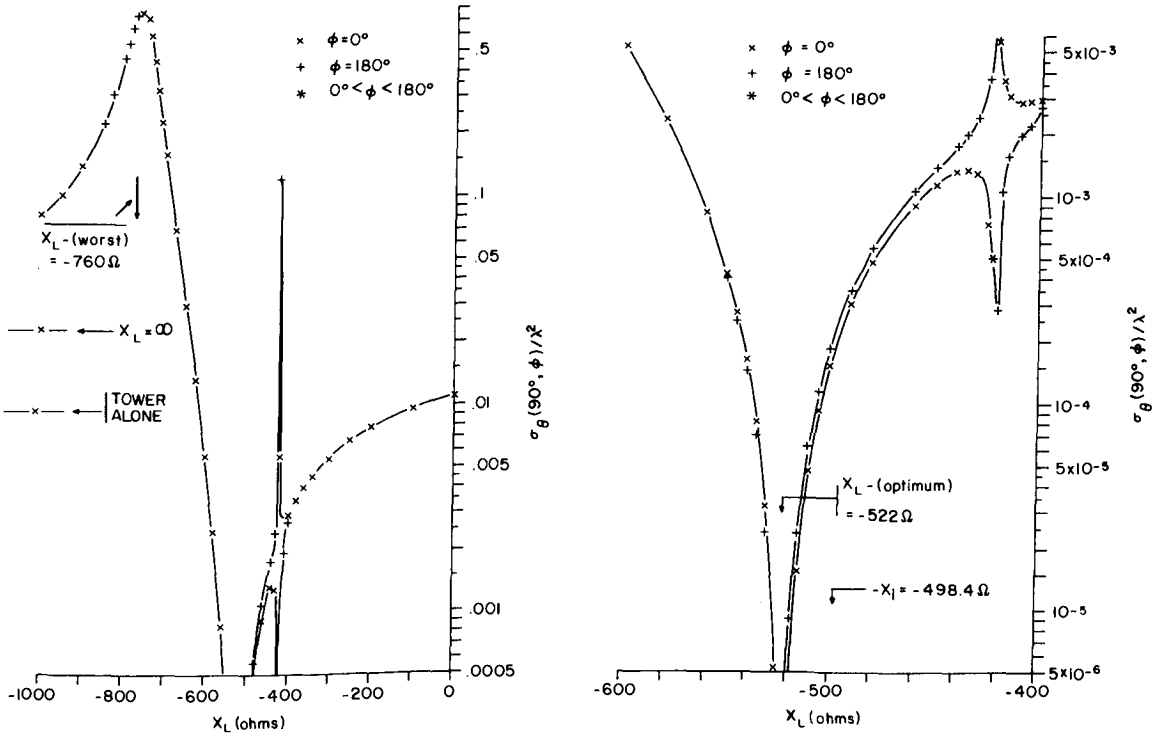

Fig. 37, $\sigma_\theta(90°,\phi)/\lambda^2$ as a function of X_L for the tower shown in Fig. 35 where h/λ=.15, d/λ=.0015 and 4 full-length stubs are used.

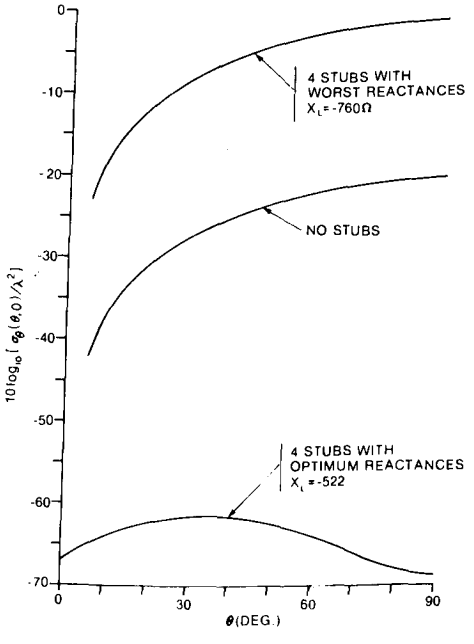

Fig. 38, Vertical σ_θ/λ^2 patterns for Fig. 37's structure where there are:
a) 4 stubs with worst reactances,
b) no stubs and c) 4 stubs with optimum reactances.

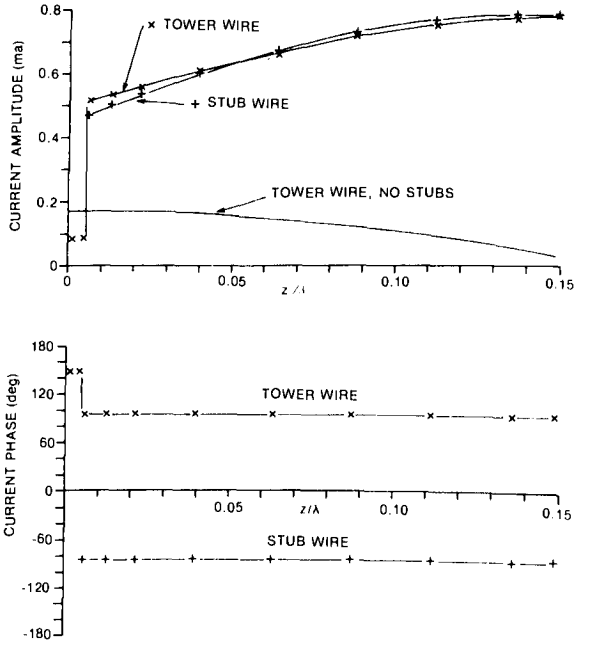

Fig. 39, The amplitude and phase of current on stub 1 and adjacent tower wire for Fig. 37's structure where the load reactances are optimum (X_L=-522 Ω).

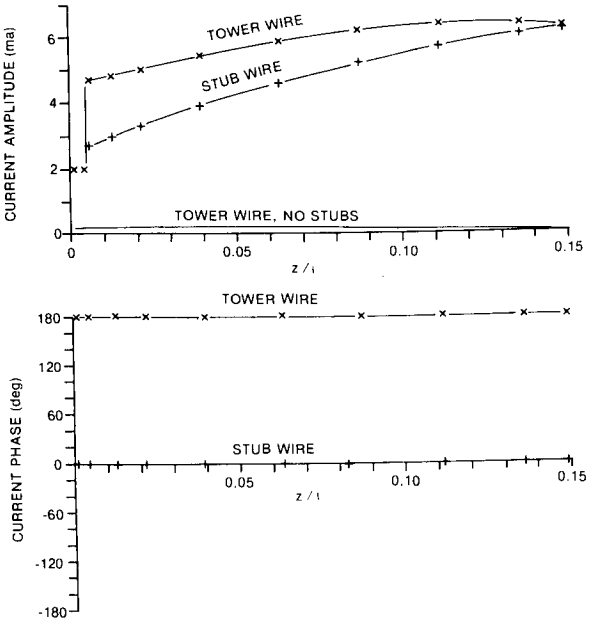

Fig. 40, The same as Fig. 39 except that the stub load reactances are worst (X_L=-760 Ω).

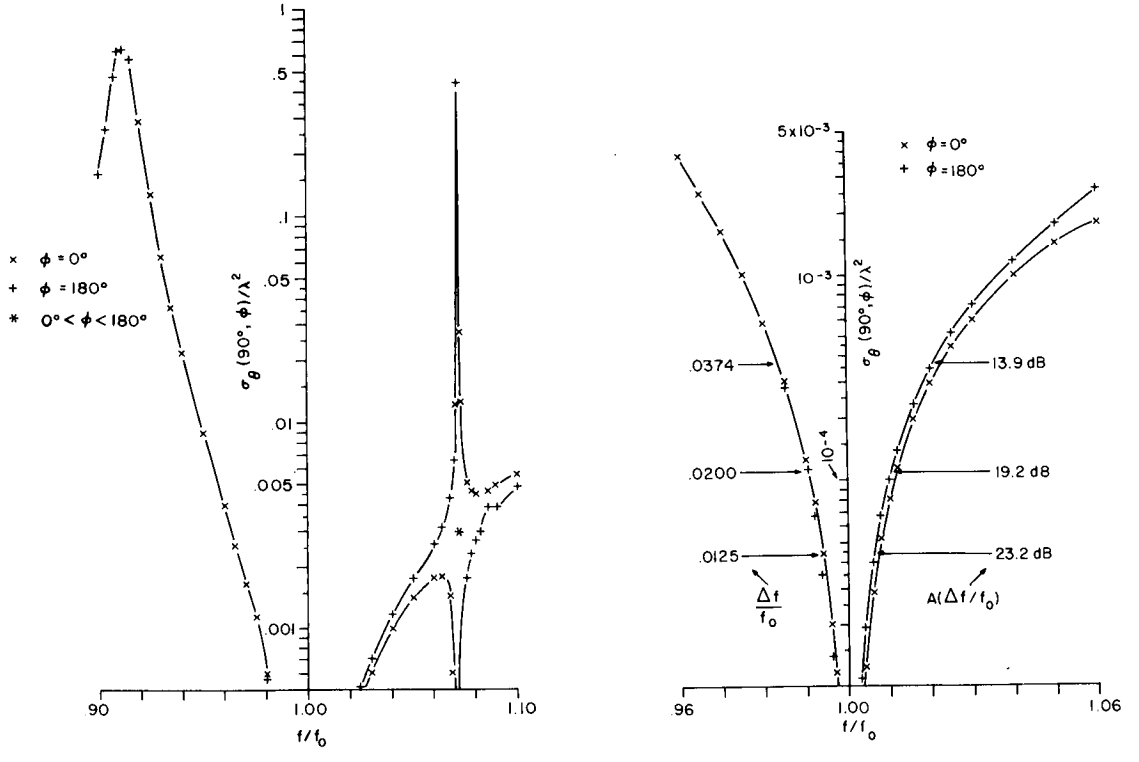

Fig. 41, $\sigma_\theta(90°,\phi)/\lambda^2$ as a function of normalized frequency (f/f_o) where at $f=f_o$: a) the structure's dimensions in wavelengths are the same as those for Fig. 37 and b) the load reactances are optimum (X_L=-522 Ω).

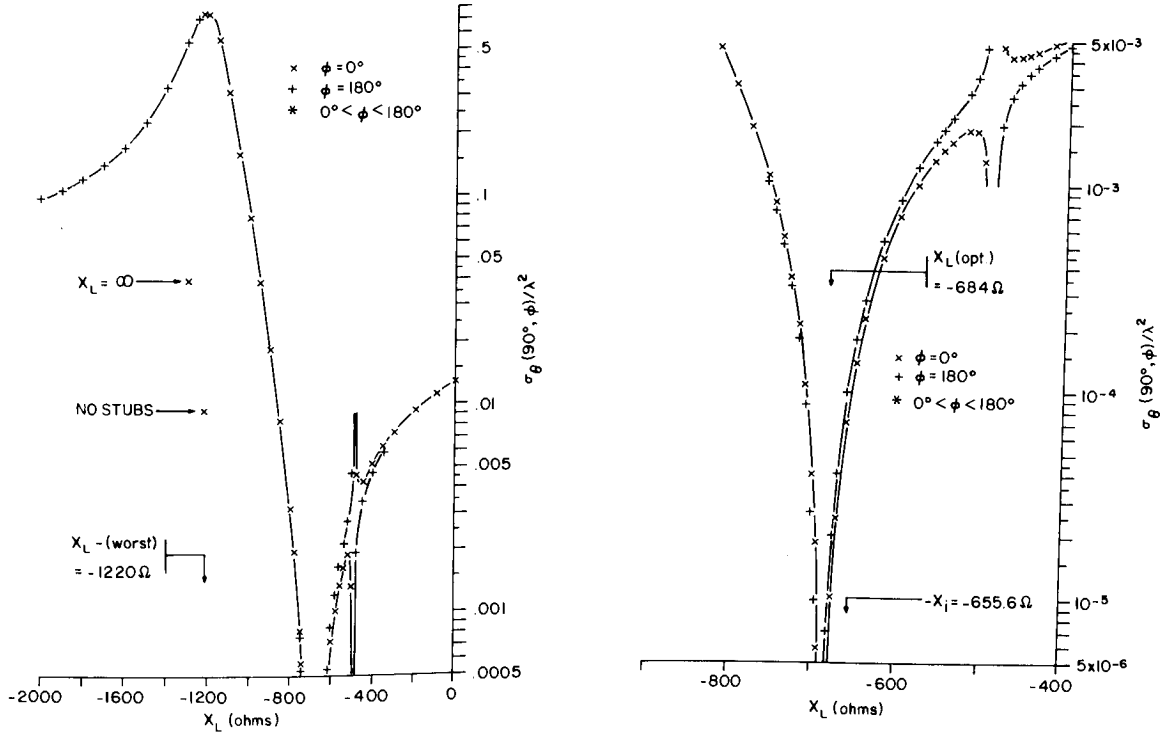

Fig. 42, $\sigma_\theta(90°,\phi)/\lambda^2$ as a function of X_L for the same structure as was used to compute Fig. 37 except that $d/\lambda=.003$.

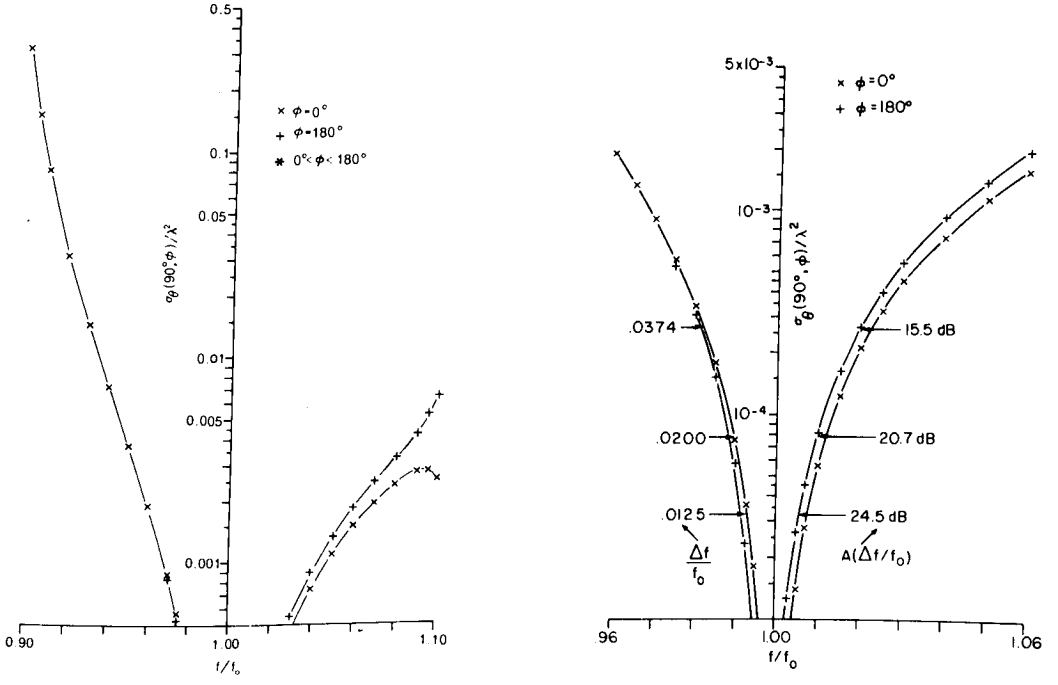

Fig. 43, $\sigma_\theta(90°,\phi)/\lambda^2$ as a function of normalized frequency where at $f=f_o$: a) the structure's dimensions in wavelengths are the same as those for Fig. 42 and b) the load reactances are optimum (X_L=-684 Ω).

4.3 Stubs on Towers where h/λ is between .25 and .50

In this subsection we investigate and compare the characteristics of the following types of stub systems on towers whose normalized heights (h/λ) range between .25 and .50.
a) Last subsection's four full-length loaded stub sytem (see Fig. 35).
b) The four short stub system shown in Fig. 44

The short stubs are about $.25\lambda$ long where their bottom ends (which are near the tower's base) and top ends are respectively electrically, not connected, and connected, to the tower. They can only be used on towers which are higher than about $.25\lambda$ and are called short stubs because they are usually shorter than the tower is high.

Figures 45 to 49 and 50 to 54 plot characteristics for respectively the tower-stub systems defined in a) and b). Table 3 lists characteristic values for both of the above systems. The types of plots presented are the same as appeared in the previous subsection except that for the short stubs, s/λ (where s is the length of the stub) replaces X_L as the parameter which is varied to optimize the system.

The curves showing $\sigma_\theta(90°,\phi)/\lambda^2$ as a function of X_L or s/λ in Figs. 45 and 50 are similar to those present in the previous subsection in that their is an optimum X_L or s/λ and, not far removed, a worst X_L or s/λ. A difference between the full-length loaded stub systems investigated in this and the previous subsection is that X_L-(optimum) is respectively positive (inductive) and negative (capacitive).

The vertical patterns in Figs. 46 and 51, for the cases where respectively X_L and s/λ are optimum, are much alike. The amplitude of the above-the-ground-plane lobes for the above vertical patterns can be seen to be much greater than that shown in Fig. 38 for the optimum full-length loaded stubs on the $h/\lambda=.150$ tower.

The current amplitude and phase versus z/λ plots in Figs. 47, 48, 52, and 53 show that the mode of operation for the $h/\lambda=.400$ tower-stub systems is essentially the same as that previously described for the $h/\lambda=.150$ tower-stub system. However, for the $h/\lambda=.400$ systems, the stub and adjacent tower wire current amplitudes are not as close to being equal as they were for the $h/\lambda=.150$ system. Therefore, for the purpose of reducing σ_θ/λ^2 along the ground plane, the optimum $h/\lambda=.400$ systems must rely more on the cancellation of far-fields induced by non-adjacent currents. This explains the $h/\lambda=.400$ systems' larger vertical σ_θ/λ^2 pattern lobes above the ground plane because non-adjacent, as compared to adjacent, wire currents cannot (due to their larger separation) as successfully induce far-fields which cancel over a range of θ angles. A comparison of $A(\Delta f/f_o)$ for the full-length and short $h/\lambda=.400$ tower-stub systems in Table 3 and respectively Figs. 49 and 54, shows that the short stub system has superior frequency bandwidth characteristics.

To this point in the subsection we have considered the properties of short and full-length loaded stub systems on an $h/\lambda=.400$ tower. Tables

4 and 5 list characteristics for the above types of stubs on towers where h/λ ranges between .250 and .500. A comparison of the full-length loaded stub system's X_i and X_L-(optimum) values contained in Table 4 shows that (as was the case where $h/\lambda < .250$) X_L-(optimum) is approximately equal to $-X_i$ (except where h/λ is near .250). The short stub system's optimum lengths in Table 5 are slightly less than $\lambda/4$ and note that they become shorter as h/λ is increased. When the A(.02) values in Tables 4 and 5 are compared it is seen that the short stub systems perform better than do the full-length loaded stub systems. This is particularly true when h/λ is larger than about .350. Note that for some value of h/λ near .250 the short and full-length loaded stub systems become one and the same system.

Table 3, Characteristic values for the full-length and short stub systems shown in Figs. 35 and 44 where $h/\lambda=.400$ and $d/\lambda=.0015$

	Four full-length stubs	Four short stubs
$\sigma_\theta(90°,\phi)/\lambda^2$ - (tower alone)	.145	.145
$\sigma_\theta(90°,\phi)/\lambda^2$ - ($X_L=\infty$)	.195	-
$\sigma_\theta(90°,\phi)/\lambda^2$ - (worst)	1.04	1.28
X_L-(optimum) in ohms	291.1	-
X_L-(worst) in ohms	324	-
s/λ-(optimum)	-	.2356
s/λ-(worst)	-	.256
R_i in ohms	3.3	-
X_i in ohms	-251.8	-
$A(\Delta f/f_o)=A(.0374)$ in db	3.1	11.4
A(.0200) in db	5.7	16.4
A(.0125) in db	8.5	20.3

Table 4, Z_i, X_L-(optimum) and $A(\Delta f/f_o=.02)$ for Fig. 35's tower and full-length loaded stubs, as a function of $h/\lambda(.250 \leqq h/\lambda \leqq .450)$, where $d/\lambda=.0015$.

h/λ	Z_i (Ω)	X_L-(optimum) (Ω)	A(.02) (db)
.250	1940+j(1634)	∞ *	26.0
.300	119.1+j(-1199.4)	1196.6	19.5
.350	10.5+j(-479.4)	542.6	17.4
.400	3.26+j(-251.8)	291.1	5.7
.450	.39+j(-111.2)	135.6	1.2

* See Table 2

Table 5, s/λ-(optimum) and $A(\Delta f/f_o=.02)$ for Fig. 44's tower and short stubs, as a function of $h/\lambda(.250 \leqq h/\lambda \leqq .500)$.

h/λ	s/λ-(optimum)	A(.02) db
.250	.2450*	26.0
.300	.2413	21.6
.350	.2386	18.4
.400	.2356	16.4
.450	.2320	15.0
.500	.2274	14.1

* This is the same tower stub structure as is shown in Table 2 where $h/\lambda=.250$. Hence $s/\lambda = h/\lambda - g/\lambda = .2450$ is not quite the optimum stub length.

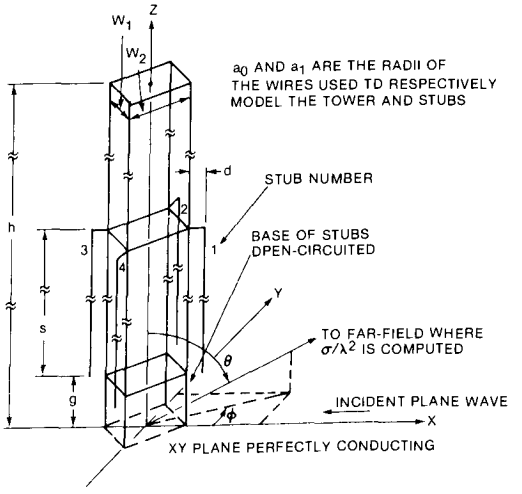

Fig. 44, Geometry of a tower with 4 short ($s/\lambda \simeq .25$) stubs where $d/\lambda = .0015$. The remaining dimensions are either as shown in Fig. 35 or specified in the text.

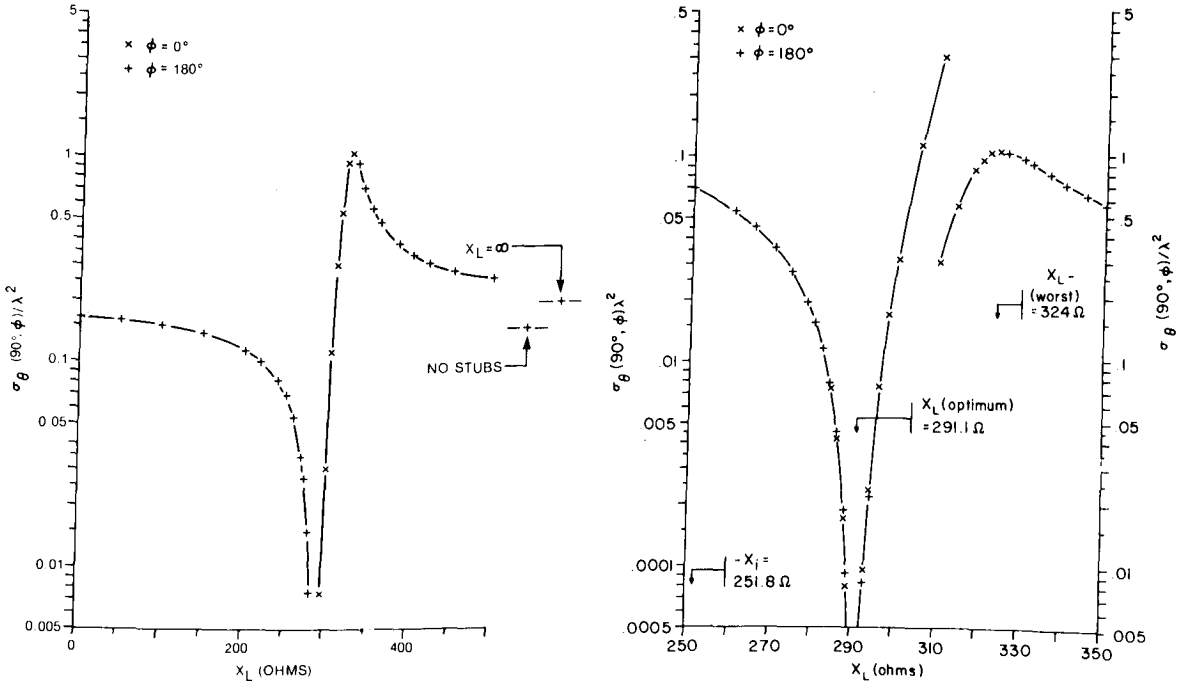

Fig. 45, $\sigma_\theta(90°,\phi)/\lambda^2$ as a function of X_L for the tower shown in Fig. 35 where $h/\lambda = .4$, $d/\lambda = .0015$ and 4 full-length stubs are used.

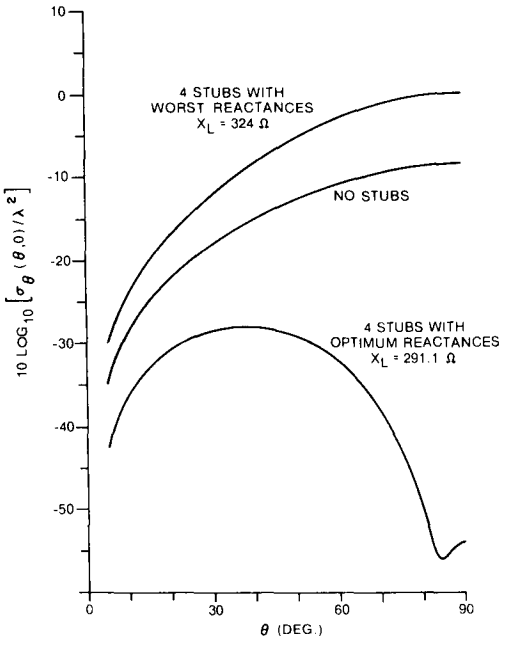

Fig. 46, Vertical σ_θ/λ^2 patterns for Fig. 45's structure where there are: a) 4 stubs with worst reactances, b) no stubs and c) 4 stubs with optimum reactances.

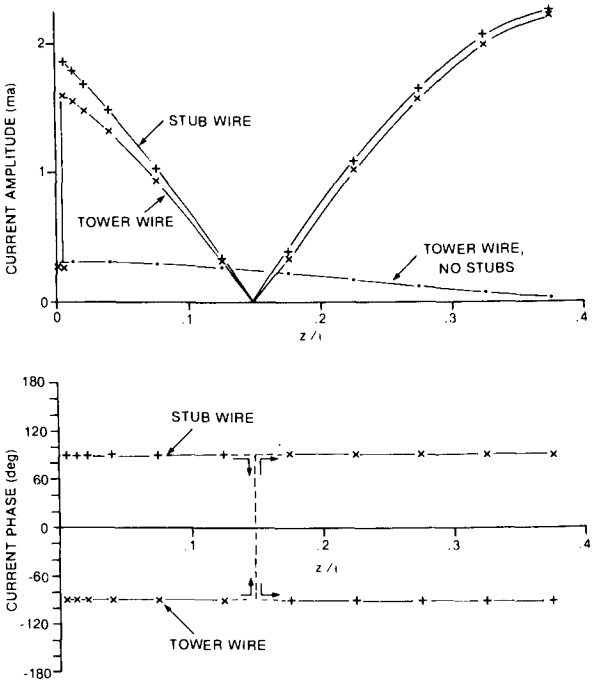

Fig. 47, The amplitude and phase of current on stub 1 and adjacent tower wire for Fig. 45's structure where the load reactances are optimum (X_L=291.1Ω).

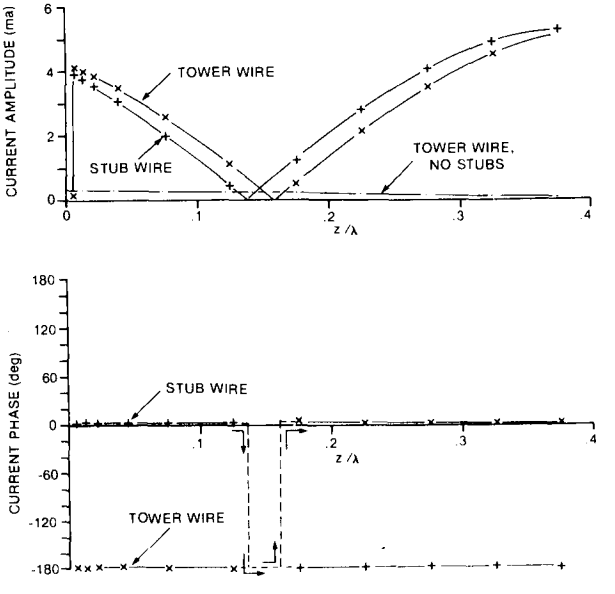

Fig. 48, The same as Fig. 47 except that the load reactances are worst (X_L=324Ω).

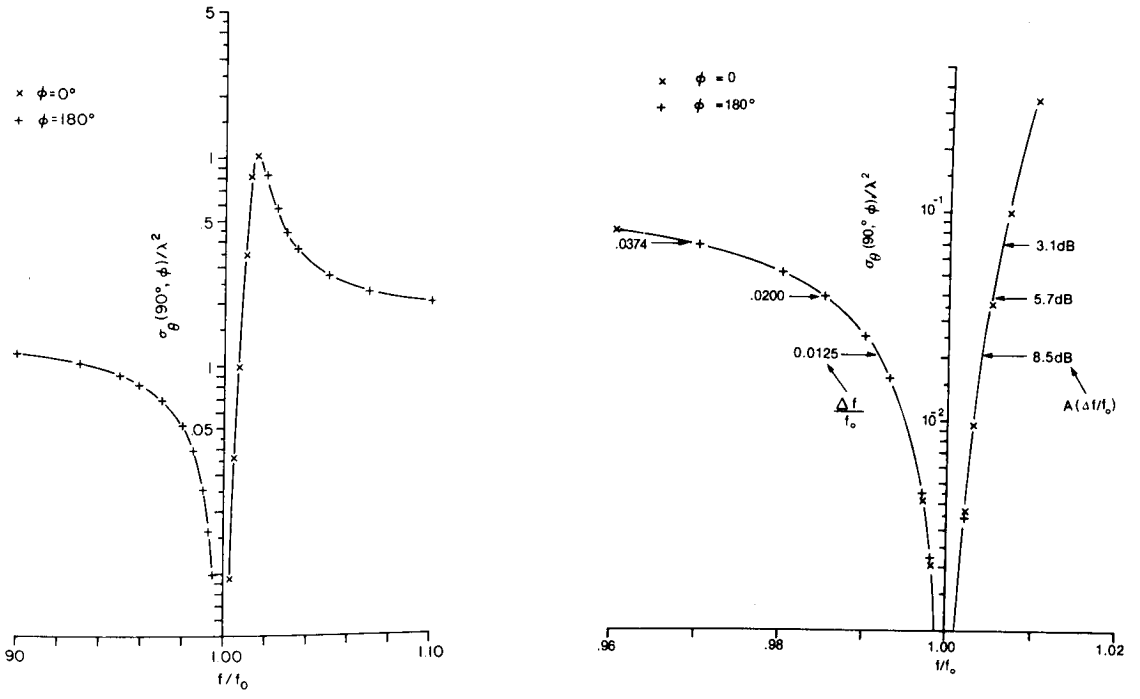

Fig. 49, $\sigma_\theta(90°,\phi)/\lambda^2$ as a function of normalized frequency where at $f=f_o$: a) the structure's dimensions in wavelengths are the same as those for Fig. 45 and b) the load reactances are optimum ($X_L=-291.1\Omega$).

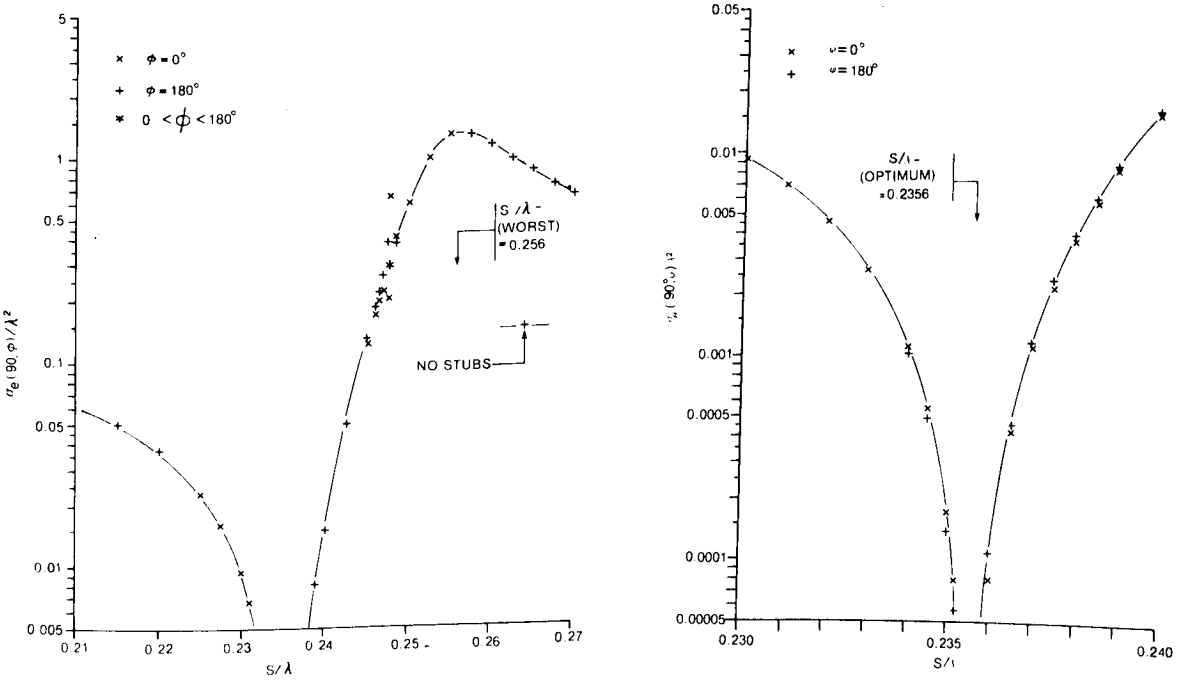

Fig. 50, $\sigma_\theta(90°,\phi)/\lambda^2$ as a function of normalized stub length (s/λ) for the tower with 4 short stubs shown in Fig. 44 where $h/\lambda=.400$.

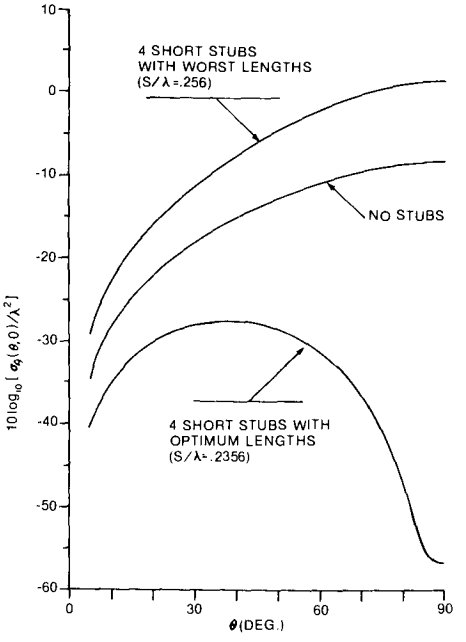

Fig. 51, Vertical $\sigma_\theta(\theta,0)/\lambda^2$ patterns for Fig. 50's structure where there are: a) four short stubs with worst lengths, b) no stubs and c) four short stubs with optimum lengths.

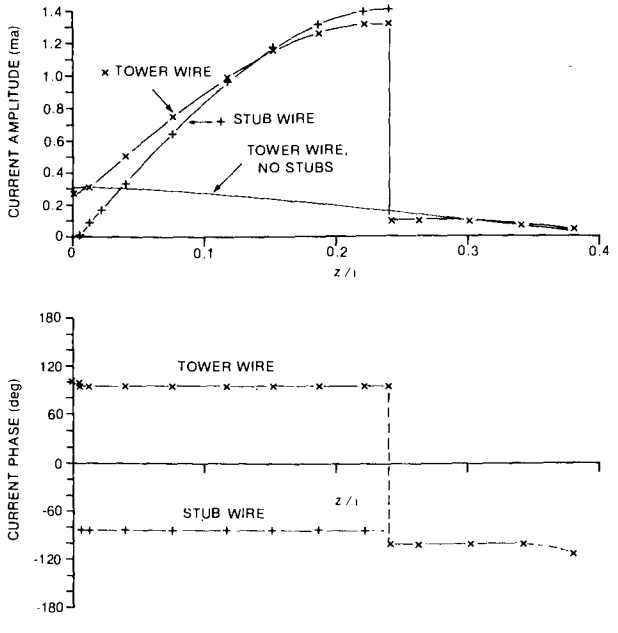

Fig. 52, The amplitude and phase of current on stub 1 and adjacent tower wire for Fig. 50's structure where the stub lengths are optimum (s/λ=.2356).

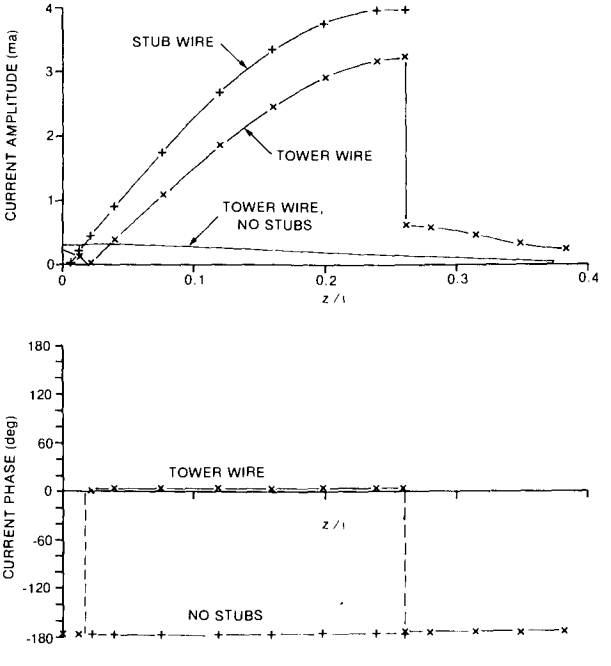

Fig. 53, The same as Fig. 52 except that the stub lengths are worst (s/λ=.256).

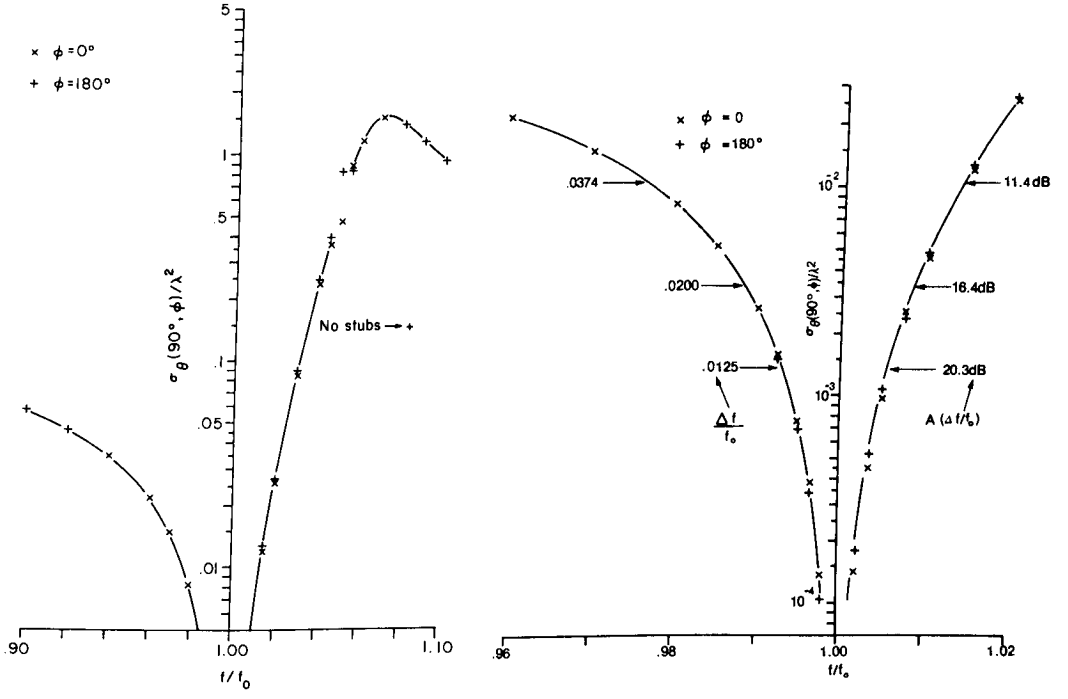

Fig. 54, $\sigma_\theta(90°,\phi)/\lambda^2$ as a function of normalized frequency where at $f=f_o$: a) the structure's dimensions in wavelengths are the same as those for Fig. 50 and b) the stub lengths are optimum ($s/\lambda=.2356$).

5. THE MINIMUM ANTENNA TO SCATTERER RANGE FOR WHICH THE NEAR-FIELD AND FAR-FIELD LIMIT FUNCTIONS ARE ACCURATE

It was pointed out in Section 2 that: 1) both the far-field and near-field limit functions will become inaccurate if the range (r_s) between the antenna and the scatterer is too small, and 2) the near-field, when compared to the far-field, limit functions will however be accurate down to smaller values of r_s. In this section directive gain and limit function patterns, for an antenna in the presence of a scatterer, are compared for the purpose of determining rules of thumb which can be used to approximate the minimum values of r_s for which the limit functions will be accurate.

The computer program NEC was used to compute: 1) this section's directive gain patterns for an antenna in the presence of a scatterer ($D_\theta(\theta,\phi)$), and 2) the limit function variables (see (13) and (16) in Section 2), $D_{a\theta}(\theta,\phi)$, $\sigma_\theta(\theta,\phi)$, $D_{\theta k}(\theta_k)$, R_k and P_t. The AM broadcast antennas which we will employ for the purposes of our calculations will be either CHFA (Edmonton)'s array or an element from CHFA's array. Figure A-1 in the appendix contains the above array's dimensions and electrical specifications. Refer to Figs. 55 and 56 for respectively the array element's vertical directive gain pattern ($D_{\theta k}(\theta_k)$) and the array's directive gain pattern along the ground plane ($D_{a\theta}(90°,\phi)$) where, for both patterns, there is no scatterer present. An isolated element from CHFA's array was computed to have a radiation resistance equal to 20.2146 ohms. The scatterer will be either an $h/\lambda(h)=.150(66.13m)$ or $h/\lambda(h)=.230(101.40m)$ tower, with $a/\lambda=.004(1.764m)$, where h and "a" are respectively the tower's height and radius. Figure 57 contains normalized vertical cross-section patterns ($\sigma_\theta(\theta,\phi)/\lambda^2$ as a function of θ) for the above towers.

For the cases where the source is a single monopole or an element of an array, we will be comparing the monopole to scatterer range (r_s) with the range r_n, where

$$r_n = \frac{2(2h+2h_a)^2}{\lambda} \qquad \ldots(18)$$

h = the height of the scatterer

h_a = the height of the monopole or array element

Note that those who measure antenna patterns commonly use the function $2D^2/\lambda$ (where D is the maximum dimension of the antenna) to compute the minimum allowable distance between the antenna and the measurement point. The range r_n as given by eqn. (18) is closely related to that given by the above function except that in eqn. (18) we have included the effects of: 1) the height (maximum dimension) of the scatterer, and 2) the ground plane through the use of 2h and $2h_a$ (as distinguished from the use of h and h_a). The height of one of CHFA's monopole elements ($h_a/\lambda(h_a)$) is .20049(88.392m). Therefore, for the cases where the tower height ($h/\lambda(h)$) is .150(66.13m) and .230(101.4m), eqn. (18) gives $r_n/\lambda(r_n)$ as respectively .9827(433.3m) and 1.483(653.6m).

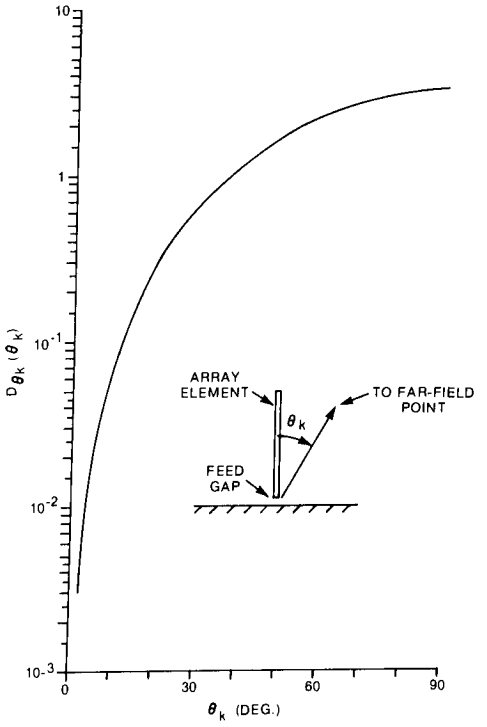

Fig. 55, The vertical directive gain pattern for an element of CHFA's array when isolated from the other elements of the array.

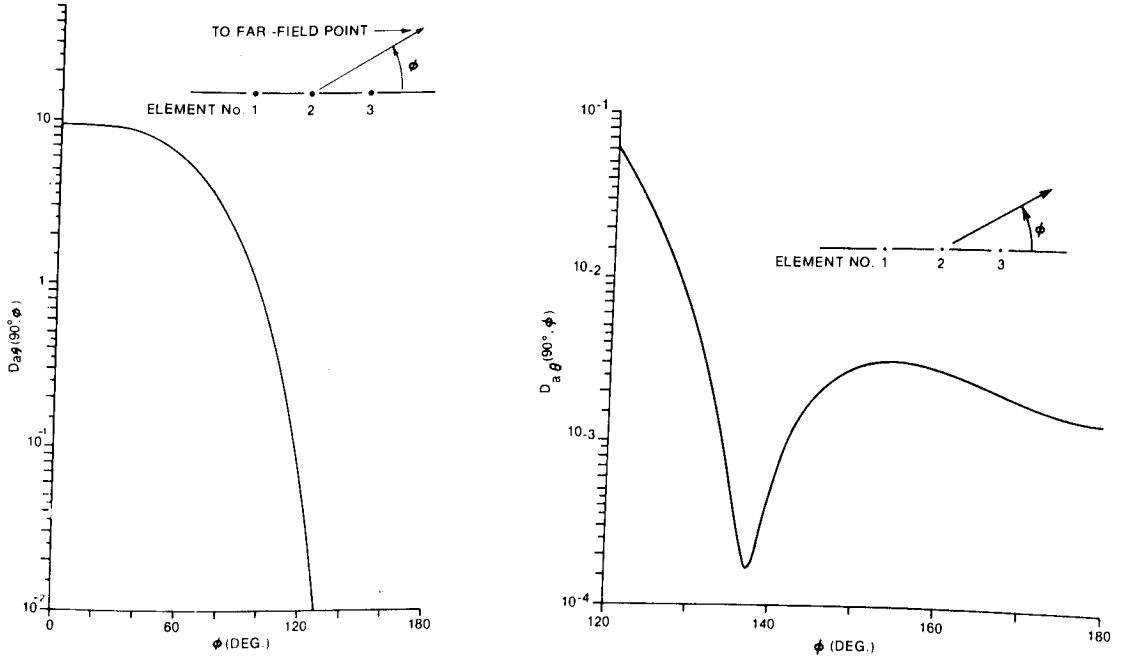

Fig. 56, The directive gain, along the ground plane, for CHFA's array.

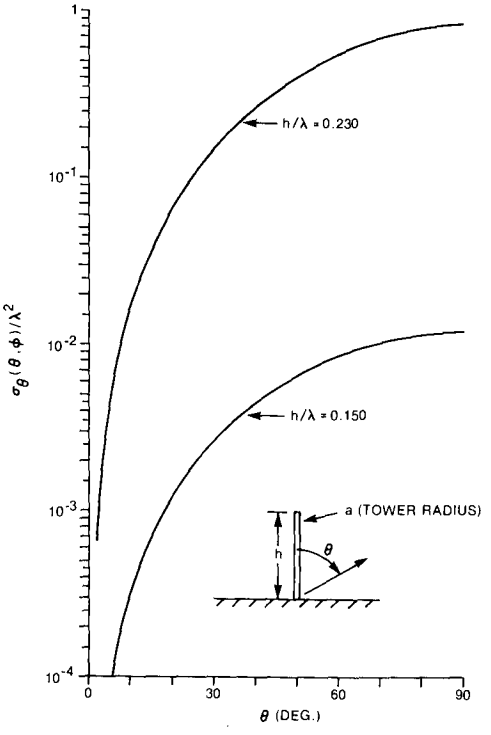

Fig. 57, Vertical scattering cross-section patterns for towers where h/λ=.230 and .150, a/λ=.004

5.1 The Minimum r_s for which the Limit Functions are Accurate when the Antenna is a Single Monopole

In this subsection the antenna will be a single monopole. For this case the far-field and near-field limit functions in (16) and (13) are identical; hence there is no need to distinguish between them and they will be simply referred to as limit functions.

When the monopole antenna is one of CHFA's array elements, Figs. 58 and 59 compare directive gain and limit function patterns for respectively the cases where:

1) the scatterer is Fig. 57's $h/\lambda(h)=.230(101.4m)$ tower and r_s is $r_n/2$, r_n and $2r_n$.
2) the scatterer is Fig. 57's $h/\lambda(h)=.150(66.13m)$ tower and r_s is $r_n/2$ and r_n.

As would be expected, the limit functions give better approximations to true limits as r_s is increased. In addition it appears that, for the case where the antenna is a monopole, the limit functions give good approximations to true limit functions provided r_s satisfies $r_s \geq r_n$.

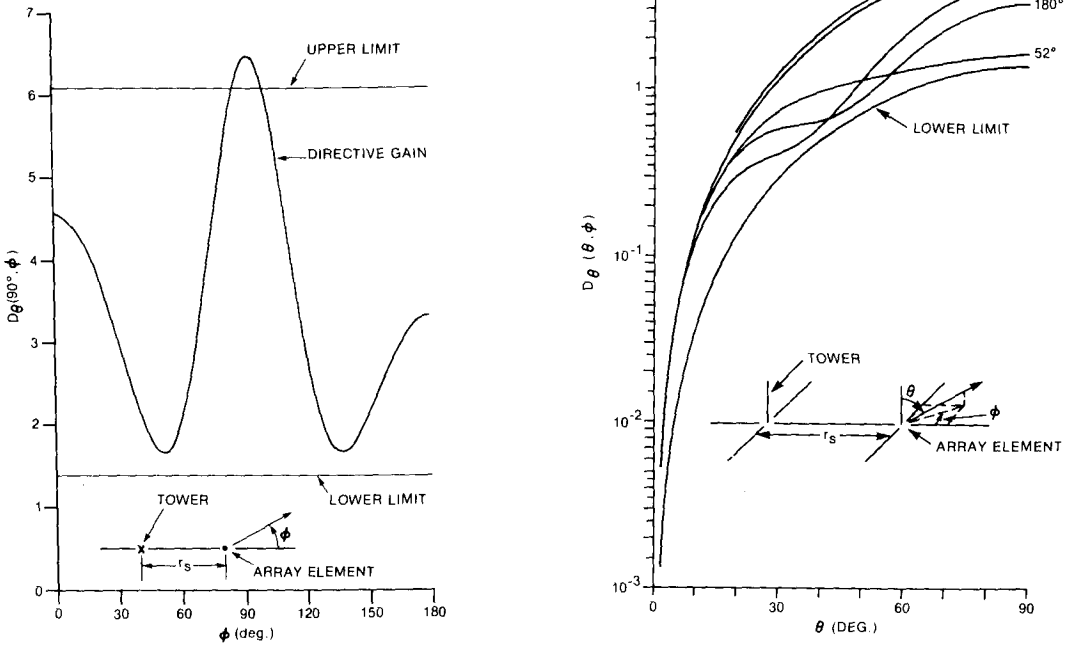

(a) $r_s=r_n/2$

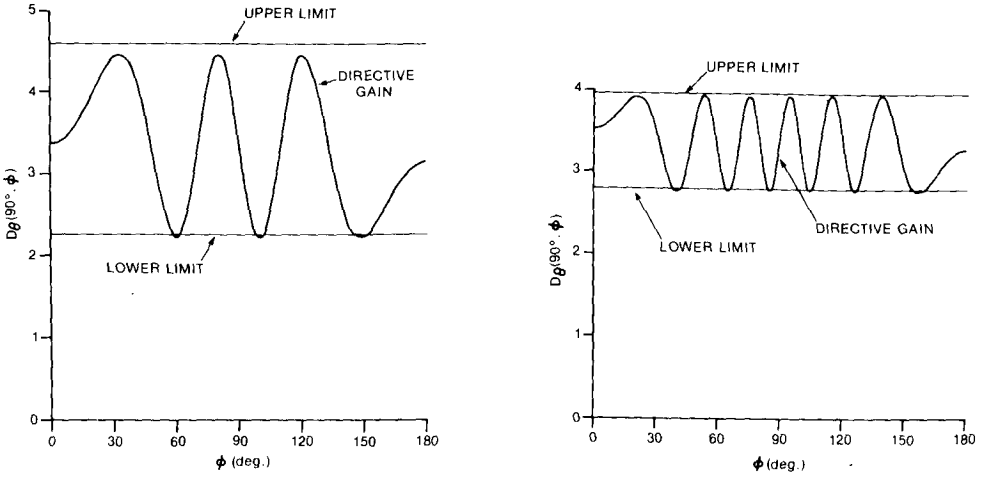

(b) $r_s=r_n$

(c) $r_s=2r_n$

Fig. 58, Directive gain and limit function patterns for an element of CHFA's array in the presence of Fig. 57's $h/\lambda(h)$=.230(101.4m) tower for (a) $r_s=r_n/2$, (b) $r_s=r_n$ and (c) $r_s=2r_n$; where $r_n/\lambda(r_n)$=1.483(653.6m).

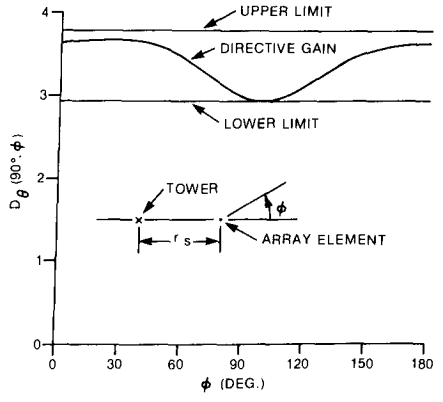

(a) $r_s = r_n/2$

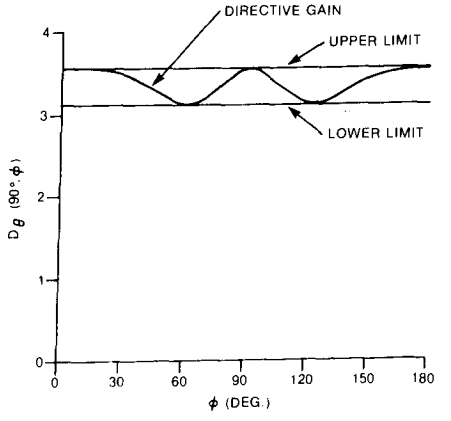

(b) $r_s = r_n$

Fig. 59, Directive gain and limit function patterns, along the ground plane, for an element of CHFA's array in the presence of Fig. 57's $h/\lambda(h)=.150(66.13m)$ tower where (a) $r_s=r_n/2$, (b) $r_s=r_n/2$ and $r_n/\lambda(r_n)=.9827(433.3m)$.

5.2 The Minimum r_s for which the Far-Field Limit Functions are Accurate when the Antenna is an Array

Figures 60 to 62 compare directive gain and far-field limit function patterns for CHFA's array in the presence of Fig. 57's $h/\lambda(h)=.230(101.4m)$ tower. In Figs. 60 to 62 the scattering tower is located respectively: 1) in the array's main beam, 2) broadside to the array, and 3) in the array's null direction. The sub-figures in the above figures correspond to different values for r_s. Note that when computing the directive gain patterns for the array-scatterer combination, the array's feed current ratios were made to be those specified, in the appendix's Fig. A-1, for the array alone. Therefore electrical interaction between the scatterer and the array made it necessary to compute new feed voltages (in the manner shown in the appendix) for each new position of the scatterer.

The figures show that when the scatterer is located, in the direction of the array's main beam (off the end of array element #3), or broadside to the array, then the far-field limit functions give good approximations to true limits for $r_s/\lambda(r_s)$ as small as .6804(300m). When however, the scatterer is located in the direction of the null for the array's pattern, then the limit functions are significantly in error, particularly when $r_s\lambda(r)$ is .6804(300m) and 1.134(500m). For these cases, it appears that the $F_\theta(\theta,\phi)$ function is (16)'s limit functions are too small.

The above are the results which would be expected when Figs. A-2 and A-3 in the appendix are examined. The figures show that: 1) when ϕ is 0° and 90°, the field patterns for the cases where $r \geqq 300m$ are close to the $r=\infty$ pattern, however 2) when $\phi=180°$ (the direction for the patterns null) r must be several thousand meters before the field patterns approach the $r=\infty$ pattern. In addition, in the vicinity of $\phi=180°$, the $r=\infty$ pattern is less than those where $r<\infty$. The $r=\infty$ pattern is that which would be computed using $D_{a\theta}(90°,\phi)$ and therefore $D_{a\theta}(90°,180°)$ in eqn. (16)'s $F_\theta(\theta,\phi)$ functions, and hence the $F_\theta(\theta,\phi)$ functions themselves, will be (as noted above) too small.

In general, when the antenna is an array, the far-field limit functions should only be used when, at the range and in the direction of the scatterer, the array's field pattern (of the type shown in Figs. A-2 and A-3) is sufficiently close to the $r=\infty$ pattern.

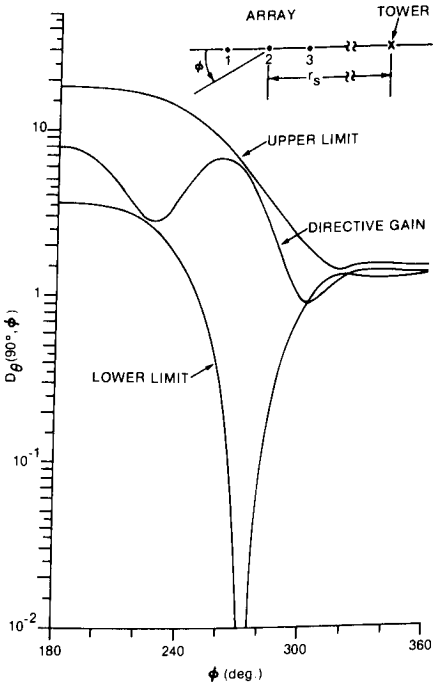

(a) $r_s/\lambda(r_s)$=.6804(300m)

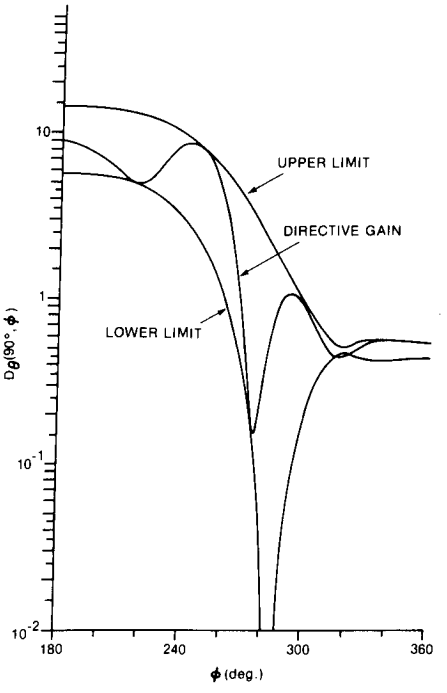

(b) $r_s/\lambda(r_s)$=1.134(500m)

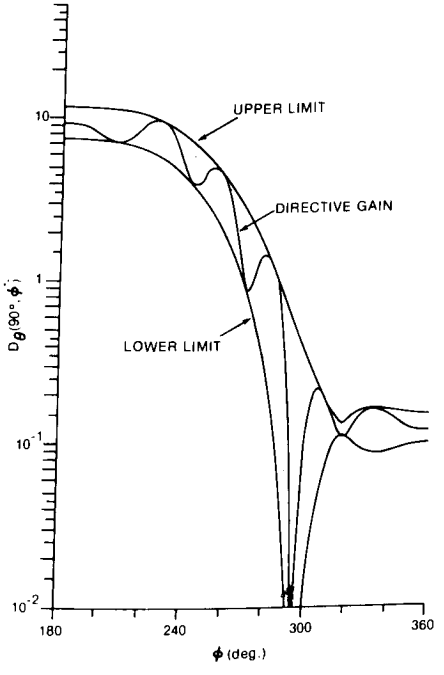

(c) $r_s/\lambda(r_s)$=2.268(1000m)

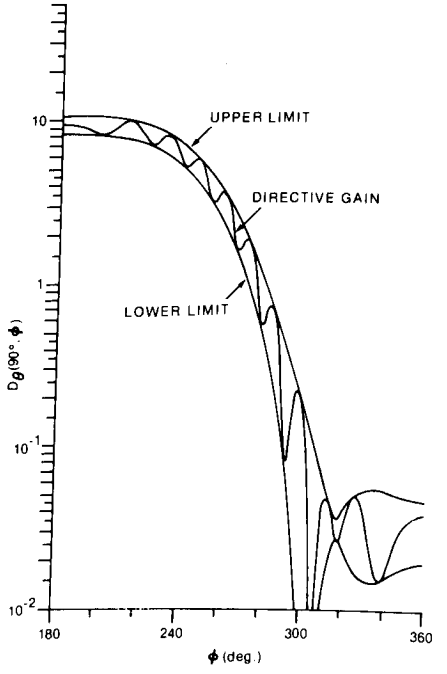

(d) $r_s/\lambda(r_s)$=4.536(2000m)

Fig. 60, Directive gain and far-field limit function patterns, along the ground plane, for CHFA's array in the presence of Fig. 57's $h/\lambda(h)$=.230(101.4m) tower where the tower is in the array's main beam and r_s ranges from 300m to 2000m.

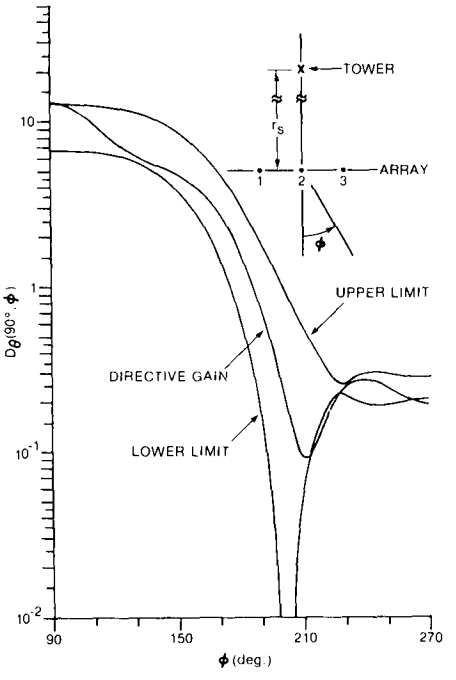

(a) $r_s/\lambda(r_s)=.6804(300m)$

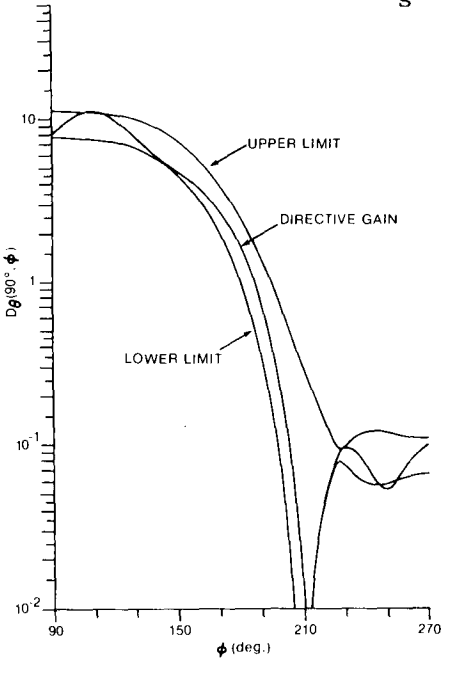

(b) $r_s/\lambda(r_s)=1.134(300m)$

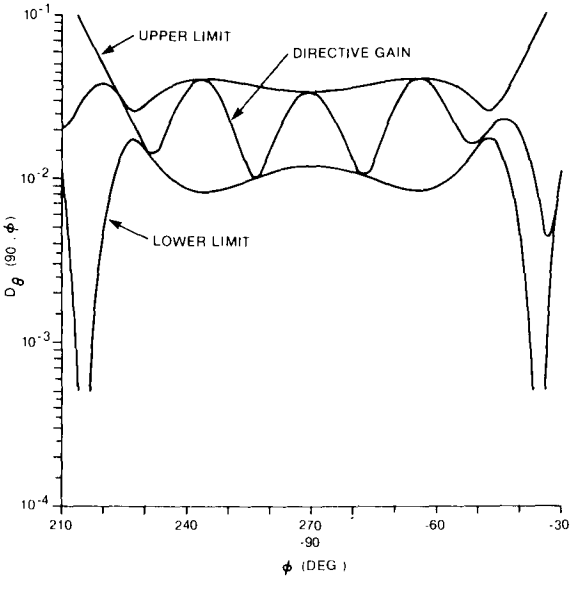

(c) $r_s/\lambda(r_s)=2.268(1000m)$

Fig. 61, Directive gain and far-field limit function patterns, along the ground plane, for CHFA's array in the presence of Fig. 57's $h/\lambda(h)=.230(101.4m)$ tower where the tower is located broadside to the array and r_s is (a) 300m, (b) 500m and (c) 1000m.

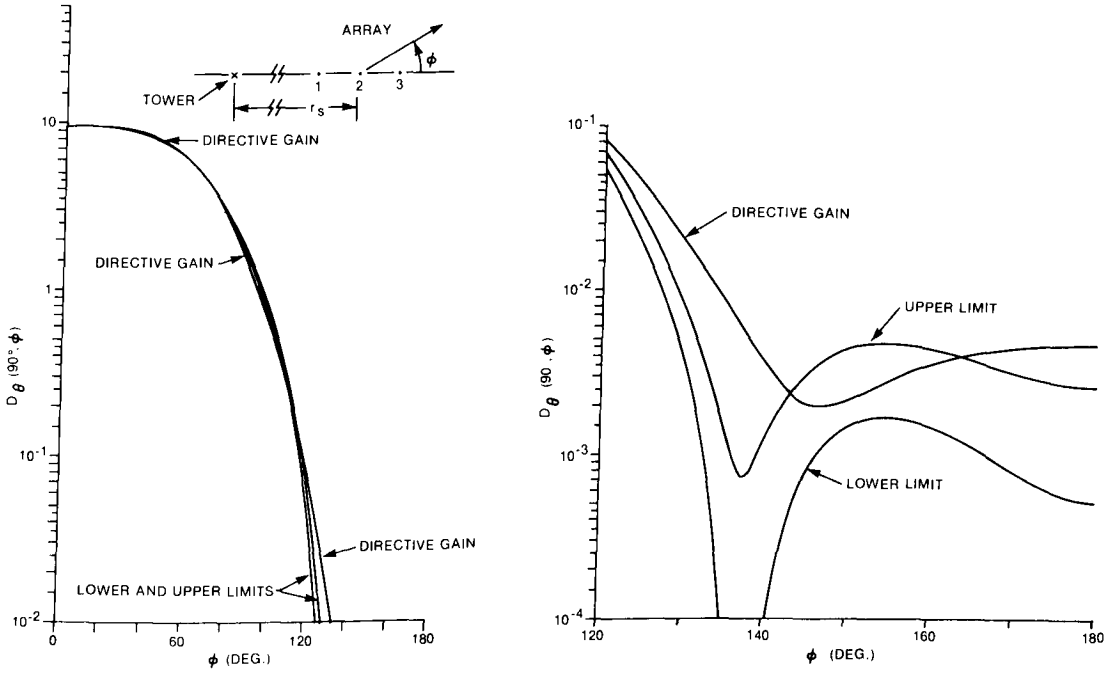

(a) $r_s/\lambda(r_s)=.6804(300m)$

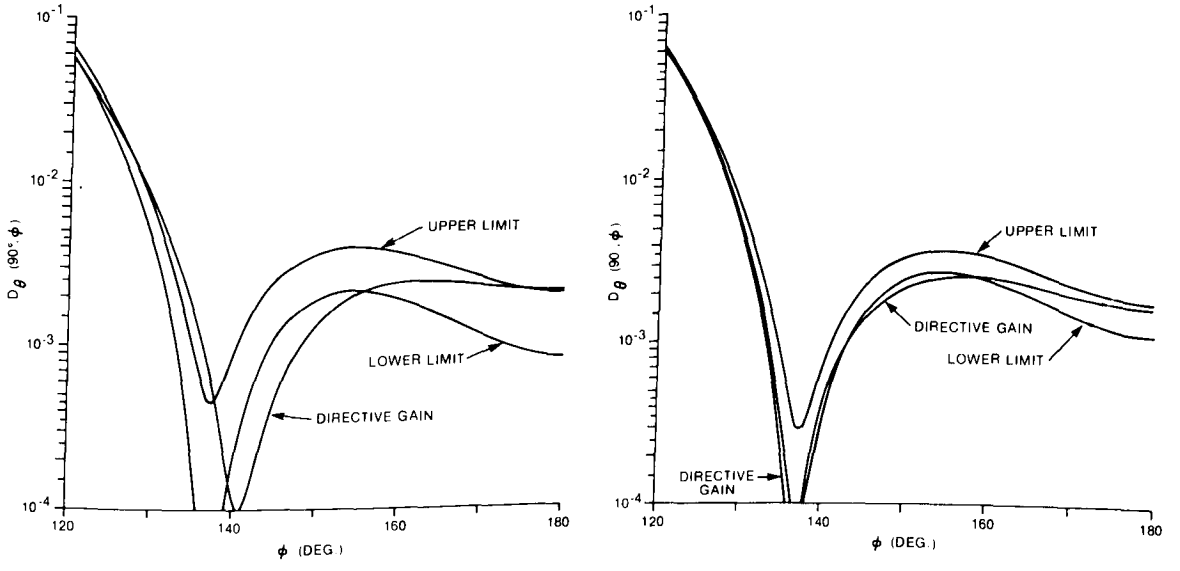

(b) $r_s/\lambda(r_s)=1.134(500m)$

(c) $r_s/\lambda(r_s)=2.268(1000m)$

Fig. 62, Directive gain and far-field limit function patterns, along the ground plane, for CHFA's array in the presence of Fig. 57's $h/\lambda(h)=.230(101.4m)$ tower where the tower is located in the array's null direction and r_s ranges between 300m and 1000m.

5.3 The Minimum r_s for which the Near-Field Limit Functions are Accurate when the Antenna is an Array

Figures 63 and 64 compare directive gain and near-field limit function patterns for CHFA's array in the presence of Fig. 57's $h/\lambda(h)=.230(101.4m)$ tower where the scattering tower is located in the direction of respectively the main beam and null for the array's pattern. The sub-figure corresponds to different values for r_s.

Let us first consider the case where the scattering tower is located in the direction of the main beam for the array's pattern. When $r_s/\lambda(r_s)$ is .6804(300m), Fig. 63(a) shows that the near-field limit functions are a little too widely separated. This is not surprising because, as was stated in their derivation, the near-field limit functions should only be used when the scatterer is in the far-fields of the elements of the array and when r_s is 300m the range between the scatterer and the nearest array element is 300m-110.2m or 189.8m; a range which is much less than the previously given value of 653.6m for r_n. The near-field limit function patterns in Fig. 63(b), where $r_s/\lambda(r_s)$ is 1.134(500m), are very close to true limits dispite the fact that the distance between the scatterer and nearest array element (500m-110.2=389.8m) is still significantly less than the above value for r_n. When the scatterer is in the direction of the main beam of the array's pattern, a comparison of Figs. 60(a) and 60(b) with respectively 63(a) and 63(b)shows that the far-field limit functions perform a little better than do the near-field limit functions. This probably occurs as the result of an approximation made during the derivation of the near-field functions wherein $D_{\theta k}(90°)$ was used to compute the strength of the field from array element k and incident on the scatterer. $D_{\theta k}(90°)$ is array element k's θ polarized directive gain along the ground plane when the scatterer and other array elements are absent. Its use in the near-field limit functions is approbriate only if the other excited arrray elements do not significantly change array element k's current distribution. In contrast, the far-field limit functions employ $D_{a\theta}(90°,180°)$ to compute the strength of the field incident on the scatterer. $D_{a\theta}(90°,180°)$ is the arrays directive gain in the direction of the scatterer when the scatterer is absent and hence any effects on an array element current distributions, due to interactions between array element currents, are included when $D_{a\theta}(90°,180°)$ is computed.

Figure 64 contains directive gain and near-field limit function patterns for the same array-scatterer combination considered above except that the scatterer is located in the null for the array's pattern. When r_s is 300m, the distance between the scatterer and the nearest array element (189.8m) is significantly less than r_n(653.6m) and, as Fig. 64(a) shows, the directive gain pattern falls outside the near-field limit patterns near the pattern's null direction. However when r_s is 500m and 1000m (see (b) and (c) in Fig. 64) the near-field limit functions give satisfactory upper and lower bounds for the directive gain pattern. When Figs. 62 and 64 are compared it is seen that for the case where the scatterer is in the direction of the null for the array's pattern, the near-field limit functions are accurate down to smaller values of r_s than are the far-field limit functions.

It is indicated that the near-field limit functions will be accurate if the range between the scatterer and the nearest array element is equal to or greater than r_n.

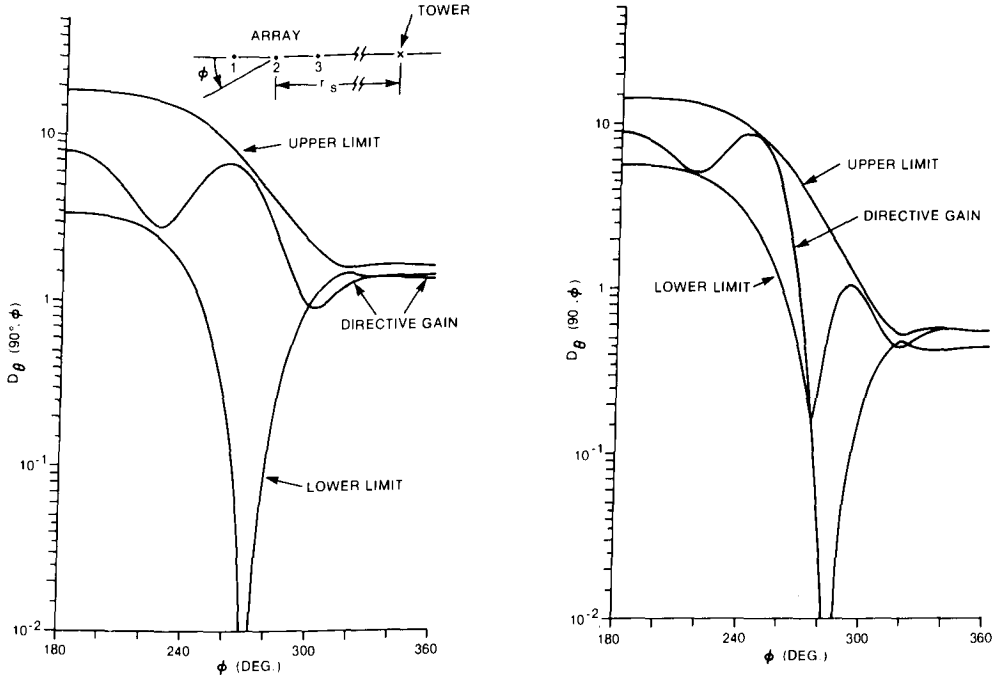

(a) $r_s/\lambda(r_s)=.6804(300m)$ (b) $r_s/\lambda(r_s)=1.134(500m)$

Fig. 63, Directive gain and near-field limit function patterns, along the ground plane, for CHFA's array in the presence of Fig. 57's $h/\lambda(h)=.230(101.4m)$ tower where the tower is located in the direction of the array's main beam and r_s is (a) 300m and (b) 500m.

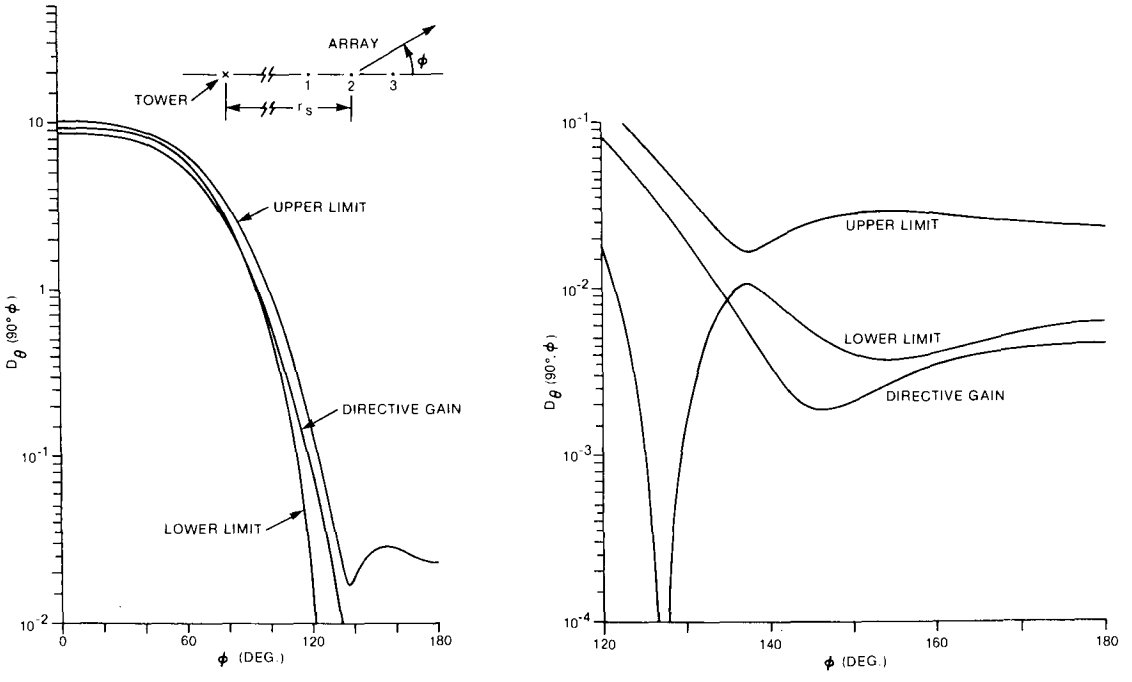

(a) $r_s/\lambda(r_s)$=.6804(300m)

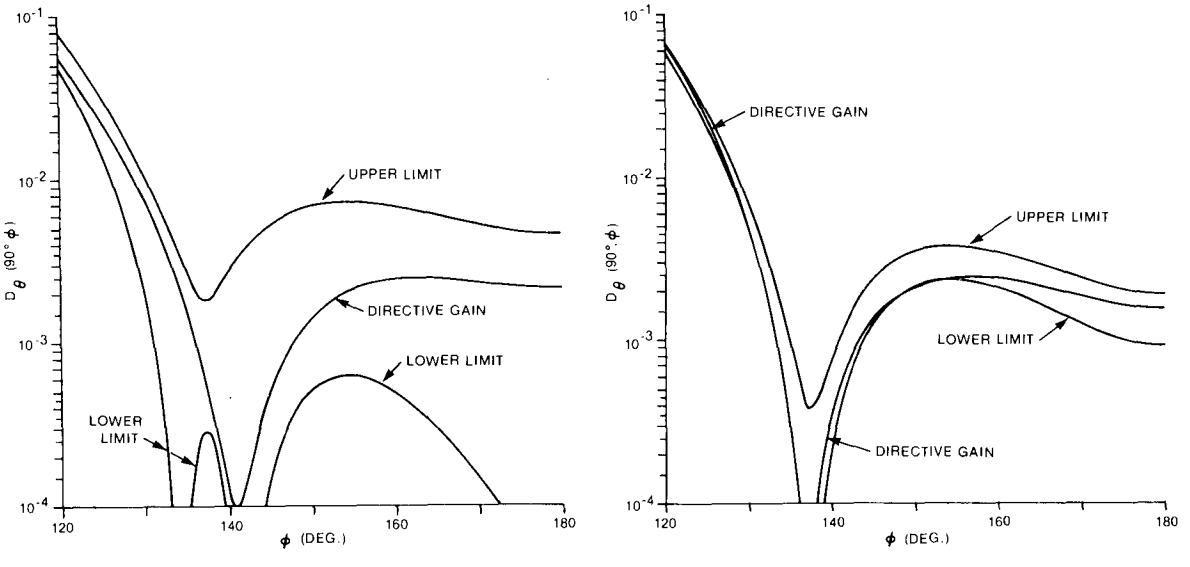

(b) $r_s/\lambda(r_s)$=1.134(500m)

(c) $r_s/\lambda(r_s)$=2.268(1000m)

Fig. 64, Directive gain and near-field limit function patterns, along the ground plane, for CHFA's array in the presence of Fig. 57's $h/\lambda(h)$=.230(101.4m) tower where the tower is located in the direction of the array's null and r_s is 300m, 500m and 1000m.

6. SUMMARY AND CONCLUSIONS

Two sets of limit functions (called far-field limit functions and near-field limit functions) were derived where both give approximate upper and lower bounds on the directive gain for an AM broadcast antenna in the presence of a tower, building or similar structure. When the antenna is a single monopole, the far-field and near-field limit functions are identical and give accurate bounds when the monopole to scatterer range (r_s) is about r_n (see eqn. (18)) or greater. For the case where the antenna is a multi-element array, the two types of limit functions differ as regards the minimum r_s for which they are accurate. The far-field limit functions are simpler than the near-field functions and are accurate provided r_s is large enough such that the array's directive gain can be employed to accurately compute the power density of the field incident on the scatterer. Accurate bounds are provided by the near-field limit functions provided the distance from the scatterer to the nearest array element is approximately r_n or larger. The near-field limit function's minimum range can be significantly less than that for the far-field functions when the direction to the scatterer is near that for a null in the array's pattern.

The scatterer's scattering cross-section must be known before the above limit functions can be used. This parameter is both difficult to accurately compute and not readily available and therefore included here (see Section 3) are scattering cross-section characteristics for structures ranging from towers whose radii are .0005λ, up to buildings whose dimensions in horizontal cross-section are .2λx.2λ.

The limit functions show that a structure would distort an antenna's directive gain pattern less if the structure's scattering cross-section were reduced. The following two methods for reducing a tower's scattering cross-section were investigated.
1) Electrical isolation of the base of the tower from the ground plane.
2) Placement of vertical stubs on the tower.

Method 1) was found to be effective provided the tower's height (h) is about λ/4 or less. Method 2) was tested on towers whose heights (h) were λ/2 or less. The characteristics for full-length loaded stubs on a tower (see Fig. 35) were computed. It was found that: 1) the frequency bandwidth for this system increased significantly as the number of stubs was increased from one to four, and 2) changing the stub wire to adjacent tower wire spacing (d) from .0015λ to .0030λ, increased the system's bandwidth: however this increase was not considered to be significant. Note that by the statement under 2) above, the author does not wish to imply that the d/λ spacing is not important. Further research is required to determine the effect of d/λ's magnitude on the system's properties. Both full-length loaded and short stubs (see Fig. 44) were tried on towers where h ranged between .25λ and .50λ. The short stubs were found to perform best. This was particularly true when h was greater than about .35. The calculations showed that care should be taken when adjusting the: 1) load reactance for full-length loaded stubs, and 2) length for short stubs. This is true because improper adjustments of the above could easily produce a scattering

cross-section for the tower-stub system which is much larger than that for the tower alone.

We have not investigated here the use of stubs on buildings as means of reducing their scattering cross-section because it was felt that an impractically large number of stubs would be required. Note that it has been shown here that at least four stubs are required to give the tower-stub system sufficient bandwidth. S.J. Kavangh[10] has investigated the use of rooftop umbrella type structures as a means for reducing a building's scattering cross-section. In full scale tests he managed to reduce the scattered field by 4.4 db to 6.6 db. It therefore appears that we do not have a practical method for significantly reducing a building's pattern distorting effect. The limit functions and scattering cross-section values in this document should enable the broadcaster to predict whether or not a building (or tower) will cause a problem and hence, if necessary, make it possible for him to take action before the structure has been erected.

7. REFERENCES

1. **Harrington, R.F.,** "Field Computation by Moment Methods", MacMillan Co., N.Y., 1968.

2. **Burke, G.J.,** "The Numerical Electromagnetic Code (NEC)", in "Applications of Moment Methods to Electromagnetic Fields", Edited by Bradley J. Straite, The SCEEE (Southeastern Center for Electrical Engineering Education) Press, 11th and Massachusetts Ave., St. Cloud, Florida, U.S.A., 32769, 1980.

3. **Trueman, C.W. and S.J. Kubina,** "Analysis of Reradiation from the South-Eastern Route Power Line into the Restricted Arc of the Pattern of Station CHFA Edmonton", Report No. CHFA-1, Sept. 25, 1980. Report prepared for the Canadian Broadcastsing Corp., Engineering Headquarters, 7925 Côte St. Luc Road, Montreal Que., H4W 1R5.

4. **Royer, G.M.,** "The Effects of Re-radiation from Highrise Buildings and Towers Upon the Antenna Patterns for AM Broadcast Arrays", 1981 IEEE International Symposium on Electromagnetic Compatibility, Boulder, Colorado, pp. 372-378.

5. **Belrose, J.S., W. Lavrench, J.G. Dunn, C.W. Trueman and S.J. Kubina,** "The Effects of Re-radiation from Highrise Buildings and Transmission Lines Upon the Radiation Pattern of MF Broadcasting Antenna Arrays", Proceedings of AGARD/EPP Meeting, Spatind, Norway, Sept. 1979, pp. 2-1 to 2-11.

6. **Belrose, J.S., C.W. Trueman, S.J. Kubina, W. Lavrench and J.G. Dunn,** "On Minimizing the Effects of Re-radiation from Power Transmission Lines on the Radiaton Patterns of MF-AM Broadcasting Antenna Arrays", IEE Second International Conference on Antennas and Propagation, York, England, April 1981.

7. **Trueman, C.W., and S.J. Kubina,** "Numerical Computation of the Reradiation from Power Lines at MF Frequencies", IEEE Transactions on Broadcasting, Vol. BC-27, No. 2, June 1981, pp. 39-45.

8. **Trueman, C.W., S.J. Kubina and J.S. Belrose,** "Corrective Measures for Minimizing the Interaction of Power Lines with MF Broadcast Antennas", IEEE Transactions on Electromagnetic Compatibility", Vol. EMC-25, No. 3, Part II, Aug. 1983, pp. 329-339.

9. **Silva M.M., K.G. Balmain and E.J. Ford,** "Effects of Power Line Re-radiation on the Patterns of a Dual-frequency MF Antenna", IEEE Transactions on Broadcasting, Vol. BC-28, No. 3, Sept. 1982, pp. 94-103.

10. **Kavanagh, S.J.,** "AM Broadcast Reradiation From Buildings", MASc Thesis, Dept. of Elect. Eng., University of Toronto, Sept. 1982.

11. **Tilston, M.A.,** "AM Broadcast Re-radiation from Steel Tower Power Lines", MASc Thesis, Dept. of Elect. Eng., University of Toronto, Jan. 1983.

APPENDIX A

THE GROUND PLANE FIELD PATTERN FOR CHFA'S BROADCAST ARRAY AS A FUNCTION OF RANGE

A-1. INTRODUCTION

When the field due to a radiating structure is being measured for the purpose of determining its directive gain, it is necessary that the measurements be made at a sufficiently large range from the structure. This is true because the shape of an antenna's field pattern changes as a function of range (r), and is only equal to the far-field shape in the limit as r approaches infinity. Investigated here is how the shape of the pattern for CHFA (Edmonton)'s broadcast array changes as r is changed.

In addition, it will be shown that a commonly used method for computing the far-field pattern shapes for broadcast arrays can give erroneous peak-to-null region ratios.

Unless otherwise indicated, all calculations will be done using a computer program called NEC (Numerical Electromagnetic Code).

A-2. COMPUTATION OF THE GROUND PLANE FIELD PATTERN FOR CHFA'S ARRAY AS A FUNCTION OF RANGE

Many of the symbols used here are defined in Fig. A-1. The values listed in Fig. A-1 caption were taken from [3]. Note that CHFA's towers are triangular in cross-section where each side of the triangle is 2 ft. (.6096m) long. The calculations which appear here were done for towers which are circular in cross-section where the towers' radii are .8 ft (.24384m). This will make no appreciable difference as far as the array's patterns are concerned. It will, however, result in computed input impedance characteristics which are somewhat different from those for CHFA's array elements.

Let

$I_k = |I_k| \exp(j\alpha_k)$, $k = 1,2,3$ be the current at the inputs to array elements 1, 2 and 3.

$V_k = |V_k| \exp(j\beta_k)$, $k = 1,2,3$ be the voltage at the input to array elements 1, 2, and 3.

Note that the magnitudes for current voltage and electric field intensity will be peak (as distinguished from rms) values. The caption for Fig. A-1 shows that the input currents are related to each other as follows:

$I_1/I_2 = .538\angle 97.5°$

$I_3/I_2 = .484\angle -97.5°$.

NEC employs voltage sources and therefore our first step will be the computation of the voltage sources which produce the following source currents:

$I_1 = .538\angle 97.5°$ amps (A-1)

$I_2 = 1\angle 0°$ amps (A-2)

$I_3 = .484\angle -97.5°$ amps (A-3)

When the array elements are fed by source voltages, it is most convenient to relate the feed currents and voltages as follows:

$$\begin{bmatrix} I_1 \\ I_2 \\ I_3 \end{bmatrix} = \begin{bmatrix} Y_{11}, Y_{12}, Y_{13} \\ Y_{21}, Y_{22}, Y_{23} \\ Y_{31}, Y_{32}, Y_{33} \end{bmatrix} \begin{bmatrix} V_1 \\ V_2 \\ V_3 \end{bmatrix} \quad \text{(A-4)}$$

NEC can be used to compute the elements in the above admittance array. For example, to compute Y_{11}, Y_{21} and Y_{31}, a voltage source (V_1) is applied at the input of array element 1 while the inputs to array elements 2 and 3 are shorted (i.e. $V_2 = V_3 = 0$). Under these conditions, NEC is used to compute I_1, I_2 and I_3 and, as equation (A-4) shows, Y_{11}, Y_{21} and Y_{31} are given by the following equations.

$Y_{11} = I_1/V_1$

$Y_{21} = I_2/V_1$

$Y_{31} = I_3/V_1$

NEC gives the following values (in mhos) for equation (A-4)'s admittance array:

$Y_{11} = 3.11282\text{X}10^{-3} + j(1.24366\text{X}10^{-3})$

$Y_{21} = 9.98481\text{X}10^{-4} + j(-1.86297\text{X}10^{-3})$

$Y_{31} = -1.57794\text{X}10^{-3} + j(-6.83925\text{X}10^{-4})$

$Y_{12} = 9.98472\text{X}10^{-4} + j(-1.86298\text{X}10^{-3})$

$Y_{22} = 2.51533\text{X}10^{-3} + j(1.26720\text{X}10^{-2})$

$Y_{32} = 9.98472\text{X}10^{-4} + j(-1.86298\text{X}10^{-4})$

$Y_{13} = -1.57794X10^{-3} + j(-6.83925X10^{-4})$

$Y_{23} = 9.98481X10^{-4} + j(-1.86297X10^{-3})$

$Y_{33} = 3.11282X10^{-3} + j(1.24366X10^{-2})$

It follows from the reciprocity theorem (where $Y_{mn} = Y_{nm}$ or $Y_{12} = Y_{21}$, $Y_{13} = Y_{31}$ and $Y_{23} = Y_{32}$) and the symmetry associated with CHFA's array (which necessitates that $Y_{11} = Y_{33}$, $Y_{12} = Y_{32}$, $Y_{13} = Y_{31}$ and $Y_{21} = Y_{23}$), that

$Y_{12} = Y_{21} = Y_{32} = Y_{23}$

$Y_{11} = Y_{33}$

$Y_{13} = Y_{31}$

In general when two values should be equal as a result of symmetry, then NEC computes them as being equal. It is interesting to note as well that NEC output satisfies the reciprocity theorem very accurately. For example, compare the values for Y_{12} and Y_{21} (which are equal only through reciprocity), in the above list.

Inversion of the admittance array in equation (A-4) gives the impedance array in

$$\begin{bmatrix} V_1 \\ V_2 \\ V_3 \end{bmatrix} = \begin{bmatrix} Z_{11}, & Z_{12}, & Z_{13} \\ Z_{21}, & Z_{22}, & Z_{23} \\ Z_{31}, & Z_{32}, & Z_{33} \end{bmatrix} \begin{bmatrix} I_1 \\ I_2 \\ I_3 \end{bmatrix} \qquad \text{(A-5)}$$

When the admittances have the values listed above, then the elements of the impedance array (in ohms) are:

$Z_{11} = 20.0315 + j(-75.8038)$

$Z_{21} = 10.7392 + j(-8.96876)$

$Z_{31} = -4.12887 + j(-8.22499)$

$Z_{12} = 10.7391 + j(-8.96876)$

$Z_{22} = 19.6484 + j(-75.9588)$

$Z_{32} = 10.7391 + j(-8.96885)$

$Z_{13} = -4.12887 + j(-8.22499)$

$Z_{23} = 10.7392 + j(-8.96876)$

$Z_{33} = 20.0315 + j(-75.8038)$

Substitution of the currents given by (A-1) to (A-3) into equation (A-5) gives the voltage sources which will produce these currents. The results (in volts) are

$V_1 = 46.0799 + j(9.53997)$

$V_2 = 18.6960 + j(-74.1874)$

$V_3 = -22.2244 + j(-15.4170)$

When the above are used as NEC's voltage sources, it computes the following.

P_t (power transmitted) = 14.6754 watts

$I_1 = .537998 \angle 97.500076°$ amps

$I_2 = .999997 \angle .000049°$ amps

$I_3 = .484000 \angle -97.500043°$ amps

It can be seen that the above currents are very close to those specified by (A-1) to (A-3).

Finally, the voltage sources as specified above give a radiated power of 14.6754 watts. We want the transmitted power to be 10^4 watts. To obtain this power, we must use voltage sources which are C times as large as those shown above where

$C = [10^4/14.6754]^{\frac{1}{2}}$

The resulting voltage sources (in volts) are

$V_1 = 1202.86 + j(249.030)$

$V_2 = 488.038 + j(-1936.58)$

$V_3 = -580.143 + j(-402.444)$

We now have sufficient information to compute the array's electric field intensity patterns using NEC. Only patterns along the ground plane ($\theta = 90°$) will be considered here. The ground plane was made to be a perfect conductor. Therefore, at the ground plane, the electric field intensity vector is on necessity θ (or Z) polarized. Let

$E_\theta(r,90°,\phi)$ = the electric field intensity due to the array where the subscript θ refers to the polarization direction and $(r,\theta,\phi) = (r,90°,\phi)$ specifies the location of the field.

In the limit as r approaches infinity, $|E_\theta(r,90°,\phi)|$ varies as 1/r. Therefore, for the purpose of making the patterns for different values of r easy to compare, we will plot $r|E_\theta(r,90°,\phi)|$ as a function

of ϕ. The results of the computations using NEC are shown in Figs. A-2 and A-3.

A-3. A COMPARISON OF THE GROUND PLANE FAR-FIELD PATTERNS FOR CHFA'S ARRAY AS COMPUTED USING A SIMPLE EQUATION AND NEC

A commonly used method for computing the far-field patterns for broadcast arrays makes use of the assumptions that:

(a) The amplitude, at a given range, of the far electric field on the ground, due to an element of the array is proportional to the amplitude of the current at the element's input.

(b) The relative phases of the contributions by the elements of the array to the far electric field on the ground plane, is correctly given by considering the phases of the currents at the inputs to the array elements and the differences in distance from the array elements to the far-field point.

Application of the above method to CHFA's array gives:

$$\lim_{r\to\infty} r\left|E_\theta(r,90°,\phi)\right| = A\left|I_1\right|e^{j[\alpha_1-2\pi(s/\lambda)\cos\phi]} + \left|I_2\right|e^{j\alpha_2} + \left|I_3\right| e^{j[\alpha_3+2\pi(s/\lambda)\cos\phi]} \qquad \text{(A-6)}$$

where A is a constant. The constant A is present because the method gives only the shape of the array's pattern.

In Fig. A-4, ground plane far-field patterns, as computed using NEC and eqn. (A-6), are compared. The constant A in equation (A-6) has been set so that equation (A-6) gives the same value for $r\left|E_\theta(r,90°,\phi)\right|$ as does NEC when $\phi = 0°$. It can be seen that the two methods give significantly different peak-to-null region ratios.

Equation (A-6) gives true patterns if it is assumed that the current distributions for the array elements are the same. Note that two current distributions are said to be the same if a constant can be found such that the constant times one of the current distribution is equal to the other current distribution. Tables A-1 and A-2 show NEC's computation of how current phase and current amplitude vary along CHFA's array elements. It can be seen that the current distributions are only approximately equal. The conclusion is that significant errors can occur in the peak-to-null region ratios for array patterns when they are computed with equations like (A-6).

TABLE A-1

THE VARIATION OF CURRENT PHASE ALONG THE ELEMENTS OF CHFA'S ARRAY AS COMPUTED BY NEC

z (meters)	$\alpha_1(z) - \alpha_1$ (deg.)	$\alpha_2(z) - \alpha_2$ (deg.)	$\alpha_3(z) - \alpha_3$ (deg.)
.762	.0	.0	.0
2.762	-.070	-.203	-.405
6.000	-.161	-.460	-.910
11.200	-.281	-.792	-1.546
19.500	-.455	-1.238	-2.375
32.570	-.711	-1.832	-3.425
48.522	-1.021	-2.447	-4.441
64.470	-1.341	-2.987	-5.270
80.418	-1.671	-3.471	-5.963

TABLE A-2

THE DISTRIBUTION OF CURRENT AMPLITUDE ALONG THE ELEMENTS OF CHFA'S ARRAY AS COMPUTED BY NEC

z (metres)	$\|I_1(z)\|/\|I_1\|$	$\|I_2(z)\|/\|I_2\|$	$\|I_3(z)/\|I_3\|$
.762	1.0	1.0	1.0
2.762	.9828	.9852	.9914
6.000	.9591	.9645	.9782
11.200	.9232	.9322	.9551
19.500	.8611	.8745	.9082
32.570	.7457	.7631	.8069
48.522	.5750	.5933	.6389
64.470	.3746	.3894	.4260
80.418	.1419	.1485	.1647

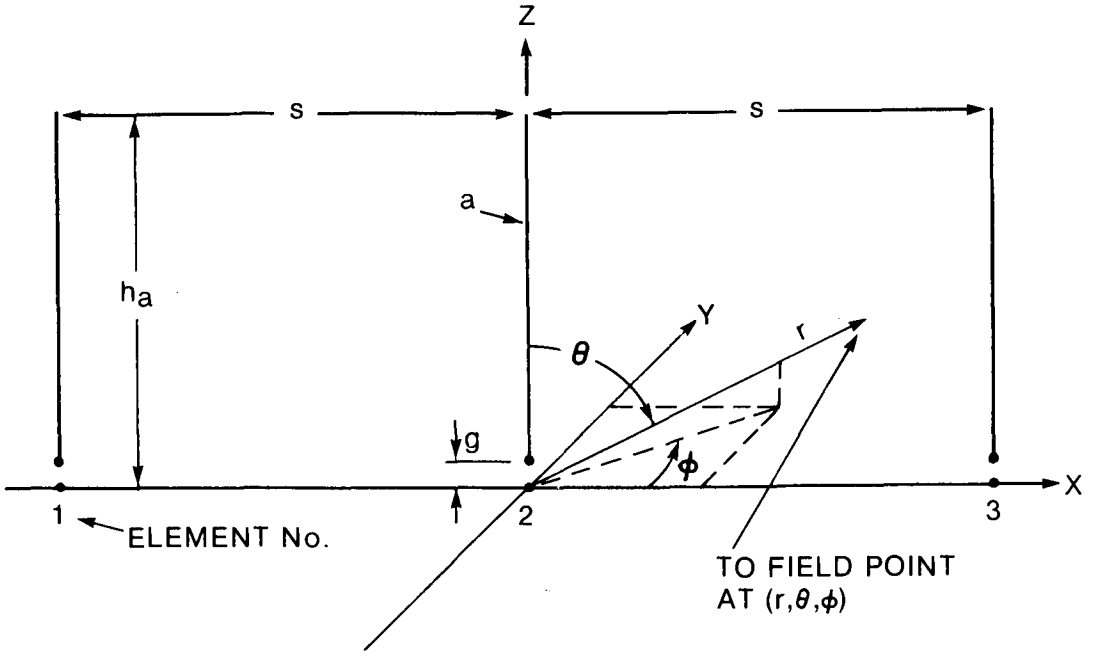

Fig. A-1, Geometry for CHFA's broadcast array where: f=680kHz(λ=440.882m), h_a=88.392m, s=λ/4=110.221m, g(feed gap)=1.524m, a(radius of element)=.24384m, P_t(power transmitted) = 10kW. I_1, I_2, and I_3 are the feed currents for respectively elements 1, 2 and 3 where: $I_1/I_2 = .538\angle 97.5°$, $I_3/I_2 = .484\angle -97.5°$. The XY plane (ground plane) and array elements are assumed to be perfectly conducting.

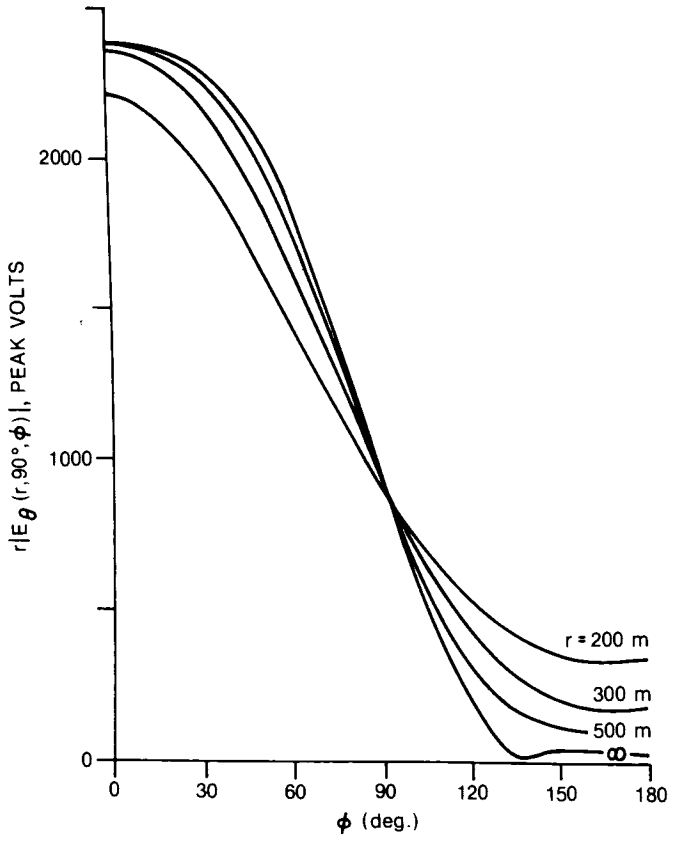

Fig. A-2, NEC computed field patterns for CHFA's array where r=200m, 300m and 400m.

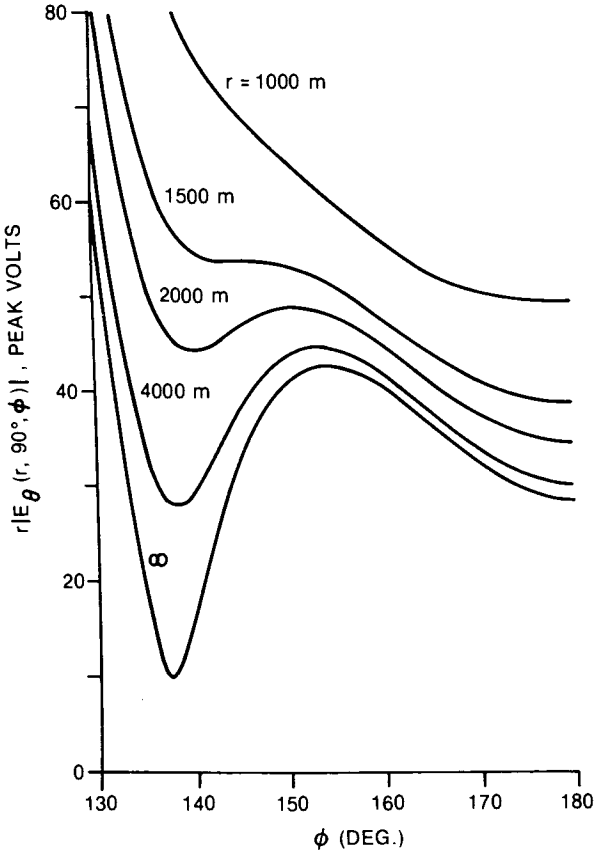

Fig. A-3, NEC computed field patterns, in the null region, for CHFA's array where r=1000m, 1500m, 2000m, 4000m and ∞.

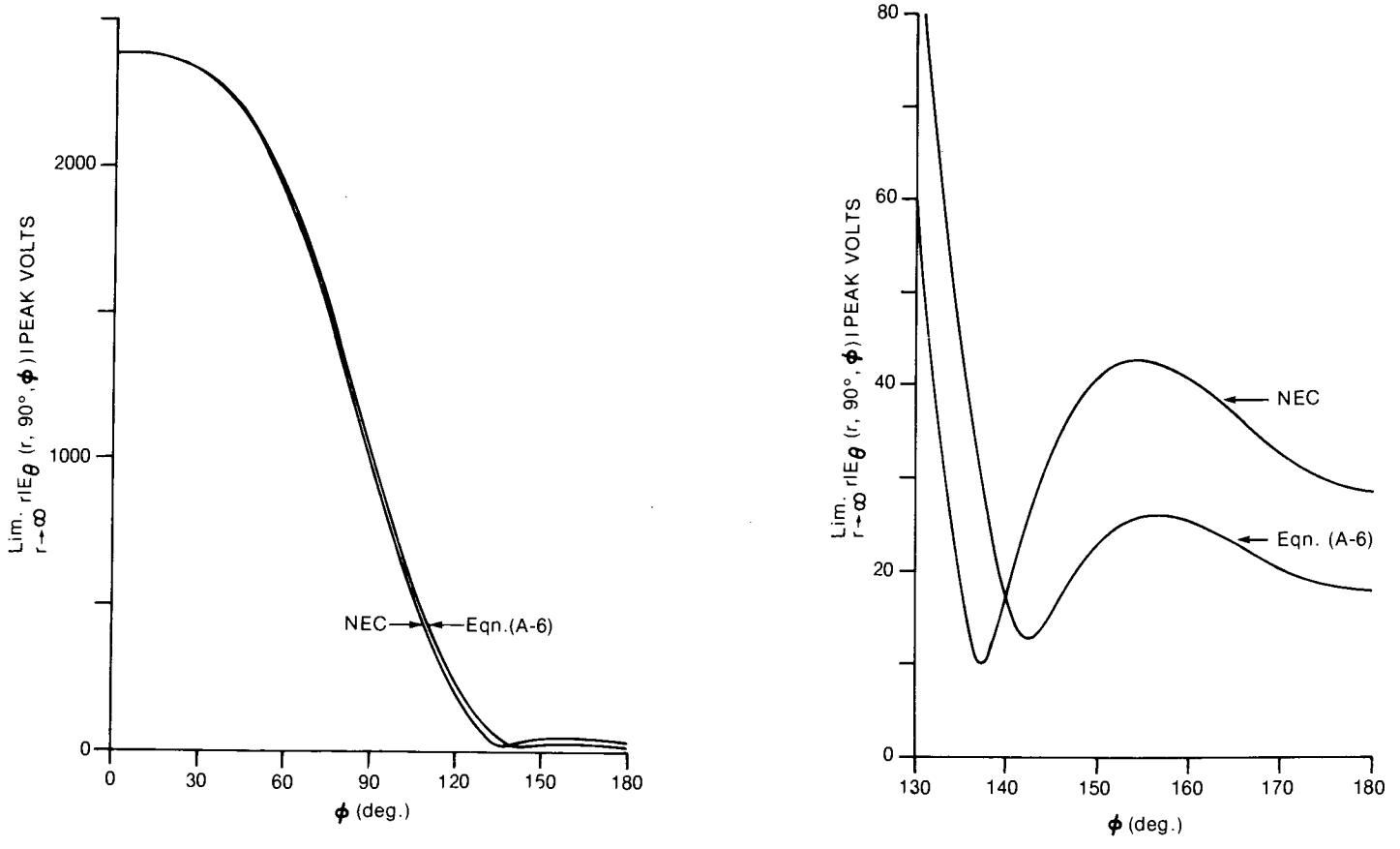

Fig. A-4, A comparison of far-field patterns for CHFA's array as computed using NEC and eqn. (A-6).

APPENDIX B

AN EXPERIMENTAL TEST OF THE COMPUTER PROGRAM NEC

The computer program NEC was extensively used to obtain the results previously presented in the report. This appendix contains an experimental test of the ability of NEC to compute these results.

Figure B-1 shows the test set-up used when making the measurements. A Hewlett Packard 8505A network analyzer was employed to measure the insertion loss presented by: a) the two monople antennas shown in Fig. B-1, b) the two monopole antennas bracketing a model tower, and c) the two monopole antennas bracket the above tower where the tower had stubs. Refer to Fig. B-2 for the dimensions of the tower and stubs. The elevated ground plane and its skirts form a continuously conducting surface. The large ground plane was formed of a 2.5 cm x 2.5 cm wire mesh screen which was about 15.2 m in radius.

For the NEC calculations the dimensions and relative locations of the antennas and scatterers were as shown in Figs B-1 and B-2. The ground plane was made to be flat and infinite. All surfaces were considered to be perfectly conducting. In the test set-up the cable characteristic impedance and the network analyzer's source and load impedance were 50 Ω and therefore the NEC model incorporated: a) a voltage source in series with a 50 Ω (R) resistor at the base of the transmitting antennas, and b) a 50 Ω (R) resistor at the base of the receiving antenna. The power absorbed in the receiving antenna's resistor is given by $P_r = |I_r/\sqrt{2}|^2 R$ where I_r is the peak current at the base of the receiving antenna. If the transmitting antenna's source (voltage source and series 50 Ω resister) were connected directly to the receiving antenna's base resistor, the power in the latter resister would be given by $P_o = |V_t/\sqrt{2}|^2/(4R)$ were V_t is the peak voltage for the voltage source. The insertion loss (I.L.) associated with the system is therefore given by

$$\text{I.L.} = \frac{P_r}{P_o} = \frac{|I_r|^2}{|V_t|^2} 4R^2 \qquad \ldots(\text{B-1})$$

For a given V_t, NEC was used to compute I_r. Equation (B-1) was then used to determine the insertion loss.

Refer to Fig. B-3 for both measured and calculated I.L. values over the frequencies from 250 MHz to 300 MHz. Several points of interest are: a) The greatest difference between the measured and computed I.L. values was 1.3 dB, b) At least for f between 250 MHz and 300 MHz, the tower reduces the coupling between the antennas, and c) the I.L. curve for the case where the scatterer is the tower with stubs, crosses over that for the case where there is no scatterer, at about f = 274 MHz. At the above cross-over

frequency the tower with stubs effectively disappears. It would be expected that the forward scattering cross-section (σ_θ (90°,180°)) for the tower with stubs would have a minimum at about f = 274 MHz. As Fig. B-4 shows, NEC indicates this to be true.

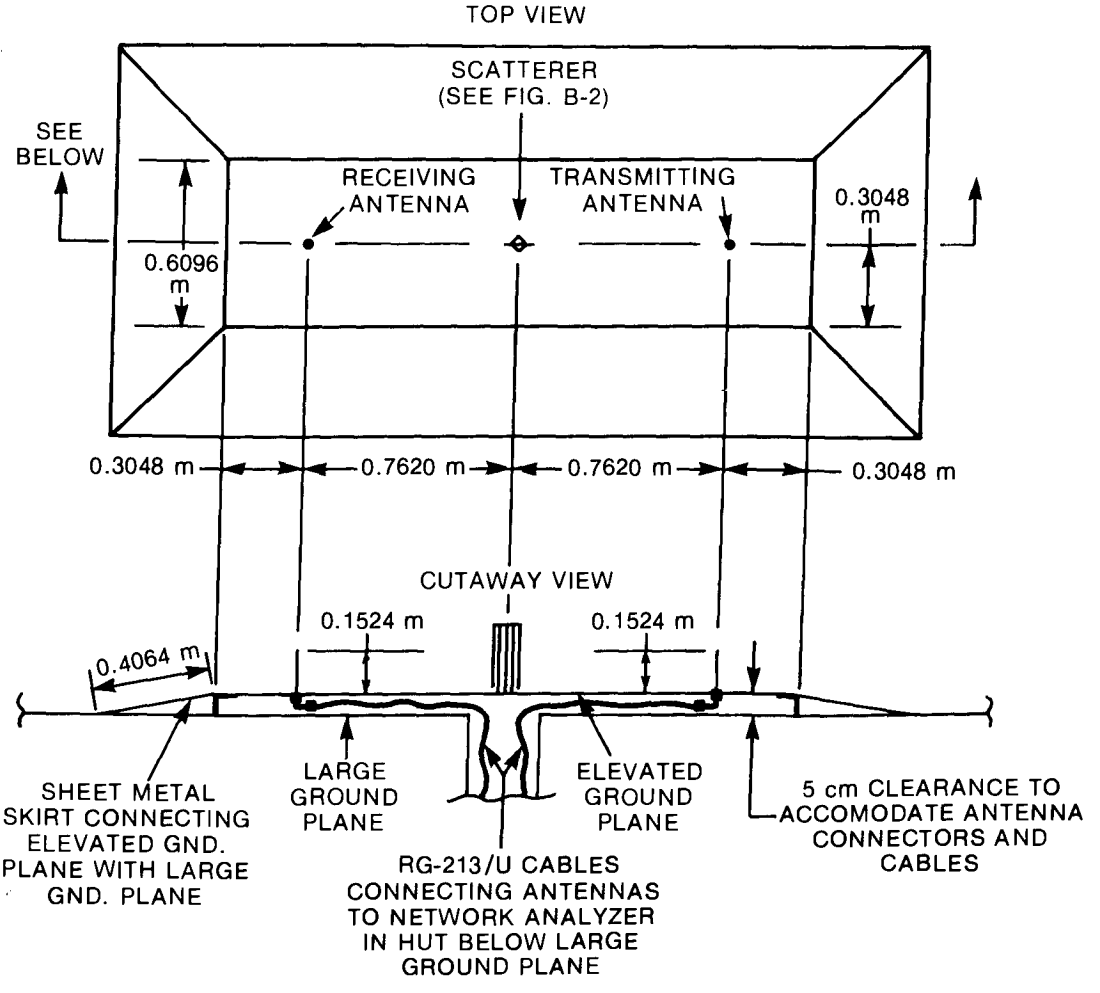

Fig. B-1, Test set-up for insertion loss measurements. See Fig. B-2 for scatterer dimensions. The Monopole antennas were .3175 cm in diameter.

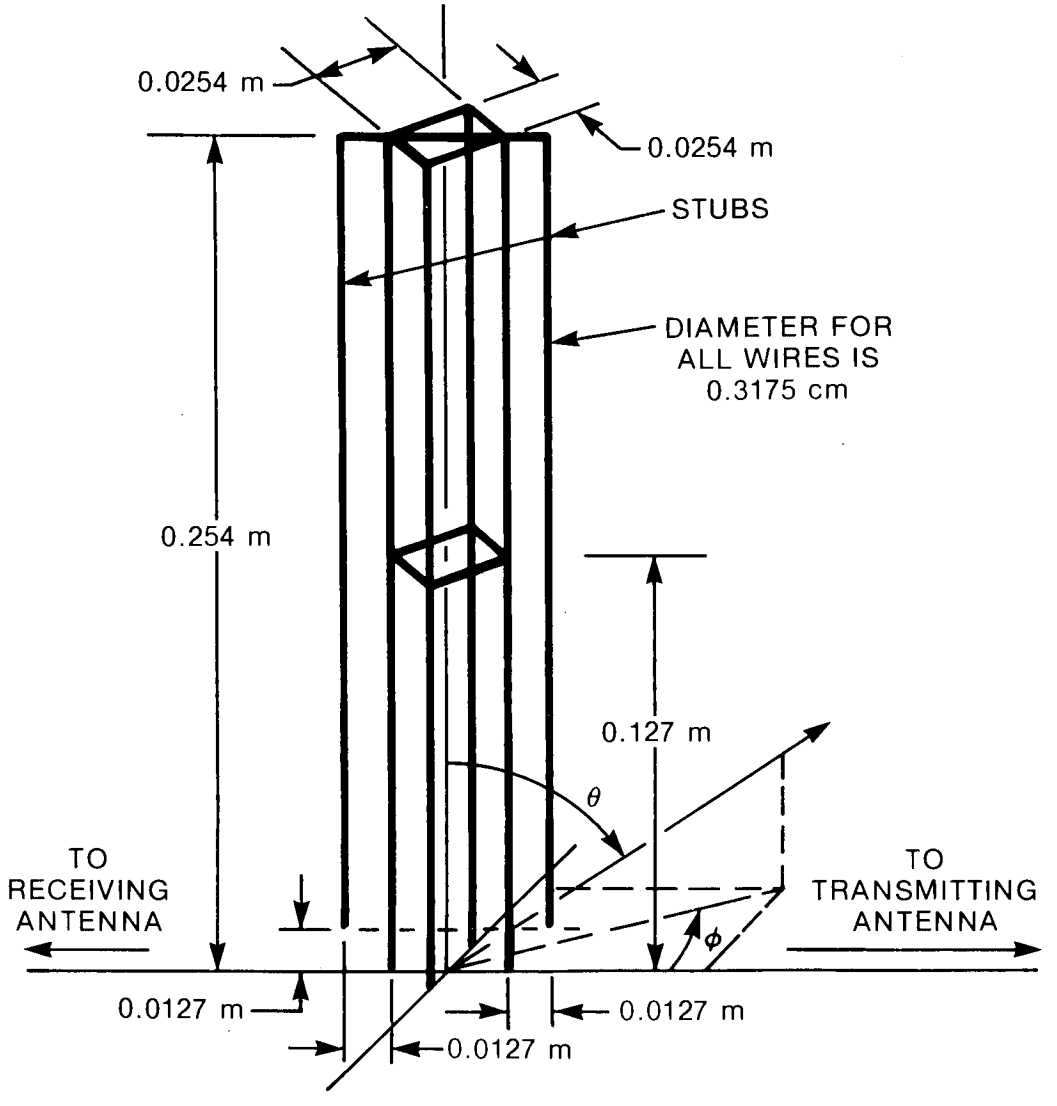

Fig. B-2, Two scatterers were used: a) the above model tower with stubs, and b) the above metal tower without the stubs.

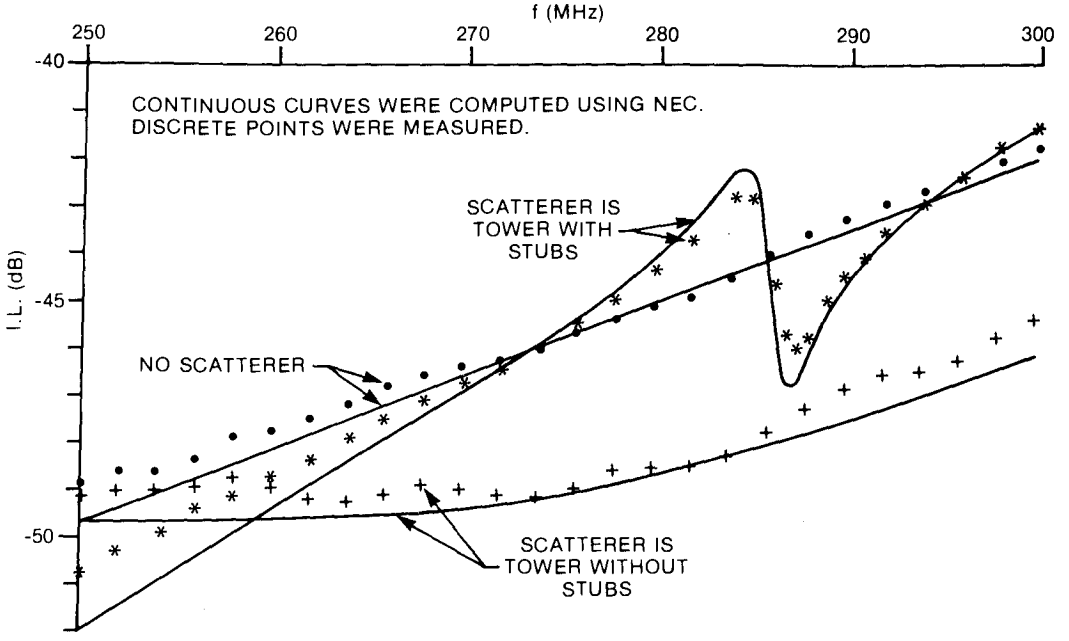

Fig. B-3, NEC computed and measured insertion loss (I.L.), as a function of frequency (f) and two monopole antennas bracketing: a) no scatterer, b) a tower with stubs, and c) a tower without stubs. Refer to Figs. B-1 and B-2 for the dimensions and relative locations of the antennas and scatterers.

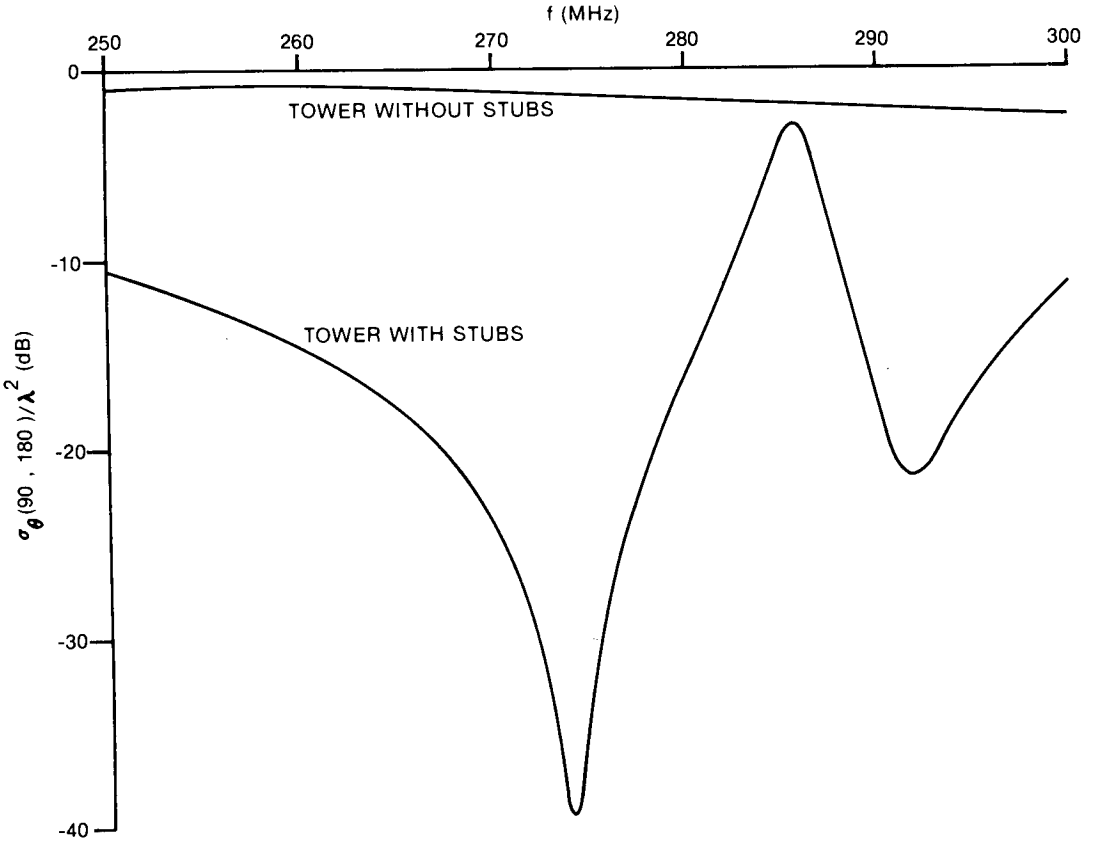

Fig. B-4, NEC computed $\sigma_\theta(90°,180°)/\lambda^2$ as a function of frequency for Fig. B-2's tower with stubs and tower without stubs.